Fakultät für Chemie

Lehrstuhl für Physikalische Chemie

Static and dynamic characterization of size-selected cluster diffusion and ripening on periodically wettable surfaces

Yves Fukamori

Vollständiger Abdruck der von der Fakultät für Chemie der Technischen Universität München zur Erlangung des akademischen Grades eines

Doktors der Naturwissenschaften

genehmigten Dissertation.

Vorsitzender: Univ.-Prof. Dr. Ulrich K. Heiz

Prüfer der Dissertation:

1. Priv.-Doz. Dr. Friedrich Esch
2. Univ.-Prof. Dr. Klaus Köhler

Die Dissertation wurde am 26.11.2015 bei der Technischen Universität München eingereicht und durch die Fakultät für Chemie am 26.01.2016 angenommen.

Πάντα χωρεϊ καί ουδέν μένει

(Plato, *Kratylos*)

Acknowledgements

I want to thank Ueli Heiz and Friedrich Esch for the chance they gave me to perform my PhD at the Chair for Physical Chemistry and especially in the STM Laboratory.

Many thanks go to my colleagues in the STM Laboratory Bo, Michael and Fabian, whose support and knowledge were always a great help for me. Thanks for proofreading go to Fabian.

Special thanks go to Giulia Troiano, who was a great help with LabVIEW programming and without whom the Atom Tracking project would probably not have been realized.

Thanks go to the electronic and the mechanic workshops of the Chemistry Department and especially to Max Wiedemann for his expertise and advice.

Thanks to all my colleagues, to the staff of the group and the students that passed by in our lab in the last years. Thanks to my office colleagues, who distracted me from work and with whom it was a pleasure to go for a conference or a beer. In this context I have to mention especially Martin Tschurl, who was always there to give good advice when times were hard. Thank you Martin!

Thanks go also to the National Research Found Luxembourg for financial support.

In the end I thank my family and my friends for their support and their sympathy during the last years.

Table of contents

Summary

Sintering is one of the major routes for deactivation of surface-supported catalytic particles in heterogeneous catalysis. Therefore, the first part of this thesis deals with the characterization of cluster ripening. The two mechanisms responsible for such coarsening phenomena are Ostwald ripening, where larger clusters tend to grow at the expense of smaller ones, and Smoluchowski ripening, where entire clusters diffuse and coalesce. The sintering properties of cluster-assembled materials can be tuned by the interaction between the particle and the substrate. In order to explore fundamental factors that control cluster ripening mechanisms, truly monodisperse Pd clusters are deposited on three different model catalysts: bare Rh(111), graphene-Moiré films grown on Rh(111) and Ru(0001), as well as a hexagonal boron nitride film grown on Rh(111). The evolution of particle size and density was tracked by high resolution scanning tunneling microscopy. The principal microscopic mechanisms governing the ripening processes on each of the three substrates have been determined from thorough data analysis of the cluster heights and size distributions. The ripening mechanisms were related to the distinct cluster adsorption and atom detachment energies obtained from first-principle calculations. These results elucidate the ripening processes and underlie formulation of a strategy for optimizing cluster stability against ripening, where both the binding of the clusters to the surface, as well as that of the individual atoms must be controlled. Such tuning of the interactions may be achieved through suitable selection of surfaces with laterally modulated wettability.

The second part of the thesis deals with the dynamic characterization of cluster diffusion. This includes the implementation of an Atom Tracking (AT) technique, which enables to track the cluster's position on the surface with high lateral precision and high resolution in

time. In this way, the diffusion of Pd_{12} clusters on graphene/Rh(111) could be tracked with an observed movement that permits to relate it to anomalous diffusion of superdiffusive behavior (Lévy flights). Furthermore the influence of tip bias and CO gas dosing on the AT measurements has been tested. The technique opens up new possibilities for investigating cluster diffusion on different length scales, e.g. the graphene Moiré cells (scaled up to 100 nm), but also within the cells (atomic scale). AT measurements at variable temperatures will enable in the future to determine activation energies and entropies and thus to get further insights into the interplay between clusters and substrate.

Zusammenfassung

In der heterogenen Katalyse ist das Sintern von geträgerten, katalytisch aktiven Partikeln eine der Hauptgründe für deren Deaktivierung. Aus diesem Grund beschäftigt sich der erste Teil dieser Dissertation mit der Charakterisierung dieses Prozesses. Die zwei Mechanismen, welche bei diesem Vergröberungsprozess eine tragende Rolle spielen, sind auf der einen Seite Ostwald Reifung, wobei größere Cluster auf Kosten kleinerer Cluster wachsen, und auf der anderen Seite die Smoluchowsky Reifung, bei welcher ganze Cluster über die Oberfläche diffundieren, aufeinander treffen und miteinander verschmelzen. Die Sintereigenschaften der geträgerten Cluster können dabei durch die Wechselwirkung zwischen Cluster und Oberfläche abgestimmt werden. Um die Clusterreifungsmechanismen kontrollierenden, grundlegenden Faktoren zu bestimmen, wurden monodisperse Pd Cluster auf drei verschiedene Oberflächen, welche als Modellkatalysatoren fungieren, dosiert: eine blanke Rh(111) Oberfläche, ein auf Rh(111) und Ru(0001) gewachsener Graphenfilm, sowie eine auf Rh(111) gewachsene Schicht aus hexagonalem Bornitrid. Die Entwicklung der Partikelgröße und Partikeldichte wurde mit hochauflösender Rastertunnelmikroskopie (STM) dokumentiert. Die vorherrschenden mikroskopischen Mechanismen, welche die Reifungsprozesse auf jedem der Substrate steuern, wurden durch sorgfältige Analyse der Clusterhöhe und der Größenverteilung bestimmt. Die Reifungsmechanismen wurden dabei den durch theoretische Berechnungen bestimmten Clusteradsorptionsenergien und Atomablösungsenergien zugeordnet. Die Resultate dieser Studie bringen Licht in die Prozesse, welche bei der Clusterreifung auftreten und führen zur Formulierung einer Strategie, um die Cluster gegen Reifung zu schützen. Diese Strategie beinhaltet eine genaue Kontrolle sowohl der Cluster-Substratbindung als auch der Bindung der einzelnen Atome untereinander. Dies

kann durch geeignete Wahl von Oberflächen mit lateral modulierter Netzbarkeit kontrolliert werden.

Im zweiten Teil dieser Dissertation wird die Untersuchung der Diffusion von Clustern auf dynamische Art weitergeführt. Die Implementierung einer “Atom Tracking” Technik ermöglicht es die Position eines Clusters auf der Oberfläche mit hoher lateraler Genauigkeit und hoher Zeitauflösung zu bestimmen. So konnte die Diffusion von Pd_{12} Clustern, welche auf eine auf Rh(111) gewachsenen Graphenschicht dosiert wurden, beobachtet werden. Die Art der Bewegung deutet auf anomale Diffusion und ein superdiffusives Verhalten hin (Lévy-Flüge). Des Weiteren konnte der Einfluss der an der Spitze angelegten Spannung oder der Dosierung von Kohlenmonoxid auf die Messung untersucht werden. Die Implementierung der “Atom Tracking” Technik öffnet die Tür für weitere Untersuchungen von Clusterdiffusion auf verschiedenen Längenskalen, z.B. die Diffusion über einzelne Moiré Zellen der Graphenschicht hinweg (bis zu 100 nm), wie auch innerhalb von Moiré Zellen (atomare Skala). AT Messungen bei höheren Temperaturen werden es in Zukunft ermöglichen Aktivierungsenergien und Aktivierungsentropien zu berechnen. Dies wird zu einem besseren Einblick in die Wechselwirkung zwischen Cluster und Oberfläche führen.

Introduction

In this thesis, size-selected Pd clusters, which have been deposited on superstructured surfaces, have been characterized in view of their diffusion and ripening properties. After a short introduction into the main experimental methods used in this thesis, in a first part, this characterization is focused on the different ripening mechanisms that act upon heating the substrate. The main objective of this part is to understand how these ripening mechanisms work, how they can be discerned and which diffusing species are responsible for each mechanism. The results from this study have already been published in ChemCatChem in 2013[1]. The respective reprint permission can be found in the end of the thesis. The theoretical calculations for this study have been provided by B. Yoon and U. Landman from Georgia Institute of Technology, Atlanta. As this study results from the statistic evaluation of large scale STM images, it is named static characterization of cluster diffusion and ripening.

In order to get more information on the processes that occur during the ripening of metal clusters on surfaces, the second part of this thesis deals with the dynamic characterization of cluster diffusion and ripening. The main goal of this chapter is to elucidate and explain the cluster's trace over the surface during the diffusion. For this characterization an Atom Tracking technique is used that enables to record the position of the cluster in real time and relate it to the support.

Each of the parts include a description of the state of the art, an experimental part, which gives detailed information about the experimental methods, a presentation of the results of the study and a discussion of these results.

The thesis is completed by a joint conclusion and outlook, and important references are given.

Experimental Methods

Size-selecting cluster source

The size-selected Pd clusters are produced by a dedicated high-frequency laser evaporation cluster source that has been developed by the group.[2] Upon evaporation of the cluster material from a target by a laser pulse of a frequency-doubled Nd:YAG laser, the resulting plasma is cooled down by a He pulse and driven through a nozzle, upon which clustering as well as cooling by adiabatic expansion occurs. The clusters are then driven through einzellenses, an octupole and a bender that selects a specific charge sign (here: cations). The clusters are then size-selected in a quadrupole mass selector and finally deposited on the substrate. The kinetic energy of the impinging clusters was controlled to be low enough (mean kinetic energy of 3 eV, with half-width at half maximum of ~3 eV) so that non-destructive, soft-landing conditions were fulfilled. The clusters were deposited at RT. The cluster density could be controlled by measuring the cluster current and the deposition time. An efficient pumping system reduces the background pressure continuously from the cluster source on, so that deposition can be performed at a base pressure of $1 \cdot 10^{-9}$ mbar, which is mainly due to the He gas pressure. This ensures the cleanliness of the substrate.

Substrate preparation

The Rh(111) crystal was cleaned by repeated cycles of Ar^+ sputtering and consecutive annealing at 1223 K. The graphene monolayer on Rh(111) was prepared by exposing the sample to ethylene ($6 \cdot 10^{-7}$ mbar) for 3 min at 1123 K. An efficient and fast cooling of the crystal after substrate preparation is of utmost importance, because carbon atoms dissolve in the bulk when cooling down. This ensures a perfect substrate qualityand leads to a well-ordered Moiré structure that has been extensively described in the literature.[3]

The h-BN-Moiré structure on Rh(111) was prepared accordingly by exposing the crystal to borazine ($6 \cdot 10^{-7}$ mbar) for 3 min at 1108 K. Structural and theoretical investigations on this nanomesh can be found in the literature.[4]

Scanning Tunneling Microscopy

In the early 1980s Binnig and Rohrer revolutionized the scientific world by inventing a new type of microscope, the Scanning Tunneling Microscope (STM) that enabled scientists to break through beyond the limitation of optical microscopy techniques.[5] Using the quantum mechanical concept of electron tunneling and assuming that a bias difference is applied between a scanning tip and a sample, a tunneling current flows when both are at a very short distance. Due to the fact that the measured tunneling current is extremely distance sensitive, scanning of the surface and regulation of the distance to the current leads to a topographic image of the surface; this predominantly used mode is called constant-current mode. For flat substrates one can also imagine to control the distance and record the tunneling current (constant-height mode).[6]

This new technique opened up the possibility to image very small structures and even atoms, and together with electron miscroscopy the spatial limit of optical microscopy was overcome. STM techniques involve tunneling electrons and high local fields at distances above chemical bond lenght that can provoke molecular motion, enabling additional experiments,[7] like manipulation experiments, but also the forming and breaking of chemical bonds on an extremely local and thus selective level.[8] Whereas the tunneling current integrates over all accessible states from the Fermi level to the applied bias, dedicated spectroscopy measurements based on bias modulation can give further access to the density of states at a given bias.

Our laboratory is equipped with an Omicron VT-AFM, combining STM and AFM, and able to be operated at variable temperatures.

Chapter I:

Static characterization of cluster diffusion and ripening

State of the art

Heterogeneous catalysis is involved in most of the fundamental processes in modern chemical and petrochemical industries, making investigation of catalyst deactivation processes that lead to loss of activity and selectivity and decreased lifetime of the catalysts, both timely and of utmost importance. In general, one may distinguish four main deactivation mechanisms of heterogeneous catalysts: poisoning, coking, phase transitions and sintering. The first three processes can be related to complicated chemical changes, whereas sintering, i.e. particle coarsening, is commonly driven by thermodynamic processes that operate at elevated temperatures,[9] as for example in the case of steam reforming of methane on oxide supported Ni particles at temperatures up to 1300 K.[10] The coarsening of catalytically active particles, often occurring concomitantly with the collapse of support pores or channels at elevated temperatures, results in a dramatic reduction of the active catalytic surface area and a loss of particle size specific properties.[11] Consequently, the activity of the catalyst drops.

The main driving force for catalytic sintering is the minimization of the total surface energy of the system. In contrast to most other deactivation mechanisms, sintering is normally irreversible, cannot be cured, and hence needs to be prevented from the start. Although the sintering rate can be readily assessed in industrial catalytic systems, rather little is known about the molecular mechanisms, as a result of the complex nature of catalytic structures, which often consist of metal particles loaded in, or supported on, porous oxides. In contrast, model catalysts, such as well-dispersed metal clusters on oxide thin films supported on metal/semiconductor single crystals,[12] represent a well-defined chemical environment that can be investigated by surface sensitive techniques.

Two main mechanisms are found to be responsible for cluster sintering (see Figure 1): The first one is Ostwald ripening (OR), where larger clusters grow at the expense of smaller ones. The clusters are supposed to be sufficiently immobile, so that mass transport occurs only by diffusion of atoms (or small intermediates) that detach preferentially from the smaller clusters. This is a consequence of their higher, curvature-dependent, vapor pressure due to the Gibbs-Thomson effect. This phenomenon was first described by Ostwald in 1900 for colloidal systems.[13]

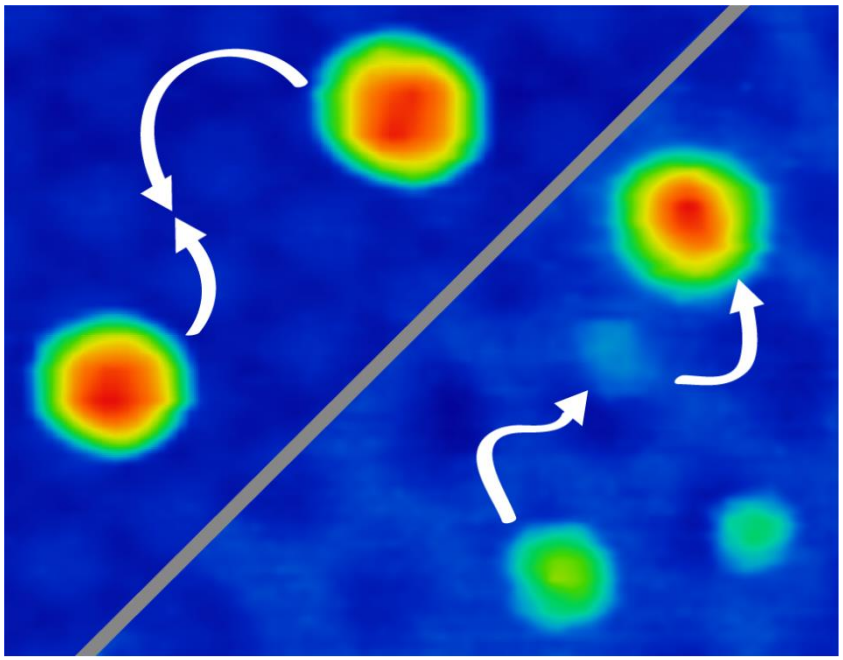

Figure 1. Upper left: Schematic representation of a Smoluchowski ripening process. The clusters are mobile and diffuse over the surface. They eventually collide and merge. Lower right: Schematic representation of an Ostwald ripening process. Mobile species leave a cluster and diffuse over the surface before being catched by another cluster. Larger cluster grow at the expense of smaller clusters.

The second ripening mechanism that we consider involves cluster coalescence, called also Smoluchowski ripening (SR). In this mechanism particle migration and coalescence occur, with entire clusters diffusing over the surface and eventually colliding and merging

into larger clusters. This mechanism was first described by Smoluchowski in 1916 for coagulation processes in colloids.[14]

Theoretical models have been developed for the abovementioned ripening mechanisms to describe the profile of the particle size distribution (PSD), based on an analysis of the particles' dimension over the entire ripening process.[15] In the case of OR, the kinetics of the process can be described by the Lifshitz-Slyozov-Wagner theory (LSW).[16] This theory was originally derived for precipitation and coalescence in solid solutions, but adapted by Chakraverty in order to describe grain size distributions in discontinuous thin films.[17] More recently, Finsy further developed this theoretical approach to predict the PSD profile for the following conditions: (1) the particles are fixed in space, (2) they do not interact, (3) the coverage of the diffusing species is constant outside two radii of the particles, and (4) transport occurs via diffusion between particles.[18] This PSD depends only on the particle diameter, scaled by the average diameter. The OR process can be limited either by diffusion control, where diffusion of the atoms is the rate limiting step, or by interface control, where the detachment of atoms from the clusters is the rate limiting step. In either case the PSD reaches a self-similar shape with a tail in the small diameter regime, resulting from the continuous supply of small clusters. While smaller clusters form on the surface, initially the total cluster coverage (number of particles) remains constant and the maximum of the PSD does not shift significantly.

For the SR mechanism, Granqvist and Buhrman showed that the PSD corresponds to a log-normal distribution function, which is skewed towards higher particle size.[19] Since smaller particles tend to be more mobile, they have a higher probability to sinter and to disappear. This consumption of small particles leads to a sharp cutoff of the PSD function

at lower particle diameters, to an immediate shift of the PSD maximum upon ongoing ripening and to an immediate decrease of the total cluster coverage.

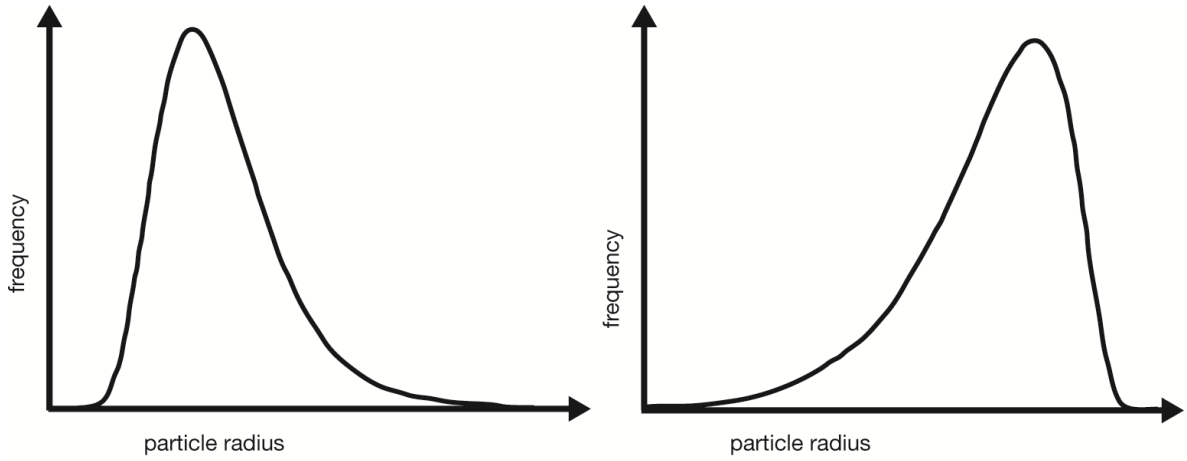

Figure 2. Particle size distribution showing the clusters' normalized dimension after a Smoluchowski ripening (log-normal function, left side, after [19]) and an Ostwald ripening (right side, after [18]) dominated process. The distributions are self-similar when scaling the particle radius on the average value.

The process of SR can either be limited by migration or by coalescence. By calculating the coalescence time for small Pt clusters, assuming that they are spherical and do not wet the substrate, Wynblatt and Gjostein showed that, for particles smaller than 5 nm in diameter, coalescence occurs so fast that migration becomes the rate limiting step.[20]

Over the last decade, several experimental studies were performed to investigate ripening processes on real catalysts as well as on model catalyst systems. We focus here on those studies that attempted to infer from the PSD, which of the two mechanisms was leading to ripening. Datye et al. investigated ripening of technically relevant supported catalysts (e.g. Pd and Pt particles on alumina) by transmission electron microscopy (TEM) and scanning transmission electron microscopy (STEM).[21] While modulating the experimental conditions in such a way as to obtain the OR mechanism or the SR, the resulting PSD were always characterized by a log-normal distribution function with a tail

towards larger particle diameters. The authors concluded that a deduction of the ripening mechanism is not possible just based on the PSD profile. Simonsen et al. used a planar support of amorphous Al_2O_3 to investigate the ripening of Pt clusters by TEM.[22] They showed that the ripening of the particles is mediated by OR and that the shape of the PSD changes during the ripening process sequentially from a Gaussian profile to the distribution predicted by the LSW theory, i.e. skewed towards lower particle size. In contrast to the work of Datye et al., Simonsen et al. concluded that their experimental conditions, i.e. the uniform flat support and the homogeneous initial distribution, were closer to the assumptions made in the LSW model. A more clearly defined model system was adopted by Jak et al. by investigating the growth of small Pd particles on TiO_2(110) using scanning tunneling microscopy (STM).[15a] The prevailing mechanism for ripening in this system is regarded to be SR for several reasons: the cluster density decreases dramatically with time, the PSD obtained at elevated temperatures fits better to a log-normal distribution function, and mobile clusters on the surface are already observed at room temperature (RT). Upon ongoing ripening and formation of large nanoparticles, however, another study on this system by Howard et al. [7b] attributed the ripening process to the OR mechanism.

From the above case studies it gets obvious that the shape of the PSD cannot serve as the only conclusive, discriminating identifier of the ripening mechanism, particularly when starting from an initial broad PSD that convolves with the final PSD resulting from the evolved ripening process.[15a, 21-23] These uncertainties, as well as other factors that complicate the assignment of the ripening mechanism, have been discussed and debated in some detail.[16]

Unlike previous studies, this work starts with truly monodisperse Pd clusters that have been size-selected and soft-landed on highly ordered substrates. This presents the unique advantage of well-defined initial conditions. Furthermore, high-resolution STM is used as a tool for determining the PSD and therefore the full range of cluster sizes can be detected without a lower size bound, unlike TEM studies that have limitations to resolve the smallest particles. To the best of my knowledge, the ripening behavior of size-selected clusters, containing several tens of atoms, has been studied experimentally earlier once, by the group of Kappes. [17] However, that electron microscopy study of the ripening of Au clusters on an amorphous carbon surface lacked control on substrate quality and did not have sufficient lateral resolution to distinguish directly between the OR and SR mechanisms. Furthermore, the diffusion coefficients derived in that study seemed to indicate enhanced OR with increasing cluster size. The authors attempted to explain this contradictory finding by suggesting effects related to the deposition process and cluster-substrate interactions.

Size-selected Pd clusters are deposited on three well defined substrates, i.e., a bare metallic Rh(111) surface, graphene-Moiré films on Rh(111) and Ru(0001), as well as a hexagonal boron nitride (h-BN) film grown on Rh(111). These substrates differ in their atom and cluster adsorption strength; the films are (Moiré) superstructures with laterally modulated wettability of comparable long-range order.[24] The evolution of the ripening processes has been investigated by annealing to different temperatures, in order to deduce the dominating mechanism for each temperature range. Based on highly resolved STM data from the monodisperse cluster samples, we construct PSDs from height histograms. These histograms exhibit peaks that can be assigned to distinct layer heights, unlike e.g. high quality STEM data, where, most often, continuous distributions are observed (see e.g. Simonsen et al.[22]). The resolution obtained in the experiment thus

allows for studies of the transition between various ripening regimes with unprecedented detail. These experiments, in conjunction with first-principles density functional theory (DFT) calculations, allow to gain important insights into the structural and energetic factors that govern the operative atomic-scale mechanisms of mass-transport and ripening.

The first chapter is organized as follows. Firstly the experimental and computational techniques are presented in the experimental approach. In the next section the results of the ripening studies are presented and discussed. This section will start with a system of Pd clusters deposited on a bare Rh(111) surface, showing OR processes already at room temperature. Investigations of Pd clusters adsorbed on a Moiré-patterned g/Rh(111) film that exhibits ripening following the SR mechanism for temperature up to 600K will follow. Between 600K and 700K, a crossover to the OR mechanism is observed. In comparative experiments on the coarsening of Pd clusters on a g/Ru(0001) surface, the SR processes are somewhat damped because of stronger binding to the surface (compared to the g/Rh(111) surface), and the crossover to the OR mechanism occurs at a lower temperature compared to the aforementioned g/Rh(111) case. Lastly, results for Pd clusters are presented, which have been deposited on a g/h-BN Moiré-film where the strong interaction between the adsorbed Pd clusters and the substrate suppress completely cluster diffusion and coalescence and where coarsening is found to occur via the OR mechanism.

Experimental approach

Experiments

All STM images of the clusters have been taken with extremely low scan velocities in the order of ≤100 nm/s, low bias magnitudes of ≤1 V and low tunneling currents, in order to minimize the interaction with the tip. On the graphene substrates, particularly low tunneling currents of 1 pA had to be chosen. The low scan velocities require extreme imaging stability: In order to investigate large areas with statistical relevance, as in figures 7 and 9, the imaging conditions have to remain stable during several hours. Tip convolution effects lead to apparent lateral dimensions much larger than the real ones, whereas the cluster height determination (topographic maxima) is accurate, with an overall precision down to the tenth of an Angstrom. The indicated histograms are therefore based on the cluster height analysis, in contrast to diameter or area usually indicated in TEM studies. The histograms are gained from large-scale images (≥15000 nm^2), where initially several hundreds of clusters are present, while sufficiently dilute cluster concentrations are maintained (10^{12}-10^{13} cm^{-2}). In this study the Rh(111) terraces were large enough, so that the considered clusters all lay on the same terrace. Different terraces would have required an additional correction step in order to relate the height of the cluster to the corresponding terrace. The vertical scale has been calibrated by the step height of Rh(111), 2.20 Å.

The images have been corrected by subtracting a plane and by aligning the median values of adjacent horizontal rows. After automatic particle detection based on a fixed threshold, the height distributions of the clusters have been determined in two different ways:

The g/Rh(111) sample shows a rather smooth, undulated topography on which also minima can be reliably mapped by the STM tip. Here, horizontal profiles (of ±3 nm length) have been taken that cut through the cluster maxima. The cluster height is then determined as difference between height profile maximum and profile minimum.

The h-BN/Rh(111) surface, instead, shows a flat topography with steep holes that have a flat bottom. This bottom cannot be easily imaged by the STM tip and, if the film is not perfect, as in this study, is measured with a depth that depends on the diameter of the hole. The cluster height is therefore determined by referencing the cluster maxima to the overall mean height of the surface around the clusters. Such a reference is reliable since the background correction works perfectly on the whole imaged area (see Fig. 7). Due to the much stronger interaction of the clusters with this substrate and since the film was not perfectly uniform, the histogram shows not the well-separated peaks observed for g/Rh(111). However, peak maxima in the height distribution can be assigned to layers, if a height of one layer is assigned to the smallest clusters that appear in the 700 K histogram (which is consistent with the observation that OR occurs). The thus required upshift in the height values of 1.3 Å is larger than the depth of the h-BN holes of 0.6 Å that has been calculated by *ab initio*-DFT[4b] and might be related to electronic effects.

Theory

Calculations were performed by B. Yoon and U. Landman (Georgia Institute of Technology, Atlanta) using the VASP-DFT package, with a plane-wave basis (kinetic energy cutoff of 400 eV), PAW pseudopotentials,[25] and the PW91 generalized gradient approximation (GGA) for the exchange-correlation potential.[26] Since the unit cell used here is rather large, a single k-point sampling of the surface Brillouin zone (SBZ) at Γ has been used in most of the calculations; in previous calculations of graphene adsorbed on

Ru(0001), employing the same unit cell (but with the lattice parameter of Ru) it has been checked that the results remain essentially the same by employing (3x3x1) sampling of the SBZ.[24b] In optimization of the various structures, convergence was achieved for forces smaller than 0.001 eV/Å. The Rh(111) surface consisted of 3 layers with the optimized Rh lattice parameter a=2.707 Å, agreeing with the experimental value (a=2.689 Å); in structural relaxations the bottom layer of the substrate slab was held fixed. In simulations of the adsorption of Pd_{19} clusters, the supercell had an (11 × 11) lateral periodicity of the 3-layer Rh(111) slab, a (12 × 12) layer of graphene, and a vacuum region which was taken large enough to ensure no interaction between periodic replicas; for the bare Rh(111) system, the vacuum region was taken as 20.7 Å. for the bare g/Rh(111) system, the vacuum region was taken as 19.7 Å, and it was 16.3 Å when a 2-layer Pd_{19} cluster was adsorbed at the r-hcp site. The relaxed configuration of the (11 × 11) structure exhibited a strong vertical modulation of the epitaxial graphene layer, with the highest C atom lying 3.88 Å above the underlying Ru topmost layer and the lowest-lying C atom located at a distance of 2.06 Å, resulting in a height modulation of 1.81 Å.

Results and Discussion

Pd clusters on Rh(111)

In the first part of this section the focus is on the ripening of metal clusters deposited on a pure metal substrate. Metal substrate are believed to show a strong binding that could prevent the ripening of cluster, but as it is shown in the following, the opposite is the case. Fig. 3 shows a series of STM images of Pd_{19} clusters deposited on Rh(111).

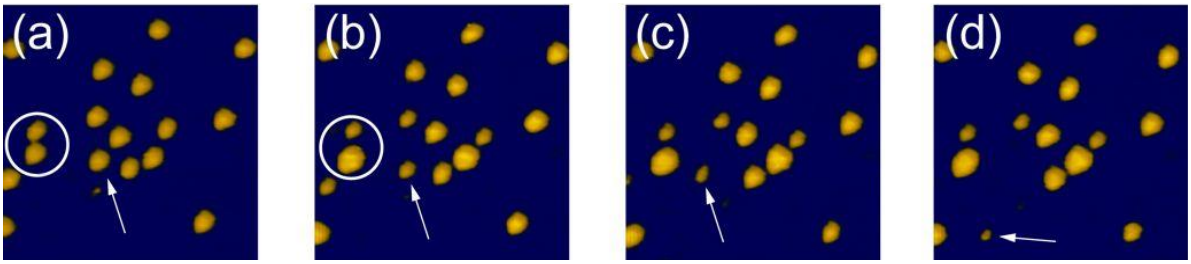

Figure 3. Ripening of Pd_{19} on Rh(111). (a) STM-image of Pd_{19} right after deposition at RT, (b) after 7h 38 min, (c) after 17h, (d) after 17h 45 min. The clusters coarsen by Ostwald ripening: Some get larger at the expense of smaller ones (see circle), whose mobility increases dramatically when below a certain size (see arrow). Image size: 25 × 25 nm^2. Imaging conditions: +1.0 V, 80 pA.

Fig. 3a displays the topography of the surface after deposition. The Pd_{19} clusters appear as 1-layer-high protrusions that have all similar shape. The relatively low coverage ($25 \cdot 10^{-3}$ clusters/nm^2) has been chosen in order to prevent cluster collisions and merging already at deposition and thus to assure the monodispersity of the sample. The finding of a two-dimensional (2D), 1-layer-high structure of the Pd_{19} clusters adsorbed on the bare metal surface is supported by first-principles calculations that were performed by B. Yoon and U. Landman at Georgia Institute of Technology, Atlanta. Indeed, these calculations have shown (see Fig. 4) that the optimal geometry of the adsorbed cluster on the Rh(111) surface is 2D (Fig. 4a), with the three-dimensional (3D), 2-layer isomer (Fig. 4b) having a significantly higher energy (5.95 eV).

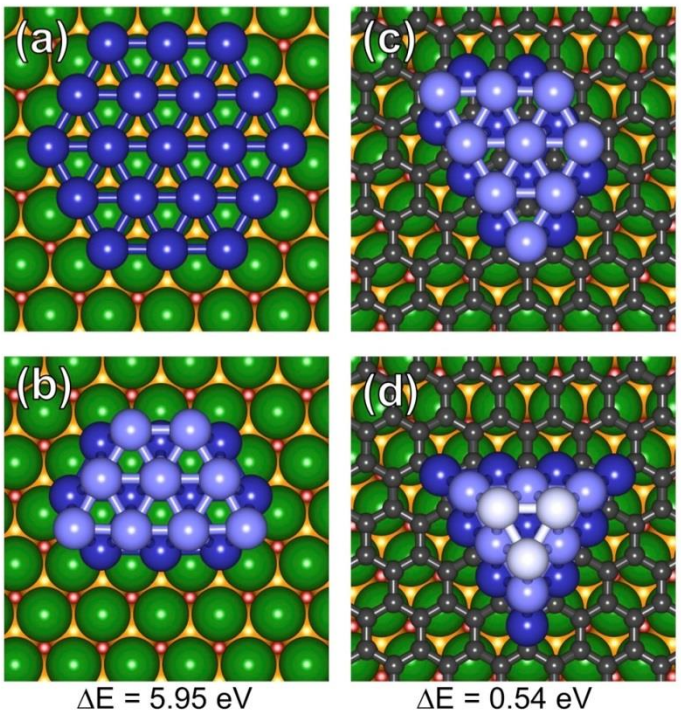

Figure 4. Optimized atomic configurations obtained from first-principles DFT calculations for Pd_{19} clusters on bare Rh(111) (a-b) and on g/Rh(111) (c-d). On Rh(111), the most stable configuration is 2D (1-layer) (a), whereas the 3D (2-layer) configuration is 5.95 eV higher in energy (b). On the r-hcp sites of g/Rh(111), 3D structures are preferred, with a most stable configuration of 2 layers (c), whereas the 3-layer configuration is only 0.54 eV higher in energy (d). Rh substrate atoms are depicted by large green spheres (first layer), resp. orange (second layer) and red spheres (third layer). Carbon atoms of the graphene-Moiré film are depicted by small dark grey spheres (c-d). Pd cluster atoms in direct contact with the underlying surface are depicted by dark blue spheres, resp. light blue (second cluster layer, b-d) and white-blue spheres (third cluster layer, d). The calculations have been performed by B. Yoon and U. Landman (Georgia Institute of Technology, Atlanta).

The STM images in Fig.3 b-d show the effects of the ripening process over several hours under ultra-high vacuum (UHV) conditions at RT. The measurement was maintained stable enough to observe the same area over a period of 12 hours. About 7 hours after the deposition, some Pd clusters have grown in size, whereas others become smaller. The most prominent example of one cluster shrinking and another growing in size are the two adjacent clusters marked by a circle (Fig. 3a,b). Whereas the large Pd clusters stay

immobile during the ripening process, the shrinking cluster marked by an arrow moves from its position after 17h and starts to diffuse over the surface. The time interval between Fig. 3c and Fig. 3d is only 45 minutes, showing the dramatic increase of the cluster mobility.

From the time series of Fig. 3, one can confidently conclude that OR takes place already at room temperature (RT) since one can clearly observe Pd clusters in the vicinity of each other, where one cluster grows at the expense of the other. The fact that we see only 1-layer-high clusters results from the strong metallic binding of the Pd cluster atoms to the Rh(111) substrate. Note that this strong binding does not prevent the ripening process: At the periphery of the 2D cluster, single Pd atoms may detach from the cluster with a relatively small energy cost of ~0.8 eV (see Fig. 5a,b; Calculations by B. Yoon and U. Landman).

These observations are in accord with investigations of similar metal supported metal cluster systems.[27] This 2D detachment (evaporation) of material leads to the nearly complete dissolution of some clusters, as for example the one indicated by an arrow in Fig. 3. As soon as the shrinking clusters reach sizes of roughly 5 atoms, they become much more mobile. This mobility indicates that it is not the diffusion, but the detachment process of the transporting species that is limiting the OR. These findings are supported by other examples of homogeneous and heterogeneous metal on metal studies that predict a decrease of the binding energy of clusters once they contain less than 6 atoms;[28] consequently the mobility of the cluster increases.

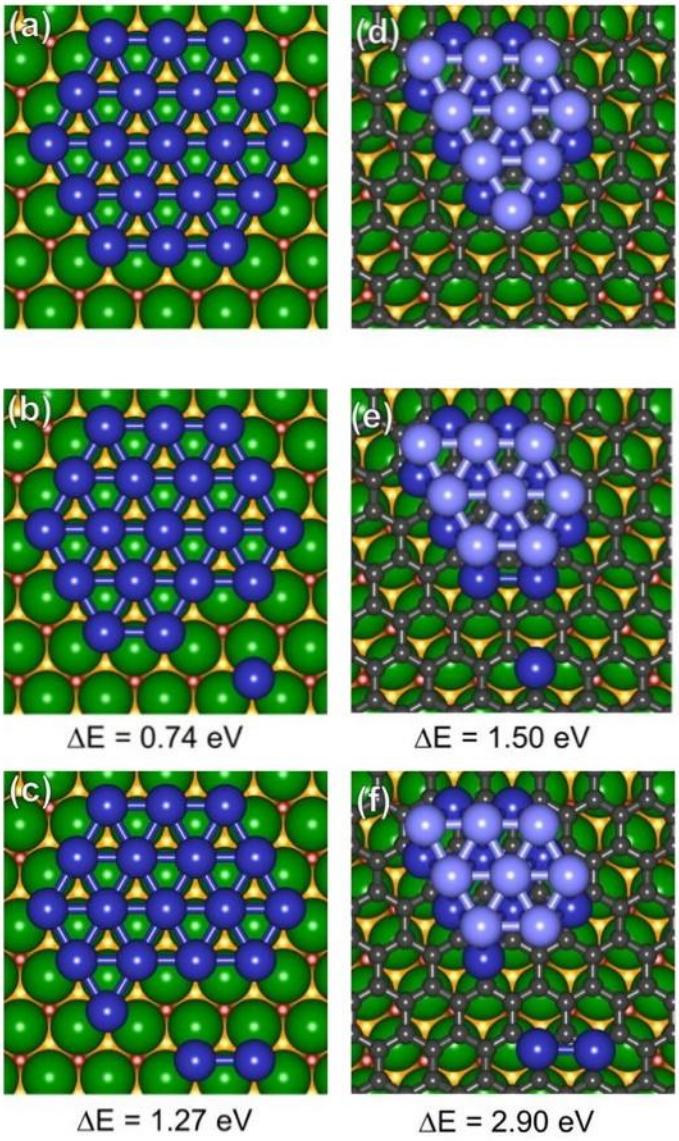

Figure 5. Optimized atomic configurations obtained from first-principles DFT calculations for Pd_{19} clusters on bare Rh(111) (a-c) and on g/Rh(111) (d-f). Starting from the most stable configurations (a, c), we show the atomic configuration corresponding to the lowest-energy single-atom (b, e), resp. dimer detachment process (c, f). The single-atom detachment process on Rh(111) entails a transition state barrier of 0.89 eV, encountered 0.6 Å prior to reaching the local energy minimum shown in (b); over all the atom covers a distance of 2.55 Å with respect to the initial configuration, and the final configuration is higher in energy by 0.74 eV. The corresponding detachment of a Pd dimer entails a total energy increase of 1.27 eV (c). In contrast, the single-atom detachment process on g/Rh(111) leads to an atom displacement of 2.63 Å prior to reaching the local energy minimum shown in (e); the final configuration is higher in energy by 1.50 eV, which is twice the value encountered for single-atom detachment from the cluster adsorbed on the bare Rh(111) surface. The detachment of a Pd dimer from the Pd_{19} cluster on g/Rh(111) entails even a total energy increase of 2.90 eV (f). Color legend see Fig. 2. The calculations have been performed by B. Yoon and U. Landman (Georgia Institute of Technology, Atlanta).

Fig. 6, taken at a slightly increased temperature of 308 K, shows in three consecutive STM topographs, taken with 6 minutes intervals, a shape transition of the larger cluster to a quasi-hexagonal shape, whereas the smaller cluster in the lower part of the image reversibly changes from a triangular to a truncated triangular shape and back. When deconvolving the STM tip shape from the cluster topography, one can estimate the Pd cluster to consist of about 15 atoms arranged in a triangular manner, as indicated by a comparison between the cluster profile and a ball model of Pd_{15} in Fig. 6a (see the triangular 2D cluster at the bottom right).

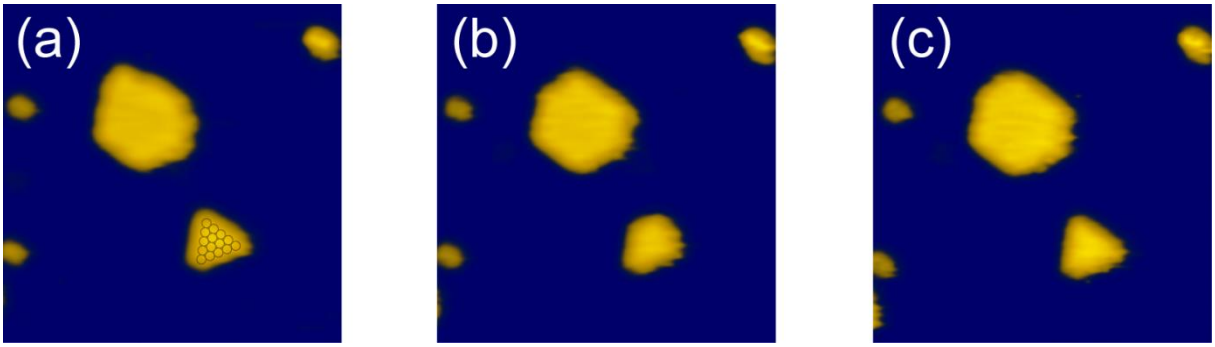

Figure 6. Pd clusters on Rh(111). Cluster shape fluctuations during the ripening process at 308 K. The lower cluster changes from a triangular (a) to a truncated triangular (b) and back to a triangular shape (c). As a guide to the eye and considering the tip convolution effect, an atomic model of the lower cluster has been added to (a). Image size: 10 × 10 nm^2. Imaging conditions: -1.0 V, 100 pA. Time step between consecutive images: 6 min.

Compared to the initially deposited Pd_{19} clusters, the triangular Pd cluster decreased in size whereas the quasi-hexagonal cluster took up atoms (through detachment from smaller clusters) and became considerably larger than Pd_{19}. The shape changes during the ripening of 2D clusters observed in Fig. 6 are facilitated by the weaker Pd-Pd binding at the cluster periphery compared to the stronger binding of the cluster to the substrate. A hexagonal (111) surface of an fcc crystal, such as Rh, can expose two kinds of steps, A

and B, that differ in their direction with respect to the underlying layer. Triangular islands can thus be oriented in two ways, differing by an angle of 60 degrees. The assignment of a particular step type can be achieved by comparing the single crystal directions of the Rh substrate with the registry of a superstructure, like the graphene-Moiré film discussed in the next section. This leads to the conclusion that the triangular cluster in the lower part of Fig. 6 is delimited by A-steps. This shape appears already immediately after deposition. The presence of triangular islands, confined by A-steps and in concomitance to hexagonal islands, is similar to the findings for atomically deposited metal-on-metal systems in the same temperature range, where kinetic limitations have been postulated and where the preference for A-steps has been explained by the slower diffusion of atoms along B-steps.[29] The same kinetic limitations might apply in this case.

From the above one can conclude that for Pd clusters on Rh(111), the ripening of the monodisperse clusters proceeds already at room temperature by OR, exhibiting pronounced shape fluctuations during the process.

Pd clusters on graphene/Rh(111)

The next focus is on results obtained for Pd_{19} clusters deposited on g/Rh(111), that is a graphene-Moiré film supported on Rh(111). The g/Rh(111) film was formed by catalytic dehydrogenation of ethylene adsorbed on the Rh(111) surface at high temperatures (see Methods section). Due to mismatch of the lattice constants of graphene and Rh(111), a Moiré superstructure, comprised of (12 × 12) carbon unit cells on (11 × 11) Rh unit cells, with an approximate periodicity of 3.0 nm has been observed. The topographic and electronic structure of such graphene-Moiré structure has been investigated both experimentally and theoretically.[3b] The surface appears in the STM images with a corrugation of up to 0.6 Å, with the maxima corresponding to positions where the

graphene rings are centered on-top of a substrate atom (r-top), and the minima to positions centered on hollow sites (r-fcc and r-hcp), where the graphene interacts more strongly with the metal substrate. The latter areas are prone to cluster adsorption, whereas at the former locations the interaction with the metal clusters is relatively weak.[24b, 30] This spatial variability of the interaction between the cluster and the underlying graphene surface gives rise to a superstructure with laterally modulated wettability. For the assignment of the high-symmetry locations in a structural model see e.g. Wang et al.[3b]

Fig. 7 shows an STM image of a g/Rh(111) sample dosed with Pd_{19} clusters at RT under soft-landing conditions. In the STM image taken at 300 K, a perfectly grown graphene-Moiré film decorated with Pd_{19} clusters can be observed. The cluster coverage is $18 \cdot 10^{-3}$ clusters/nm^2 (around 7% with respect to the number of Moiré supercells).

From the image in Fig. 7 it is apparent that mainly two different cluster heights occur, and that the higher clusters appear wider due to a larger tip convolution effect. Since tip convolution does not affect the height determination obtained from the STM topography, cluster heights can be measured reliably with a precision down to around 0.1 Å. Extensive height statistics have been accumulated, for at least 80 clusters/sample. The resulting height histograms, normalized to relative frequencies, are shown in Fig. 8 and serve as PSD of the clusters present on the surface. The noticeable bimodal cluster height distribution observed in the image at 300 K (Fig. 7) is distinctly mapped in the corresponding histogram. The two cluster heights are attributed to two types of isomers of Pd_{19} that are 2- and 3-layers high (similar to the case for g/Ru(0001)[24b]).

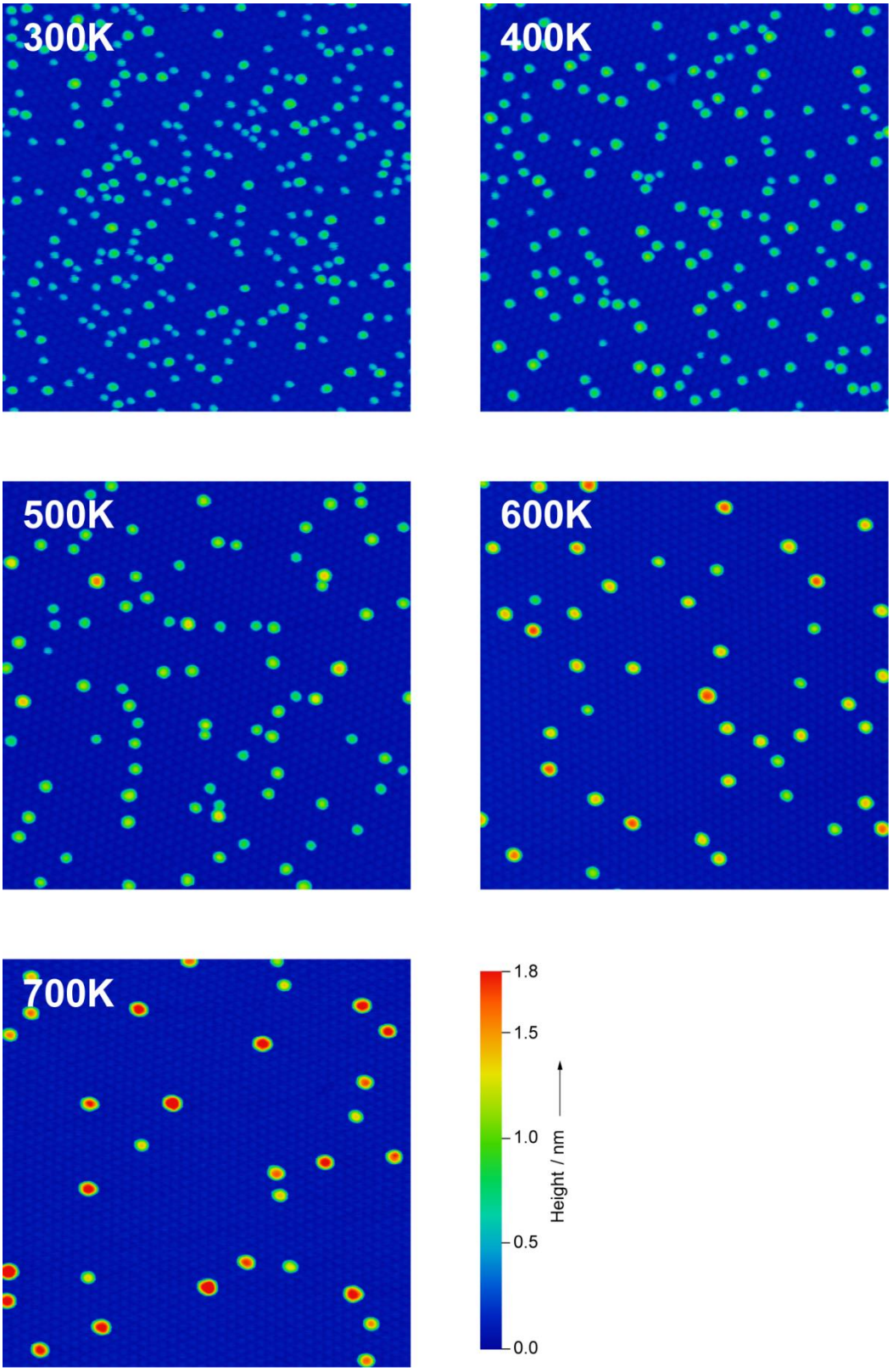

Figure 7. Ripening of Pd19 clusters on g/Rh(111) upon sample annealing during 5 min. to the indicated temperatures; images have been taken at RT. Image size: 120 × 120 nm². Imaging conditions: +0.5 V, 1 pA.

The layer distance of 2.5 Å, marked in the histograms by dashed lines, is comparable to the diameter of Pd in the bulk, but larger than the step height on a Pd(111) surface. The peaks in the histogram indicate that the clusters have layered structure starting already at small sizes. Anyhow, the smaller 2- to 3-layer-high clusters show also some intermediate intensity between two neighboring peaks in the histogram. This may indicate that there are more than just two isomers, which show different electronic coupling to the substrate. However, these differences are of diminishing influence for larger clusters. Upon closer examination of the STM image one can observe that the Pd_{19} clusters are exclusively bound to ring-hollow sites of the Moiré superlattice, with roughly equal probability in r-hcp and r-fcc.

The above observations are supported by the results of our calculations, see Fig. 4c,d. Here 2- and 3-layer Pd_{19} clusters adsorbed on g/Rh(111) at the r-hcp site are shown. These two 3D surface-supported isomers are predicted to be separated by a relatively small energy (0.54 eV). We can summarize these findings by concluding that on the supported graphene film, the Pd_{19} clusters do not completely wet the surface but tend to keep a 3D structure as a consequence of the stronger binding within the cluster compared to the cluster interaction with the substrate; this effect has been discussed previously for Pd_{19} and Pd_{20} adsorbed on g/Ru(0001).[24b] The experimental observation of 2- and 3-layer clusters is in agreement with the small energy difference found in the calculations. Further DFT results can be found in the Supporting Information of reference [1].

Upon successive annealing for 5 minutes to increasingly higher temperatures in steps of 100 K and subsequent measurements by STM at RT, one can observe in the STM images (Fig. 7) a growth in the cluster height, accompanied by a decrease in the cluster number.

Note that the images in the sequence are all of the same size and are representative cutouts taken from (at least) six fold larger images. After the final annealing to 700 K, only a few very large clusters remain on the graphene surface. The whole process, displayed in the histograms of Fig. 8, is manifested by a continuous shift of the PSD maxima and their lower onset to larger cluster heights. In concomitance, the cluster coverage, depicted as horizontal bars, diminishes dramatically with each annealing step: At 400 K, already two thirds of the initial coverage have disappeared, while the corresponding PSD shows a clear decrease of the 2-layer clusters. 3-layer clusters start to dominate and the first 4-layer clusters appear. This shift to larger sizes continues at higher annealing temperatures, with the PSD remaining similar in shape at 500 K, slightly broadening at 600 K and strongly broadening at 700 K. Throughout this process, the cluster coverage continues to drop considerably until only roughly one tenth of the initial cluster coverage is left.

From these observations, it is evident that the surface has undergone a ripening process. The continuous shift of the maximum of the height distribution to higher values, the sharp distribution cutoff at low values and the tail at high cluster heights, as well as the immediate change in cluster coverage upon annealing, point unequivocally to an SR mechanism. The corresponding log-normal distribution curve[19a] has been tentatively fitted to the PSD after annealing to 500 K and indicates clearly a high particle-size tail. Further support to the suppression of the OR process and the emergence of SR as the dominant ripening mechanism on this graphene film comes from the results of our first-principles calculations. Indeed, these calculations predict for the 2-layer Pd_{19} cluster adsorbed at the r-hcp site on g/Rh(111) relatively high monomer and dimer detachment energies (1.5 eV and 2.9 eV, respectively, see Fig. 5e,f). These high detachment energies

inhibit the onset of OR, at least up to relatively high temperatures (see following discussion).

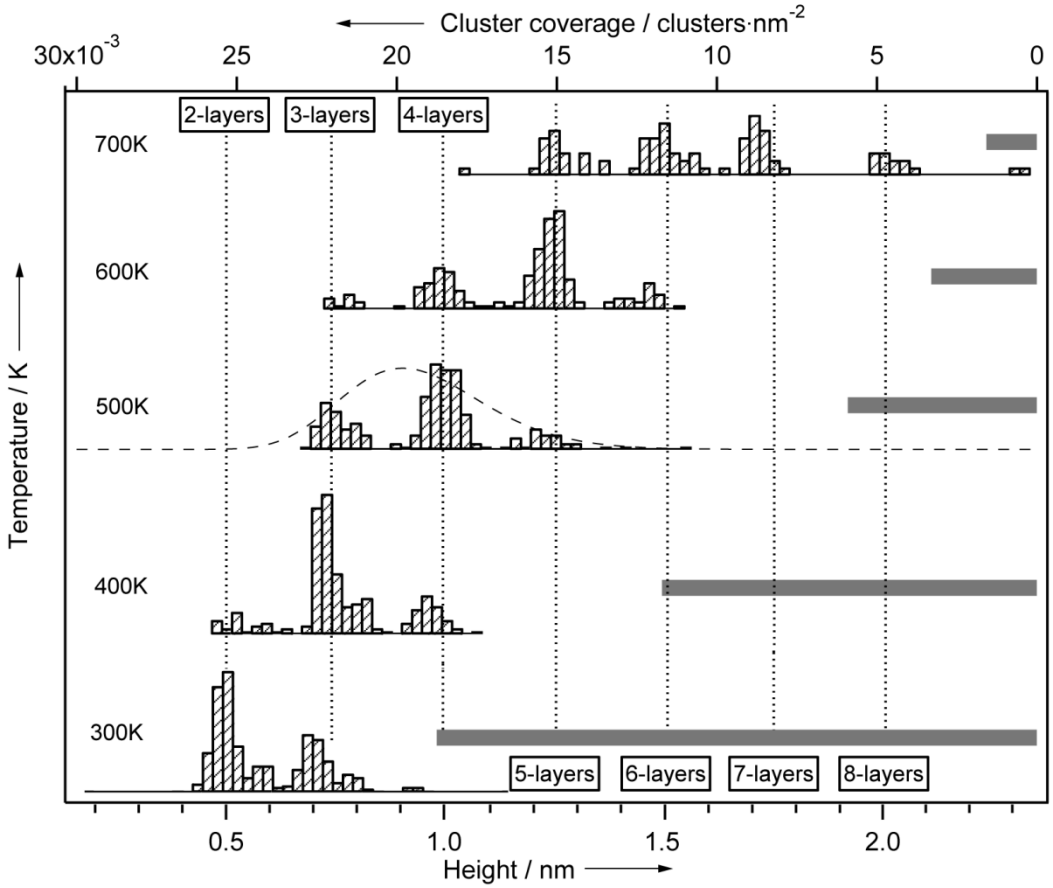

Figure 8. Bottom axis: Particle size distributions corresponding to the images of Fig. 7. The PSDs are obtained as height histograms, normalized to relative frequencies; the analyzed surface areas are larger than the shown cutouts and correspond to 120 × 180 nm² (300 K and 400 K), 160 × 240 nm² (500 K) and 200 × 300 nm² (600 K and 700 K). Distinct layer peaks are resolved. As a guide to the eye, the 500 K data is fitted by a log-normal function after Granqvist.[19a] Top axis: Cluster coverage observed for each annealing temperature, represented by grey bars. The PSDs' shift to larger cluster size, their sharp lower-edge cutoff and the loss in cluster coverage indicate that an SR mechanism is dominant for annealing temperatures up to 600 K; thereafter OR takes over.

The cluster distribution broadens significantly only after annealing to 700 K, which indicates an onset of the OR mechanism between 600 K and this temperature. However, small clusters could not be observed after annealing, possibly due to the high mobility of

the smaller clusters at elevated temperatures, leading to their disappearance before the sample has cooled down to RT. At these moderate maximal annealing temperature, desorption of Pd atoms is unlikely to occur.

The SR mechanism implies subsequent formation of increasingly large clusters, with increasing adhesion to the surface and hence decreasing diffusion propensity. Whether this increasing adhesion is limited to a critical footprint size, is a topic in the thesis of Michael König and can be followed there.[31]

The above observation of the onset of an SR process much prior to the OR mechanism, is rather unique. One can estimate the stability of particle-assembled catalysts on weakly interacting supports based on the empirical Hüttig temperature that states atoms to detach from kinks and edges at a temperature of around 30% of the melting temperature,[32] and consequently OR to be expected from this temperature on. Based on this rule-of-thumb, one may expect OR to set in for Pd particles at about 550 K, which is close to that found in our measurements.

In order to disentangle the contributions from SR and OR by a mild suppression of the SR process, the cluster adsorption energies have to be increased. For this purpose the ripening on g/Ru(0001) was studied. This support shows a Moiré structure of similar periodicity and corrugation to that found on the g/Rh(111) surface, but is characterized by a somewhat stronger interaction with deposited Pd clusters (with the binding energy of Pd_{19} calculated to be ~0.6 eV higher on g/Ru(0001)). Due to the higher activation needed for cluster migration on the g/Ru(0001) surface, the SR on this surface is damped, compared to that found on the g/Rh(111) at comparable annealing treatments. Thus, at 500 K, the PSD of Pd clusters on the g/Ru(0001) surface peaks at 3 layers, whereas on the g/Rh(111) surface clusters of up to 5 layers had already formed at that temperature.

At 600 K, a broadening of the PSD characteristic for the OR mechanism is clearly observed on g/Ru(0001); that is, at a temperature that is about 100 K lower than on g/Rh(111) (see Fig. S1 in the Supporting Information of reference [1]). Additionally, clusters of smaller heights are observed in the broadened PSD, and the cluster coverage remains unchanged during annealing at 500 K and 600 K, whereas it decreases again only after annealing to 700 K, when the smaller clusters have disappeared.

One can conclude that the higher binding energies of the Pd clusters to the g/Ru(0001) surface underlie a suppression of the SR mechanism, so as to maintain a population of smaller clusters at corresponding applied annealing temperatures. Since smaller clusters have a higher vapor pressure due to the Gibbs-Thomson effect, OR is observed earlier, that is at a lower annealing temperature compared to the aforementioned g/Rh(111) case.

The stronger binding of the Pd clusters to g/Ru(0001), compared to g/Rh(111), could be substantiated by the calculations: the adsorption energies of the Pd_{19} cluster for the two systems are, respectively: 6.12 eV and 5.51 eV, that is the cluster binding to the g/Ru(0001) surface is stronger by 0.61 eV. These energies have been calculated by B. Yoon and U. Landman as $[E(g/M) + E(Pd_{19})] - E(Pd_{19}/g/M)$, where E(x) is the total energy of the indicated system, M is either Ru(0001) or Rh(111). Note that $E(Pd_{19})$ is the total energy of the isolated Pd_{19} cluster in the corresponding optimized adsorbed configuration.

Upon the onset of OR, one would expect to observe a relative abundance of very small clusters that result from shrinking (as a result of atom detachments). On the g/Ru(0001) substrate, this occurred rarely and on the g/Rh(111) it was impossible to observe. Although small clusters may have formed on the g/Rh(111) surface, the dominance of small cluster diffusion at high temperatures prohibits in-situ measurements; when

studying the samples with STM at RT after the annealing stage, aggregation has already taken place.

The cluster-surface interaction can even be further increased by switching to the isovalent substrate, hexagonal boron nitride, where the two carbon atoms of the graphene unit cell are replaced by boron and nitrogen.

Pd clusters on h-BN/Rh(111)

A hexagonal boron nitride film was prepared by catalytic dehydrogenation of borazine at high temperatures on Rh(111). This leads to the formation of a Moiré superstructure with a periodicity of about 3.2 nm, corresponding to a coincidence lattice of (13 × 13) h-BN units on (12 × 12) Rh unit cells.[4a, 33] This superstructure appears as a 1-layer mesh with around 2 nm wide pores, which host the deposited clusters and are known from literature to be good trapping centers for molecules and clusters.[24a, 34]

To gain further insight about the mechanisms of cluster ripening on this substrate, the h-BN/Rh(111) sample dosed with Pd_{19} clusters was investigated by STM at RT and after annealing the sample to 500 K and 700 K respectively. Similar to Figs. 7 and 8, Fig. 9 shows three STM images and the corresponding height histograms. The initial coverage of the clusters was $8.5 \cdot 10^{-3}$ clusters/nm^2 (around 4% with respect to the number of Moiré supercells); the sample was cooled down to RT before scanning.

From the STM images of Fig. 9, one can observe that, over the temperature range of our study, the clusters on h-BN/Rh(111) do not grow in height as noticeably as on the graphene substrates discussed above. However, in contrast to the graphene substrates, a considerable amount of very small particles appear at 700 K. A closer examination of

the STM images reveals that the clusters are located inside the pores and are mostly adsorbed at their rim.

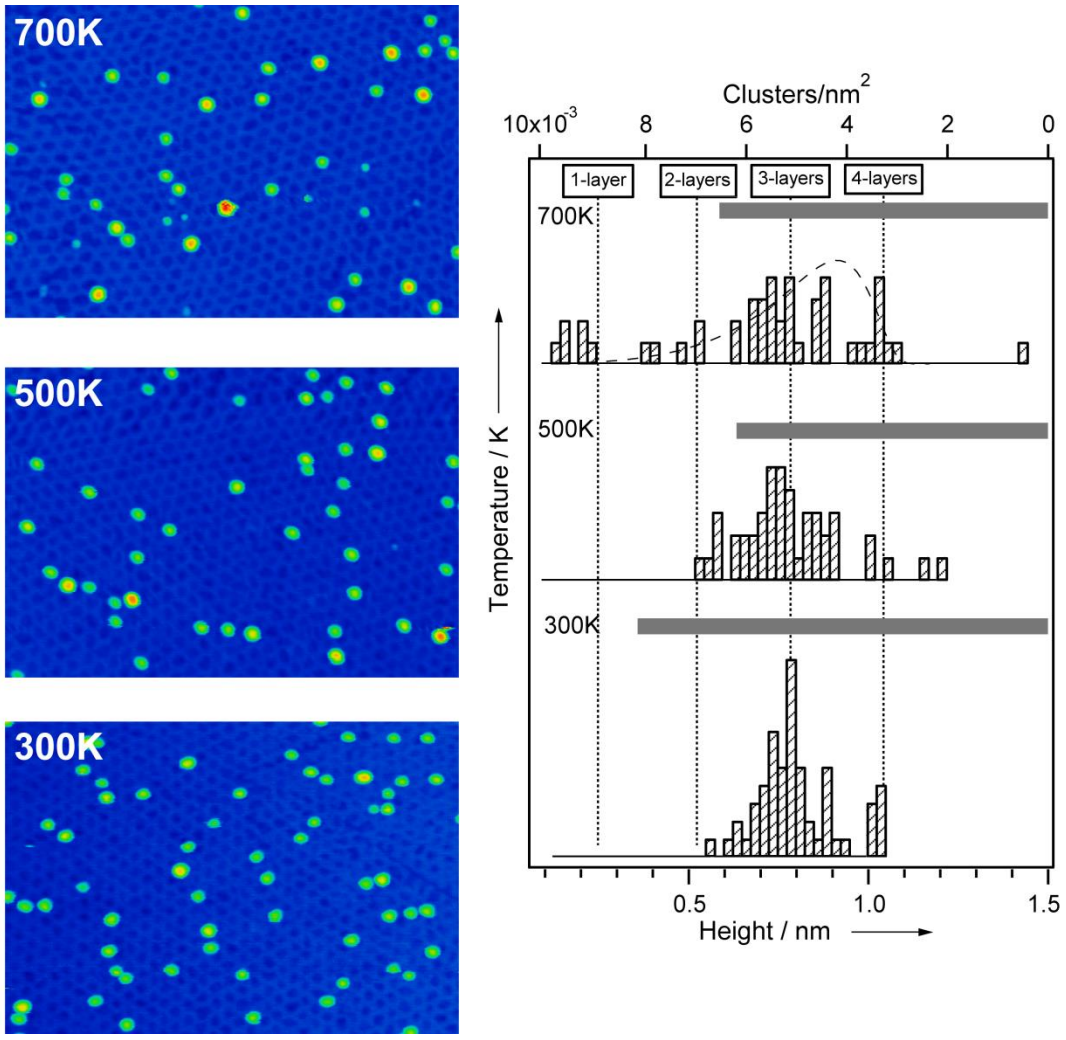

Figure 9. Left: Ripening of Pd_{19} clusters on h-BN/Rh(111) upon sample annealing during 5 min. to the indicated temperatures. Image size: 75 × 100 nm^2. Imaging conditions: +1.0 V, 1 pA. Right: (bottom axis) Particle size distributions corresponding to the images on the left, obtained as height histograms, normalized to relative frequencies. As a guide to the eye, the 700 K data is fitted by the model of Finsy.[18] The color scale used for the images is indicated at the bottom. (top axis) Cluster coverage observed for each annealing temperature, represented by grey bars. The cluster coverage is not decreasing as much as for the graphene-Moiré samples. The PSDs' broadening, without a shift, and the almost constant cluster coverage indicate an OR mechanism.

When analyzing the corresponding height histograms (Fig. 9, right hand side), it gets obvious that the maxima of the PSDs do not shift to larger cluster heights. Whereas the PSD does not change much upon annealing to 500 K, it broadens at 700 K and now small 1-layer-high clusters are also observed, both in the histogram and in the corresponding STM image. The different layers do not appear as well separated in the histogram as for the g/Rh(111) supported cluster sample (Fig. 8), since the h-BN film is not as uniform and regular as the graphene films and since the binding and electronic interaction with the substrate is stronger (see discussion in refs. Dil et al.[34]). The maximum of the PSD is always about 3 layers, but already at 300 K also 2- and 4-layer clusters are present. Both the STM images and histograms, show that the coverage remains essentially constant over the whole temperature range, within the limits of precision of our coverage determination; the Pd clusters are thus much more stable on h-BN/Rh(111) than on the graphene superstructures.

This result indicates that the binding of the Pd clusters to the h-BN/Rh(111) substrate is sufficiently strong as to essentially suppress SR. The broadening of the PSD at 700 K, as well as the constant cluster coverage, are strong indications for OR. The histogram obtained after annealing to 700 K can be tentatively fitted to the distribution profile proposed by Finsy[18] and shows a tail towards low particle diameters predicted for the OR mechanism. The increased presence of small particles might partly also be related to a footprint-related trapping at defect sites; for this reason, clusters of this type were not included in the fit.

Discussion

In this study two ripening mechanisms of size-selected Pd clusters adsorbed on solid surfaces are explored: Ostwald and Smoluchowski ripening. With atoms taken as the mass-transport agents in the OR mechanism, two possible rate-limiting processes may be considered: (i) Interface control, where the rate-limiting step involves the detachments of atoms from the smaller clusters, and (ii) diffusion control, where the rate is governed by the surface diffusion of the atoms. Since the barriers for atom diffusion are relatively low on the metal surface[28b, 35] as well as on the epitaxial graphene surface (both local, single-step site-to-site hopping barriers, and global diffusion barriers from one Moiré cell to the next),[24b] one can conclude that the detachment of atoms from the clusters is the operative rate-limiting process of the OR mechanism.

For the OR to dominate over the SR mechanism, the following conditions have to be fulfilled: First, the binding of the clusters to the substrate has to be sufficiently strong to anchor them at their adsorption sites. This condition is fulfilled here for the metal-on-metal system, based on the observation that the gas-phase 3D clusters transform to 2D islands and wet the metal substrate upon deposition and adsorption (see Fig. 3 and Fig. 4a,b). On h-BN/Rh(111), the binding of the clusters to the substrate is enhanced by the additional trapping potential at the rims of the pores.[34a] Second, the atom detachment energy of the cluster has to be low enough, so that atoms can leave the cluster. The relatively low energy value of ~0.8 eV, obtained from our first-principles calculations for atom detachment from the interfacial periphery of the 2D Pd_{19} island adsorbed on bare Rh(111), is consistent with this requirement; it has to be noted here that the calculations indicate an energetically unfavorable dimer detachment. The atom detachment energy is determined by the local coordination environment of the detaching

atom, and consequently its value is essentially independent of cluster size, except for very small clusters where incomplete coordination lowers the detachment energy. Note however, that diffusion of adsorbed clusters also becomes energetically more favorable at small cluster sizes. Therefore, for circumstances involving small enough clusters and higher temperatures competing coarsening mechanisms (that is, the aforementioned OR and SR ripening modes) may operate, with one of them eventually dominating.

In cases where the SR mechanism dominates already at low temperatures, OR processes may enter only if the cluster diffusion barriers increase strongly with size (thus quenching the SR process). Under such circumstances, a critical cluster size may be reached during the SR process, at which detachment of single atoms is energetically favored over diffusional displacement of the entire cluster. When this occurs, the OR mechanism takes over, accompanied by an increased concentration of transporting species on the surface. This is the case for Pd clusters on g/Rh(111) and g/Ru(0001). Since Pd clusters adsorb with a higher binding energy on the g/Ru(0001) surface than on the g/Rh(111) one, the SR mechanism is partially suppressed on the former at lower temperature. This is confirmed by the observed PSD broadening after annealing to 600 K for g/Ru(0001) and to 700 K for g/Rh(111).

Cluster ripening processes can be strongly influenced by the presence of adsorbates. Indeed, cluster diffusion and coalescence (i.e. the SR mechanism) of small Pt clusters on a g/Ir(111) surface induced by CO adsorption has been reported recently.[36] The graphene film in this system is characterized by a rather weak interaction with the underlying Ir(111) surface and the Moiré superstructure forms through pinning by the adsorbed clusters. Unpinning of the clusters (caused by CO adsorption) induces diffusion and coalescence of clusters with less than 10 atoms, although the precise mechanism is not understood

yet. Since the g/Rh(111) and g/Ru(0001) are stable superstructures, characterized by much stronger interaction between the graphene layer and the metal surface (compared to that operating in the g/Ir(111) case), and since CO will have desorbed at annealing temperatures above 400 K,[37] the onset of such adsorbate-induced SR mechanism in the present systems is not expected. Adsorbates may as well influence atom detachment energies, thus favoring the OR mechanism. Such effects have been demonstrated by Di Vece et al. in an x-ray diffraction study on Pd nanocluster films in the presence of hydrogen (1 bar) at RT.[38] The sublimation energy of Pd decreases with increasing hydrogen concentration and is about 50% lower at a H/Pd ratio of 0.3.[39] However such an effect in the present study under UHV conditions is excluded.

In light of these findings, a strategy for the reduction of cluster ripening can be formulated. Graphene-Moiré is a most favorable support for suppression of the OR mechanism of cluster coarsening because of its laterally modulated wettability – that is, on the Moiré-patterned surface transition metal clusters bind at locations characterized by relatively higher adsorption energy (wettable zones of the surface), with the detachment and transport of atoms (serving as the mass-transporting agents) from the clusters inhibited, because these processes require transit into areas of the Moiré-pattern that are characterized by a significantly weaker adsorption interaction. Consequently, on graphene-Moiré surfaces, cluster stability towards ripening is largely determined by the cluster adsorption energies. Since these adsorption energies may be relatively small, the onset of cluster diffusion (that is the SR coarsening mechanism) may occur already at relatively low temperature (e.g. 400 K). In contrast, on the bare metal substrate, the cluster adsorption energies, as well as the adsorption energies of individual atoms, are high. This facilitates atom detachment and diffusion and decreases the thermal cluster stability, this time through the OR mechanism. An intermediate case is represented by the

h-BN/Rh(111) substrate, where the laterally modulated wettability of the Moiré superstructure is accompanied by a higher cluster adsorption energy. This combination results in increased cluster stability (up to temperatures of at least 500 K) on this surface.

One can conclude that the significant success of oxides as stabilizing agents for the support of catalytically active species is related to a similar principle of laterally modulated wettability: whereas defects act as randomly distributed binding sites (wettable zones), stoichiometric areas in between, where the binding to the surface vanishes, block the transport of Ostwald ripening diffusing species. This leads to suggest that periodic wettability control may be a fruitful concept for the rational design of novel catalysts with enhanced stability against sintering.

Chapter II:

Dynamic characterization of cluster diffusion and ripening

State of the art

As shown by the static characterization of cluster ripening in the first chapter, the coarsening of clusters is an interplay between different ripening mechanisms. The study presented in the first chapter is based on data that describes metal cluster ensembles before, in between and after ripening processes. More information about the dynamics is needed; to this purpose the time resolution during the measurement has to be dramatically increased. In that way the cluster's diffusion over the surface can be studied in detail. To elucidate the required time scale, the diffusion of clusters is discussed in more detail in the following.

Description of diffusion paths

Diffusion is defined to be the uncontrolled movement of a particle in a medium in the presence of a concentration gradient and the diffusion flux is given by Fick's law:

$$\boldsymbol{J = -D\frac{\partial c}{\partial x}} \qquad \textbf{(1)}$$

D being the diffusion coefficient.[40] In his 1905 thesis and other publications, Albert Einstein developed a formula connecting the mobility of a particle to this diffusion coefficient by combining the diffusion equation with the Boltzmann distribution for a system in thermal equilibrium.[41]

$$\boldsymbol{D = \frac{k_B T}{6\pi\eta r}} \qquad \textbf{(2)}$$

with k_B being the Boltzmann constant, T the absolute temperature, η the friction coefficient and r the radius of the particle.

Because of the contribution of Marian Smoluchowsky to this topic in 1906[42], the corresponding formula is known as Einstein-Smoluchowsky relation. Their work describes the so called Brownian motion of particles that was first observed by Jan Ingen-Housz but which attained general attention only with the work of Robert Brown on pollen in aqueous solutions.[43] The macroscopically random movement of the particles that Brown described is driven by innumerable collisions with the solvent molecules. As a consequence of Einstein's equation **(2)**[41] this random walk process is characterized for a 2D system by

$$\boldsymbol{\Delta r^2(\tau) = 4D^*\tau.} \qquad \textbf{(3)}$$

This tracer diffusion coefficient D* approaches the Fick diffusion coefficient D for highly dilute systems (non-interacting particles). This description of the diffusion process is based on two assumptions: there exists a mean free path and a mean time between two steps or two collisions. In this case the distribution of the step length and the time between two collisions would show an exponential decay.

Although this description holds for many systems like the Brownian motion of the pollen particles or the atomic diffusion on surfaces,[44] since the 1970s several examples have been identified that do not follow this ideal relation. Indeed, this has not always to be the case. Imagine that the trajectories depend on the "prehistory" of the particle, i.e. the sum of the previous steps. If the diffusion steps are no longer independent the particle's movement is driven by anomalous diffusion. The aforementioned distribution is then dominated by longer step lengths, respectively longer waiting times between steps, i.e. the exponential decay is skewed to the right.

In order to generate equation **(3)** for cases of anomalous diffusion, one can write:[45]

$$\Delta r^2(\tau) \propto \tau^{\alpha} \qquad (4)$$

If this exponent α is smaller than one, the mean-square displacement grows slower than the first power of time in the formula above. This scenario is then called sub-diffusion. This process was first discovered in photocopiers, where moving charges tend to get trapped by local imperfections in the amorphous material of the photocopier cylinder, so that their movement is slowed down.[46] Subdiffusion also occurs in physiological systems: The diffusion of molecules within the cytoplasm of cells or the diffusion of proteins across cell membranes, where the particles get trapped in compartments, is a typical example for this kind of diffusion.[47]

If the exponent in formula **(4)** is larger than one, the mean-square displacement grows faster than in normal diffusion. This case is then called super-diffusion, characterized by the fact that the distribution of step lengths and waiting times between steps is broadened. This kind of distribution is called Pareto-Lévy distribution and differs from a Gaussian distribution by the fact that it is a heavy-tail distribution, dominated by the largest steps or the highest waiting times between steps. It is named after the Italian economist Vilfredo Pareto and the French mathematician Paul Lévy. But these so-called Lévy-walks are not restricted to the world of mathematicians and statisticians; there are many examples of processes that fit into this category of anomalous diffusion. Lévy walk statistics are used e.g. to describe the travel behavior of humans and with that the dispersion of bank notes.[48] But also the dissemination of genetic material of certain animal species, the foraging behavior of spider monkeys and the flights of albatrosses can be described by Lévy walks.[48-49]

In surface science too, Lévy walk statistics can describe the diffusion of particles whose distribution is dominated by large step lengths and does not follow the classic Gaussian distribution of a random walker. Especially in the context of cluster diffusion it is important to know the fundamental mechanisms that lead to their ripening and the models that describe their diffusion pathways.

As an example for anomalous diffusion an extensive molecular simulation of a Au_{140} nanocrystal on graphite predicted that the diffusion of this nanocrystal would show a (here called) Lévy-flight type behavior.[50] The distribution for the flight lengths and the sticking time has a tail at the long flight-lengths side, respectively the long sticking-time side. They explain that the diffusion steps are not independent one from another, because once the cluster in movement by taking a non-sticking configuration, the probability to get into a sticking configuration again is very low, so the particle continues its movement and can cover an important distance. This searching for a coincidence position happens on a time scale of nanoseconds.

This example is similar to the investigations in the first chapter, because of the same carbon lattice support. Though, on a graphene superstructure the large periodicity, which result from the interaction of the carbon lattice with the underlying metal support, reduces the probability to hit wettable sites. However the binding of the cluster to the graphene substrate at the wettable sites is much larger than on graphite. Therefore the time scale of the diffusion is enlarged and figures in the range of miliseconds. In this case the tracer diffusion constants can well be measured by enhanced time-resolution local probe techniques, e.g. Atom Tracking. Some of these techniques will be presented in the following.

Enhanced time resolution Scanning Probe Microscopy techniques

Nevertheless standard STM keeps one main drawback caused by the scanning of the considered area. For one spot, information can only be gathered while the tip is scanning over it. The rest of the scanning time the considered spot remains unobserved, making it difficult to get more information out of it. This makes the improvement of time resolution an important issue in STM.

In literature one can find several techniques that try to tag this problem. The increase of time resolution can either be achieved by keeping the tip stable at one position and getting real-time information about this spot of the surface, or by increasing the scanning velocity, so that also fast processes can be imaged. Depending on the system and the application one or the other is favored. One of the techniques that fit into the first category is open-feedback-loop STM, where the vertical feedback is switched off. Hence the observation of particle mobility or a molecular switching process becomes accessible. The time resolution is increased because the tip stays fix at one position, either in the center of the investigated molecule or above an important electronic orbital that is involved in the switching. This technique is only applicable if the molecule is immobile or at least shows no translative movements under the experimental conditions. That is why open feedback STM experiments are often performed at liquid He temperature in a cryostat where lateral drift can be optimally excluded. Stipe et al. investigated the rotation of acetylene on Cu(100) by a tunneling current induced process with a pulse energy corresponding to the excitation of the C-H stretch mode.[51] The feedback of the vertical direction was kept open during the pulse. Out of the decay time constant of the excited state they could calculate the rate of rotation. Baber et al. even went further exploring thermodynamic properties of molecules on surfaces.[52] They adsorbed thioether differing by their chain length at low temperatures on Au(111) and observed that beyond a specific

temperature the thioethers start to rotate due to thermic activation. By following the rotation of the chains by open feedback STM, they could deduce the switching rate of the process and from that the activation energy for rotation by plotting the data from different temperatures in an Arrhenius plot. In another interesting study, Auwärter et al. used the electron current through the STM tip to switch the hydrogen atoms in the inner cavity of a tetraphenyl-porphyrin molecule and realized with that an atomistic, four-level conductance switch.[53]

The increase of the scanning velocity in STM has been a topic for several years now and impressive progress has been made by different groups. In order to drive the tip at enhanced velocities, the mechanical setup has to be changed so that the high resonance frequencies can be challenged.[54] In another approach suitable resonance frequency windows are chosen, so that a conventional STM can be driven at enhanced velocities just by adding additional electronics.[55] Although the measurement times are very low for this method and the resulting movie is appealing to the eye, the high tunneling current (around 1 nA) that is required for this method makes it impossible to scan clusters, as they are interacting too much with the tip and in the worst case will be sucked off the surface by the tip. The high currents are necessary since driving the preamplifier at higher band-width requires a lower gain. Nevertheless for other applications this technique can provide impressive real-time movies of surface processes, e.g. the diffusion of oxygen atom on Ru(0001) at RT observed with a high-speed STM.[56]

One of the most efficient techniques to increase the time resolution in STM, while measuring at low currents, is Atom Tracking that has first been suggested and described theoretically in 1987.[57] In this paper the major ideas and possible applications of this technique were already formulated and a very simple experiment showed that the

technique works. The most important idea was that a scanning tip can be controlled to always run uphill and thus follow a moving maximum on the surface. This is realized using the lateral feedback of a tip that performs a dithering movement over the protrusion. Thus, the imaging is given up and simply a local extremum is followed. This works only if lateral interaction can be neglected. A scheme of the Atom Tracking working principle is displayed in Fig 10.

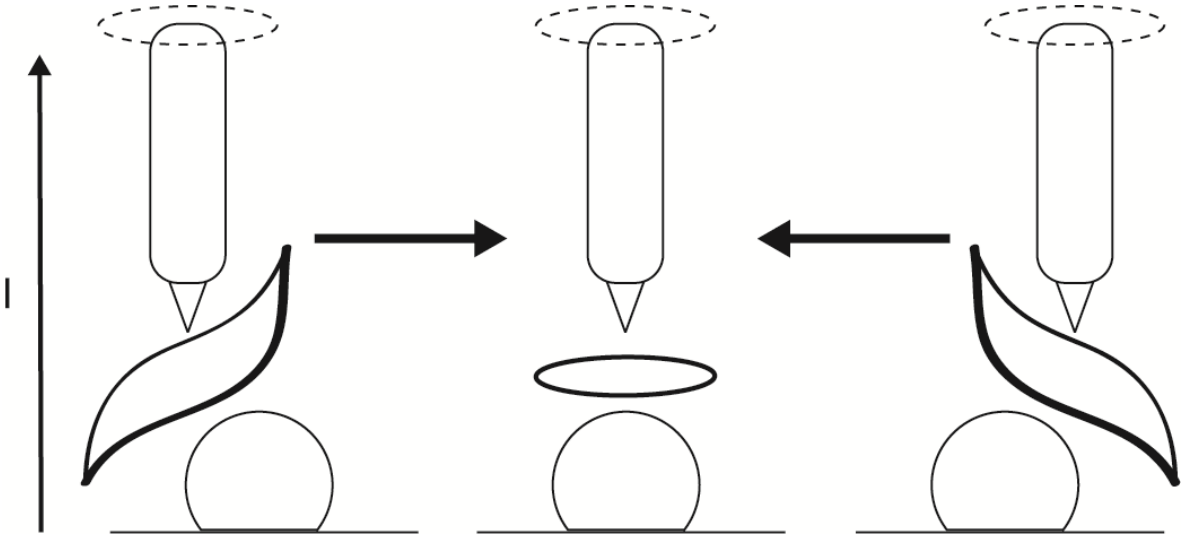

Figure 10. Scheme of the Atom Tracking (AT) working principle. As soon as the rotating tip gets decentered from the protrusion, by drift or by a movement of the protrusion itself, the lateral feedback drives the tip again on the maximum and tracks its way. The bold lines represent the evolution of the tunneling current during the circular movement (represented by a dotted line above the tip). The tunneling current shows an exponential dependance on z. Therefore, strong effects can be detected even at low current setpoints.

Some years later Swartzentruber et al. showed that this technique can be used to track silicon dimers on Si(001).[58] They visualized their dynamics and calculated thermodynamic properties. From the tracking pattern and the movement of the dimers in time at different temperatures, they deduced hopping rates, which were plotted in an Arrhenius diagram to result in the activation energy for the diffusion step. They further showed that the observation of the z-channel can provide simultaneous information about the height of

the silicon particle during the tracking. They observed that the dimers can be found in two different conformation states, which differ in height. Thus, the z-channel can be an indication of the adsorption state a particle. In another study they checked the effect of higher tip bias on the activation energy for diffusion and rotation.[59]

After nearly a decade without a publication on this topic, Abe et al. used Atom Tracking in combination with Atomic Force Microscopy (AFM).[60] In contrast to the application of Swartzentruber, which was to observe diffusion of mobile species, this group now tracked a stable feature in order to calculate the thermo-mechanical drift of the substrate. The apparent movement of the feature can then be referred exclusively to drift. The aim of this drift control was to get a very stable positioning for reproducible force spectroscopy experiments with non-contact AFM at room temperature. A considerable noise reduction in the spectra combined with an increase in resolution could be achieved. In collaboration with Rahe et al. they further developed the technique to be compatible with any kind of SPM system and used it for precise 3D non-contact AFM force mapping.[61] An automated scan protocol enables them to switch between drift measurement and force mapping. The drift compensation is measured at regular intervals over the same immobile feature, while the force mapping takes place in between and is referenced to this spot. This application of Atom Tracking does not take so much advantage of the increased time resolution, but is powerful through its ability to locate defined places even in severe drift conditions.

The Atom Tracking technique thus shows to be a powerful tool for the investigation of diffusing species like clusters on superstructured surfaces and for shedding light on the diffusion mechanisms and the thermodynamic properties of the clusters on surfaces. Hence, it is the perfect technique to combine with our cluster source system, which

provides low coverage size-selected clusters on well-defined long-ranged superstructured surfaces.

Experimental approach: Implementation of Atom Tracking

This section will describe the implementation of the AT technique, the finding of the right parameters for driving the technique with noble metal clusters, as well as a description of the procedure for data treatment applied on the first tries with this technique.

The implementation of AT in our VT-SPM system was led by the idea of a modular concept, which means that the different components of hardware and software should be easy to get and no greater modifications should be necessary, so that the AT module can be implemented into a large number of SPM systems. It was realized as an add-on instrument connected to the control system that regulates the z-feedback.

In order to keep the system simple and very user-friendly, we relied on the fast data acquisition system acquired for FAST STM measurements (PXI 1033 box from National Instruments) and implemented a digital PID regulator that could be switched on in a highly controllable manner: via a link between the LabVIEW program and the SPM system the necessary signals to drive the experiment and receive a trigger timing signal from the STM computer could be exchanged. Fig 11 shows a scheme of the implemented Atom Tracking module. The LabVIEW program controls the experiment through a field-programmable gate array (FPGA) that has a fast data acquisition synchronized with the dithering signal generation. These signals are then given out by the box and added to the different piezo voltages respectively that drive the STM tip. The trigger for the AT experiment is given by the STM controller, as well as the signals of topography (Z-channel) and tunneling current (I_{mon}). As the experimental frame is very complex, the LabVIEW program was written by the software engineer Giulia Troiano.

The implementation of the AT measurement requires various hierarchical steps that are described in the following.

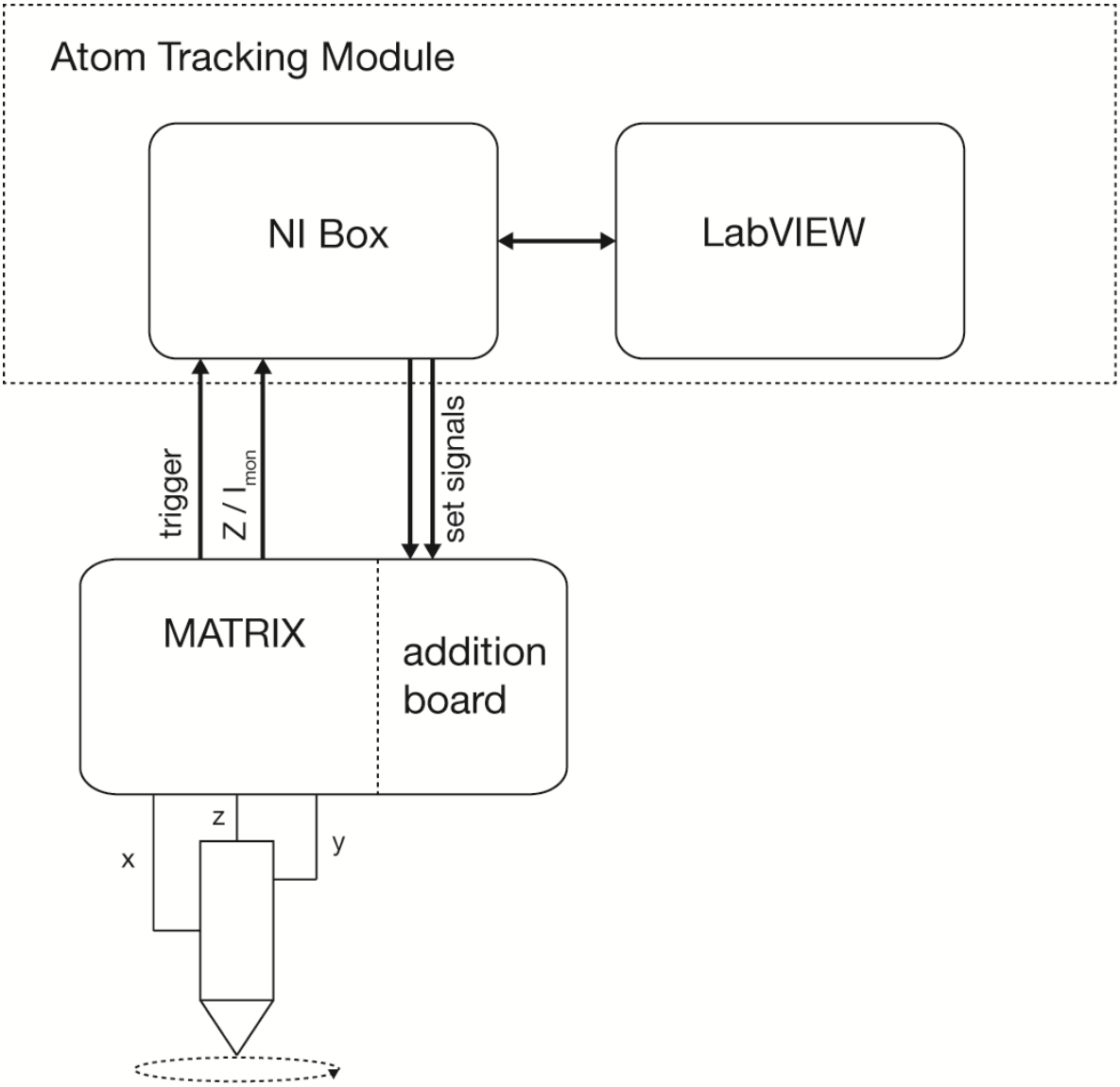

Figure 11. Scheme of the Atom Tracking module and its combination to the MATRIX control unit of the STM. The arrows mark the flow of information from one unit to the other.

Explanation of the set-up

Circular movement

The tracking of a feature on the surface only works if the tip performs a circular movement of the right diameter and symmetry over the considered feature. In order to get the STM tip rotating, two sinusoidal voltages, approximately phase-shifted by 90°, are defined by the LabVIEW program. These voltages are added to the x- and y-signals of the Matrix STM controller through an addition board, custom-made by our electronic workshop (see Fig. 12).

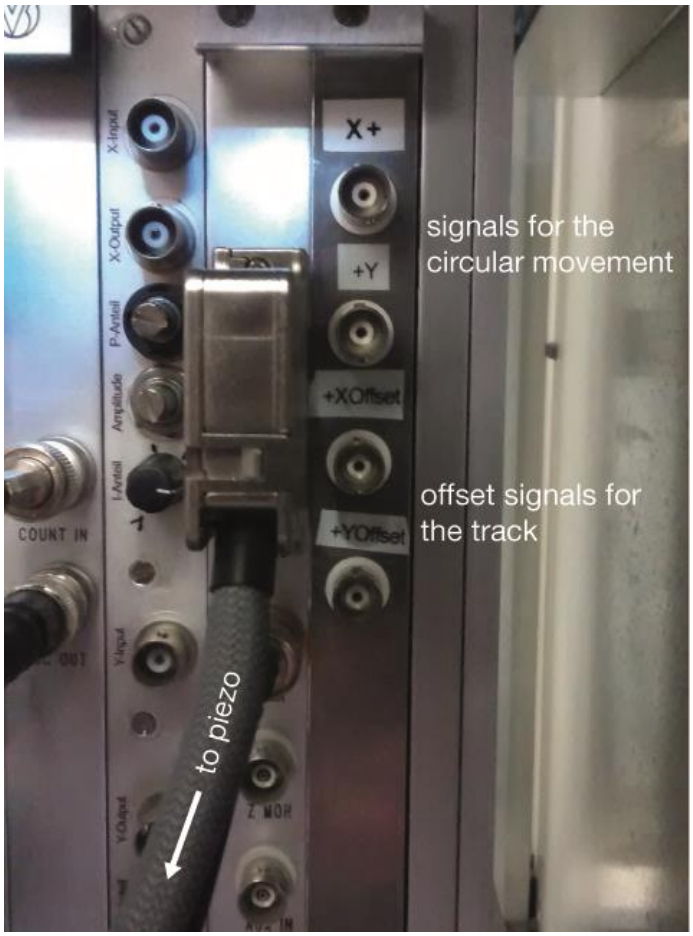

Figure 12. Addition board (right slide), which takes up the circular movement signals as well as the offset signals (which will be described later) coming from the LabVIEW program and adds them to the position signals coming from the control system. The resulting voltages are applied to the piezo trough the cable pointing downwards.

Software selectable parameters of this dithering movement are the voltages that are added to the piezos (which define the amplitude of the circular movement), the dithering phase shift between the two sinusoidal voltages and the frequency of the rotation. The typical values for these parameters are described later.

Detection of the error signal

The heart of the AT technique is the regulation of the tip above the feature. This regulation is based on the error signal that can be extracted using a digital lock-in amplifier. In the implemented version, the lock-in amplifier is entirely programmed using a custom-made virtual instrument in LabVIEW. The tunneling current signal is multiplied with a sine and a cosine wave at selectable (lock-in) phase shift and then low-pass filtered. This leads to an in-phase and a quadrature signal that can be identified (after appropriate setting of the lock-in phase) as the x- and y-error signals. This can be understood, if one imagines the variable tunneling currents that the tip is exposed to at the rotation plane over the decentered cluster (see Fig. 13).

The z-feedback is too slow to follow these variations in the tunneling current, since the preamplifier is set to high gain and low band-width that cuts off at 800 Hz, i.e. around the dithering frequency. This is only the case if the loop gain settings remain similar as in usual STM imaging.

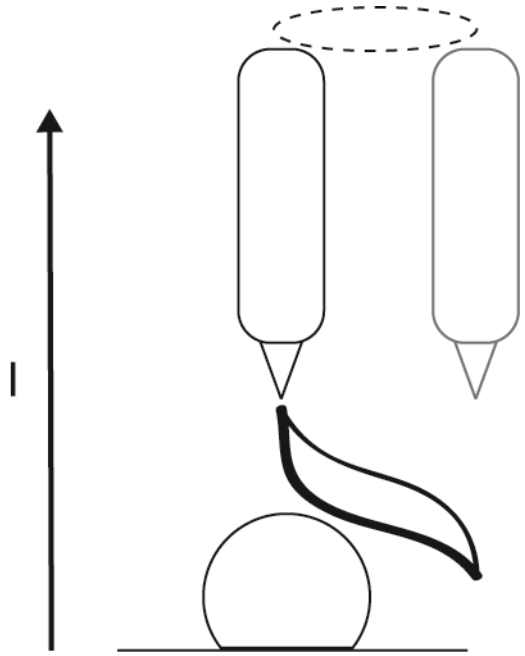

Figure 13. Representation of the tunneling current depending on the position of the tip over the decentered cluster. This variation in the tunneling current will generate an error signal that will help to drive the tip rotating again over the center of the cluster.

Regulation and generation of a tracking offset

In order to track a surface feature, an offset has to be generated using the error signal that has been extracted in the step before. This is realized by a simple PI controller that is integrated in the LabVIEW program. The control loop is set to minimize the error signal und thus to drive the tip to the topographic maximum of the feature. The control value is calculated by the following formula using a proportional and an integrative term:

$$u[i] = K_p\left(e[i] + \frac{T_s}{T_i}\sum^{i} e[i]\right)$$

, with K_p being the proportional constant, T_i the integration time and T_s the sampling period. The regulated offset values for the X- and the Y-channel are calculated separately and are added to the piezo driver in the control system as a second pair of inputs. With a

dithering frequency of ≥800 Hz, we decided to set the minimum sampling period to 1 ms, whereas a measuring point is taken each 10 ms in order to prevent excessive data generation. Typical values for the regulation constants were K_p=0.05 and T_i=10 ms, in line with the measurement time steps.

Control of the set-up steps

Check of the circular movement

The amplitude and frequency of the rotation is subject to the design of the experiment (Fig 14). A larger amplitude leads to a larger dithering circle and thus to a larger capture area but also to uncertainty in space. The center of a large circular movement will lack of a gradient leading to a doughnut shape imaging (see later). Smaller amplitudes and thus a smaller dithering circle tend to show problems when following long jumps of surface features. The area of control is smaller and thus the gradient of control decreases.

Generally the amplitude of the circular movement should be in the range of the radius of the feature or slightly smaller, which was in the case of clusters 50 mV peak-to-peak (for an apparent particle diameter of 1.5 nm). The voltage is divided by a factor of 1.5 before being applied on the piezo by two symmetrically driven quadrants. As the piezo has a conversion factor of 32 nm/V, the cluster should appear with a diameter of around 1 nm, but is slightly enlarged due to the tip convolution effect. The dithering frequency was chosen to be 800 Hz (in our case given by the preamplifier bandwidth of 800 Hz). Ideally it should be larger than the cut-off frequency of the vertical feedback, but definitely smaller than the first resonance frequency of the piezo crystals. Excitations in these zones should be avoided in order to prevent strong distortions in the circular movement due to the resonances.

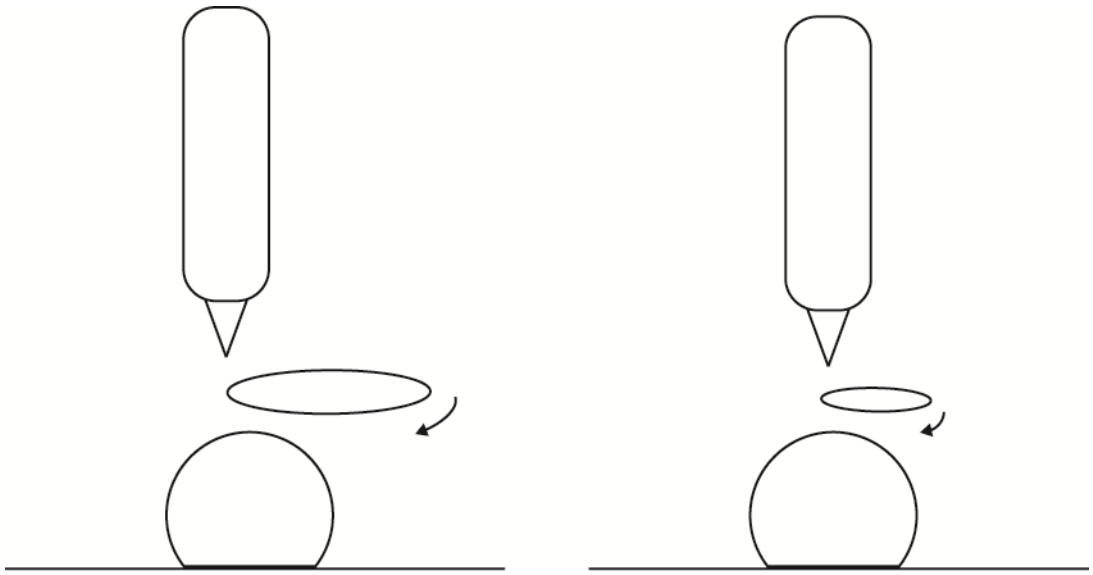

Figure 14. Scheme of the rotating tip above an adsorbed cluster with a larger (left side) and a smaller (right side) amplitude of the sinusoidal voltage addition. The radius of the resulting revolving of the tip is hence larger or smaller.

In order to check the dithering properties, a scan of the feature can be made while the tip is dithering. Due to the superposition of a circular (dithering) and a linear movement (scanning), the image of the feature should be a perfect circle, according to the theory of Lissajous figures,[62] when the phase difference is exactly 90°. Due to the lateral extension of the cluster the shape resembles more a doughnut. With decreased dithering amplitude the hole in the middle is disappearing at some point. If the dithering frequency and especially the effective dithering phase are not correct, the shape of the feature is elongated, as it is shown in Fig. 15. The dithering phase has then to be corrected; this happens close to resonance frequencies that influence the x and y movement differently ($C_{\infty v}$ symmetry of the piezo tube versus C_v symmetry of the coarse sled).

Rotation frequencies that are not suitable for our measurements can be identified, because they do not show a perfect circle at 90° phase shift. These frequencies lie in the neighborhood of resonances which can be easily excited and provoke phase shifts.

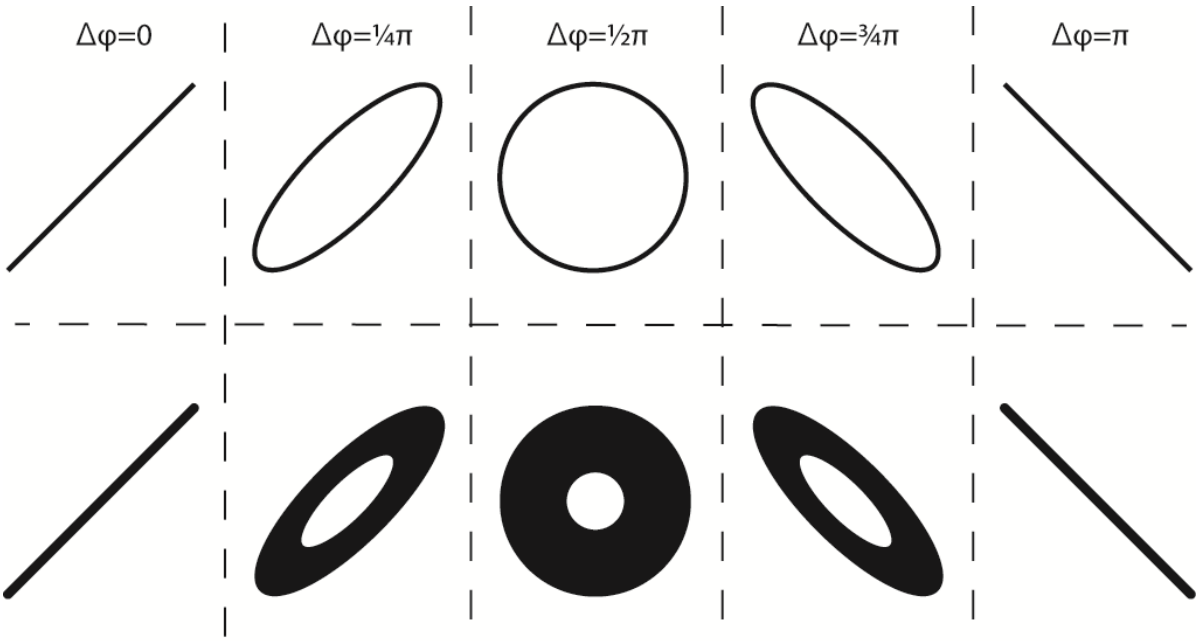

Figure 15. Upper part: theoretical Lissajous figures with an amplitude ratio 1:1 depending on the phase difference.[62] A perfect circle is obtained when the phase difference between the two signals is exactly π/2. Lower part: Due to the convolution of the tip and the surface feature the Lissajous figures are broadened and show an "doughnut" shape for the perfect match of the phases.

As it can be seen in Fig. 16, several STM scans that were taken at 1056 Hz rotation frequency, the geometries are phase shifted compared to theory. Thus, the excitation of resonances leads to distortions that can be corrected for by proper setting of the dithering phase and eventually by adapting the excitation amplitude in order to account for different Q factors.

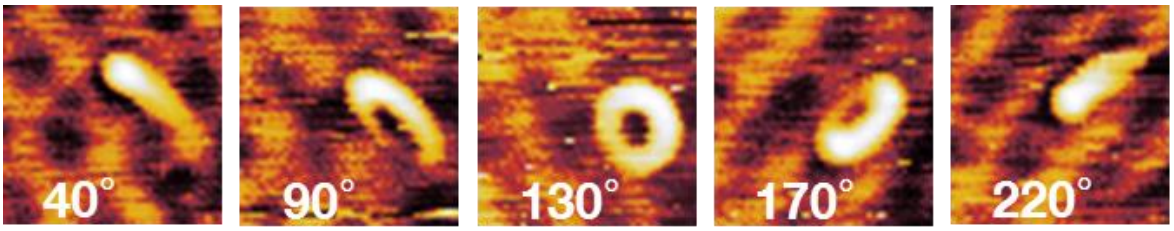

Figure 16. Experimental Lissajous figures that were taken at 1056 Hz with 75 mVpp amplitude. Note the phase shift of 40° compared to theory. Scan conditions: 1.3 V, 100 pA, 1%loop gain. Image size 10 nm x 10 nm.

Check of the error signal

In a next step, the error signals have to be assigned correctly to the directions on the surface. To this purpose, the LabVIEW program comprises a tool to image the error topography. Fine-adjustments for the circular movement of the tip can be made here, as well as corrections for the sign assignment and the phase between error signals. This is a very important tool, as it became obvious after some experiments that the shape of the error signal was depending on the tip shape. So a bad tip (asymmetric tip or multiple tip) could be recognized a lot faster with the error topography tool. As each new tip is slightly different, the error phase had to be adjusted accordingly.

There are mainly three indications for a bad assignment of the error signals: the representation of the error signal on the cluster can have no clear line of symmetry or the attribution in the error signals for x and y channel are not shifted by 90° or the attribution in the error signals for x and y channel are not coinciding with the x and y direction, respectively. The reason for that could be that the tip has an asymmetric apex (different properties in x and y direction) or tips with different bluntness react differently on the lateral feedback. Therefore the error topography tool enables to correct the tip influence by fine-tuning the error phase. Usually the range of fine-tuning was around 40°. A correct error assignment is shown in Fig. 17 below.

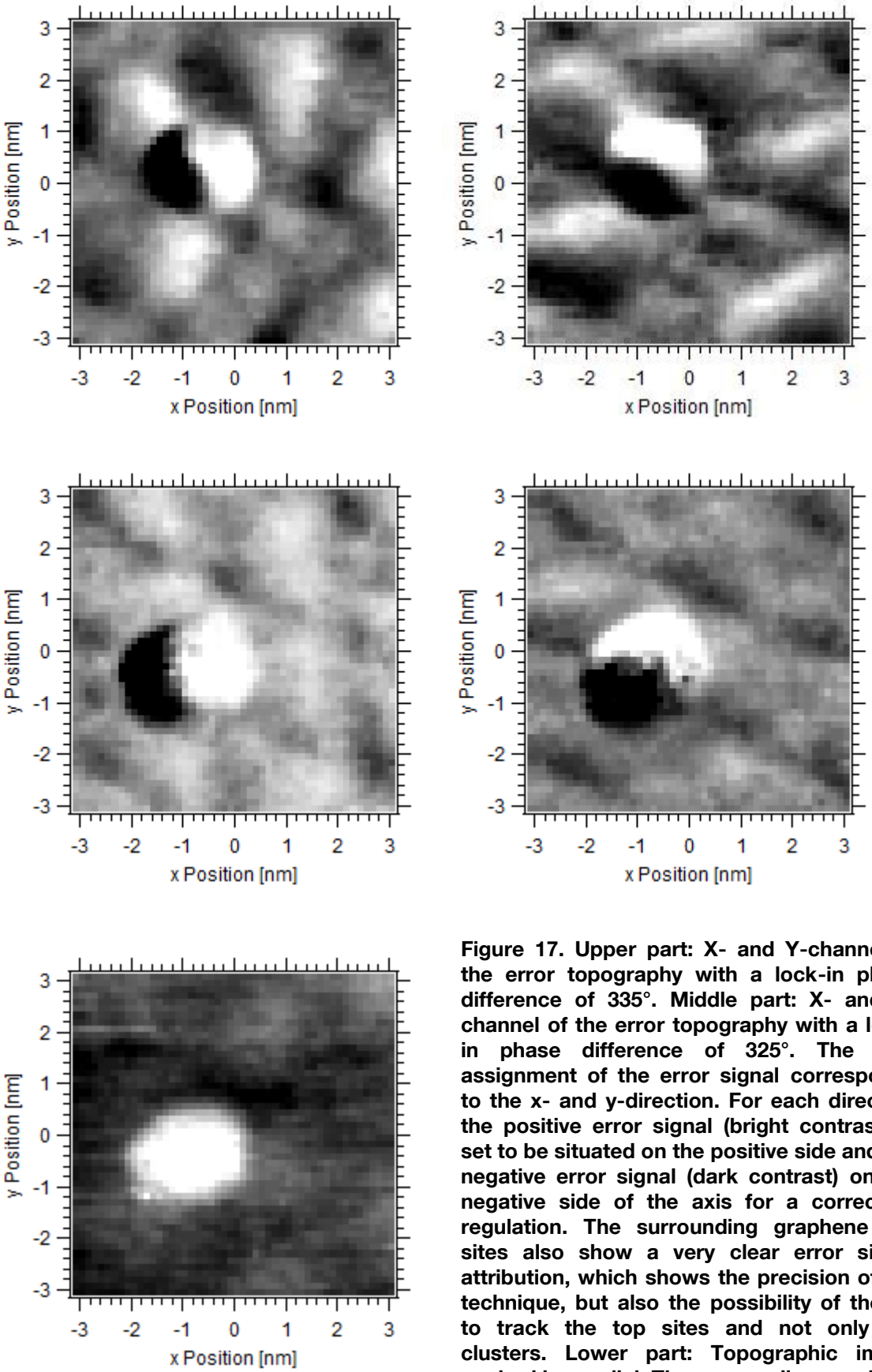

Figure 17. Upper part: X- and Y-channel of the error topography with a lock-in phase difference of 335°. Middle part: X- and Y-channel of the error topography with a lock-in phase difference of 325°. The sign assignment of the error signal corresponds to the x- and y-direction. For each direction the positive error signal (bright contrast) is set to be situated on the positive side and the negative error signal (dark contrast) on the negative side of the axis for a correct PI regulation. The surrounding graphene top sites also show a very clear error signal attribution, which shows the precision of the technique, but also the possibility of the tip to track the top sites and not only the clusters. Lower part: Topographic image aquired in parallel. The surrounding graphene

can be hardly seen and the borders of the cluster are not as clearly defined as in the error topographic images, showing the high imaging dynamics of the error topography evaluation.

The AT technique is in principle also able to track depressions, just by changing the sign of the error signals, i.e. by adding 180° to the lock-in phase. In this case the tip always runs downhill and searches for a minimum, but this has not been checked in this work.

Timing of the experiment

While making an AT experiment, the communication of the MATRIX system and the LabVIEW program is achieved with a MATE script (Matrix Automated Task Environment). This MATE script has to be loaded separately when starting an experiment. It opens a channel for a TTL pulse (Transistor-Transistor Logic), which switches from high to low exactly when choosing a feature by mouse control in the STM image on the MATRIX monitor with the tip positioning tool. Upon this TTL pulse, the MATRIX control system stops the lateral scan movement, but continues to regulate the z-feedback, keeping the feedback loop-gain at the usual value. At this point, the LabVIEW program starts the control loop and gives out the correction offsets to hold the tip over the feature's maximum. These voltage offsets, added to the piezo crystals of the STM scanner, are held even after finishing the AT measurement. In this way the environment of the cluster after the tracking can be investigated with a "slow" STM image:

For an ideal experiment, the surface should be scanned conventionally before and after the tracking, so that one can define the local position of the feature at the start and at the end. After a first scan documenting the position, the tip should scan a close-up before one selects a feature of interest using the positioning tool. This helps to avoid piezo creep

that could mislead the tip. The tracking activation can lead to an apparent hop when the tip is still searching for this maximum. As this hop was within the range of the cluster's dimensions for a successful tracking and this artifact was similar each time, it is believed that it is due to positioning uncertainty when clicking on the cluster with the mouse tool while scanning over it. If this initial movement is beyond the range of the feature's dimensions, the tip has lost the feature. A checking of the correct error signal assignment can improve the situation.

During the tracking experiment, the trace is monitored on the screen and the according data is saved as a HDF5 (hierarchical data format) file. Fig. 18 shows a screenshot of the program's front panel. In the upper left corner the parameters for the circular movement can be set and the movement can be switched on and off using the respective buttons. On its right side, the parameters for the lock-in amplifier, like time constant and phase, can be set. At the lower left side the parameters for the PI regulation can be set and also changed during the experiment. In the middle of the panel a large tracking graph documents the position of the tip on the surface, while the evolution of the x- and y-direction, as well as the z- and I-channel can be followed in the smaller graphs on the upper right side. In the lower left side the settings for the visualization of these graphs can be found.

The program has been written so that a restart of the scanning in MATRIX switches the TTL channel from high back to low and deactivates the tracking. The offset of the stopping position is maintained, so that one can document the new position of the feature by a conventional scan. If it is necessary, another tracking of the same feature can follow immediately.

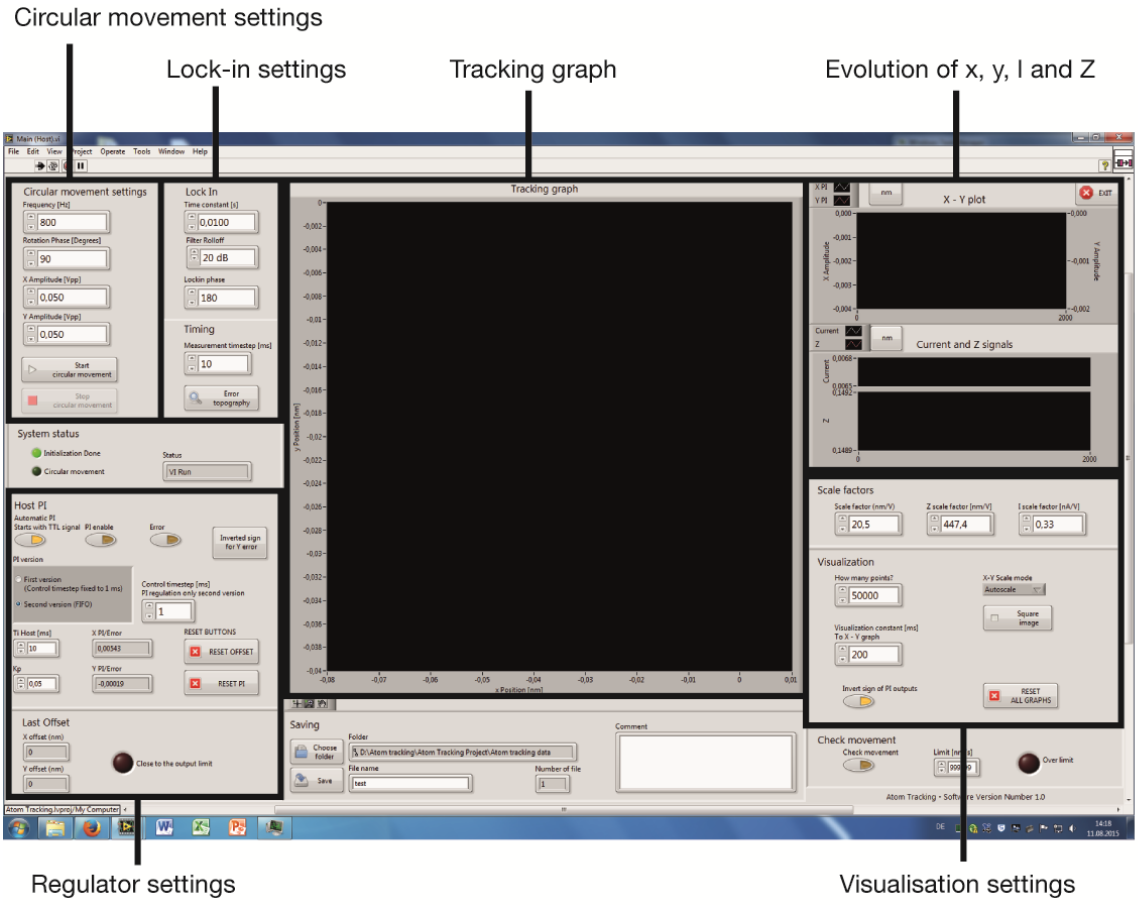

Figure 18. Screenshot of the main program's front panel. Here all the parameters necessary for the tracking can be adjusted and the track of the followed feature observed in real-time on the large tracking graph. The smaller graphs show the evolution of the x- and y-offset-channels as well as the Z-topography and the current channels.

Drift background correction

A dedicated IGOR program has been developed that allows to analyze the full tracking information: tracking graph, drift corrections and statistic evaluations. Fig. 19 shows a raw tracking graph where displacements were deliberately applied by moving the tip by ±1 nm steps in x and y direction by the MATRIX program, i.e. by inducing jumps that the lateral feedback had to compensate.

The most important feature of this program is the drift background correction. Drift is an important issue in STM, both when taking topographs of the surface and for spectroscopic experiments, but also for AT: If the tip drifts by piezo creeping due to a thermal gradient, the system not only records the movement of the tracked feature but overlays the drift of the tip with respect to the surface. Hence the drift has to be calculated out to extract the pure movement of the tip. In Fig. 19 the tip is drifting from the upper right to the lower left of the graph. In between the jumps, the drift is recognizable by the diagonal slope.

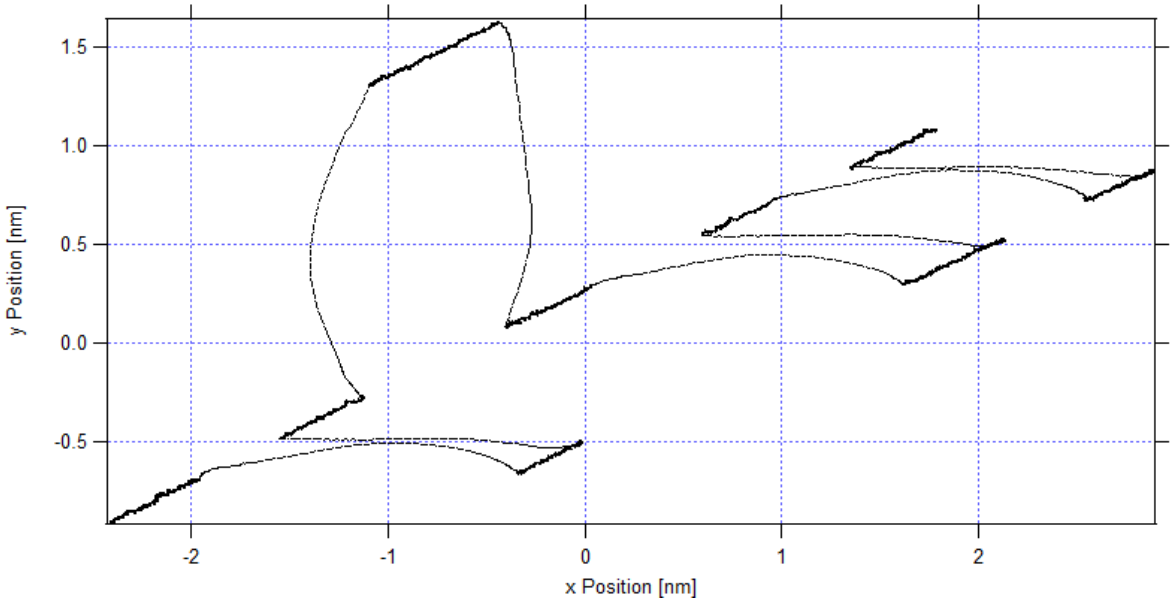

Figure 19. Tracking graph of the first measurement regarding the offset calibration. Using the positioning tool of the STM control unit, deliberate offset jumps of 1 nm in all main directions are applied during the tracking. In between the jumps the remaining thermal drift can be seen.

The algorithm of the drift background correction calculates smooth background movements out of the difference between adjacent data points in x, y and z. It allows for the setting of several parameters regulating for example the time step and the box size of the analysis upon which the correction curve is calculated which is then subtracted from

the measured track. Thus the program corrects for smooth changes between adjacent data points (in x- and y-direction respectively), while ignoring any discontinuities. In this way slow variations in the trace can be discerned from fast variations and thus from movements that can be assigned to the cluster itself. After the drift correction the tracking pattern only shows the pure movement of the tip and is shown in Fig. 20.

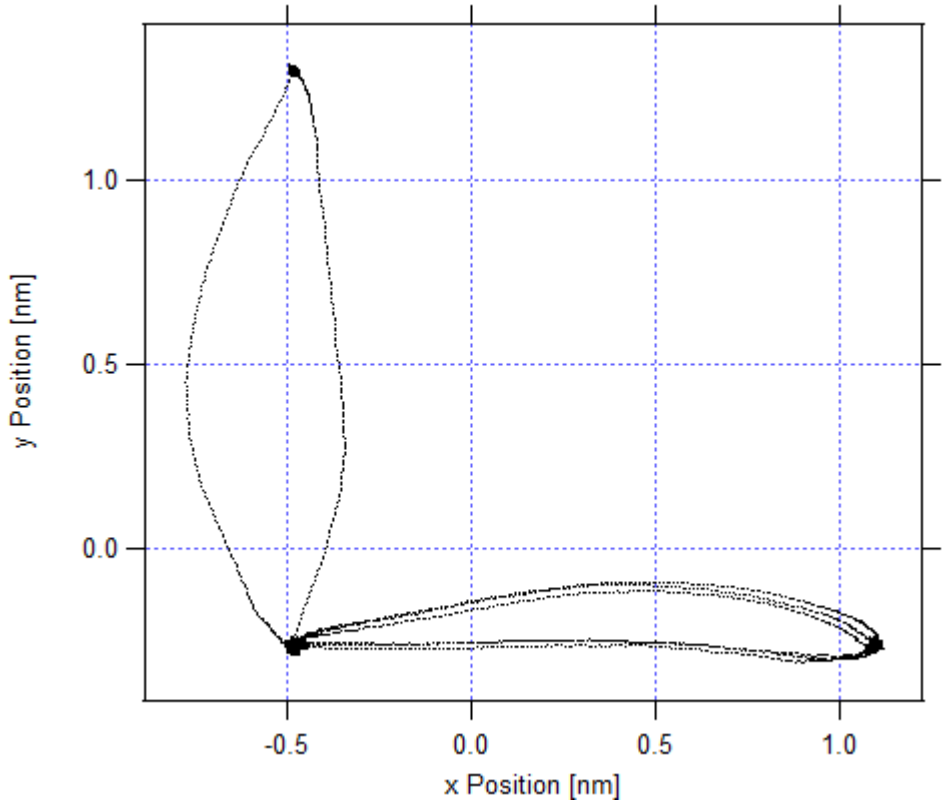

Figure 20. Tracking graph of the offset jump experiment as in Fig. 19, but with drift background correction applied. It becomes obvious that the applied 1 nm jumps do not correspond to 1 nm reactions and that therefore a calibration is needed.

Calibration

As the correction offsets that are added on the piezo for the X- and Y-directions are voltages, they have to be calibrated in order to move the tip to the precise location and not too far. Therefore an offset of exactly 1 nm was deliberately added to the tip in each

direction during the tracking and the response of the regulation was checked. In Fig. 21 the tracking graph for such an experiment on a random cluster is shown. For an offset of +1 nm in X, the tracking added a voltage on the X-piezo that corresponds exactly to an apparent movement of the tip of -1 nm. As the cluster did not move and the tip tries to stay permanently on the cluster, the regulation reacts upon the offset addition by driving the tip in the opposite direction on the cluster again. This trace should be exactly 1 nm again.

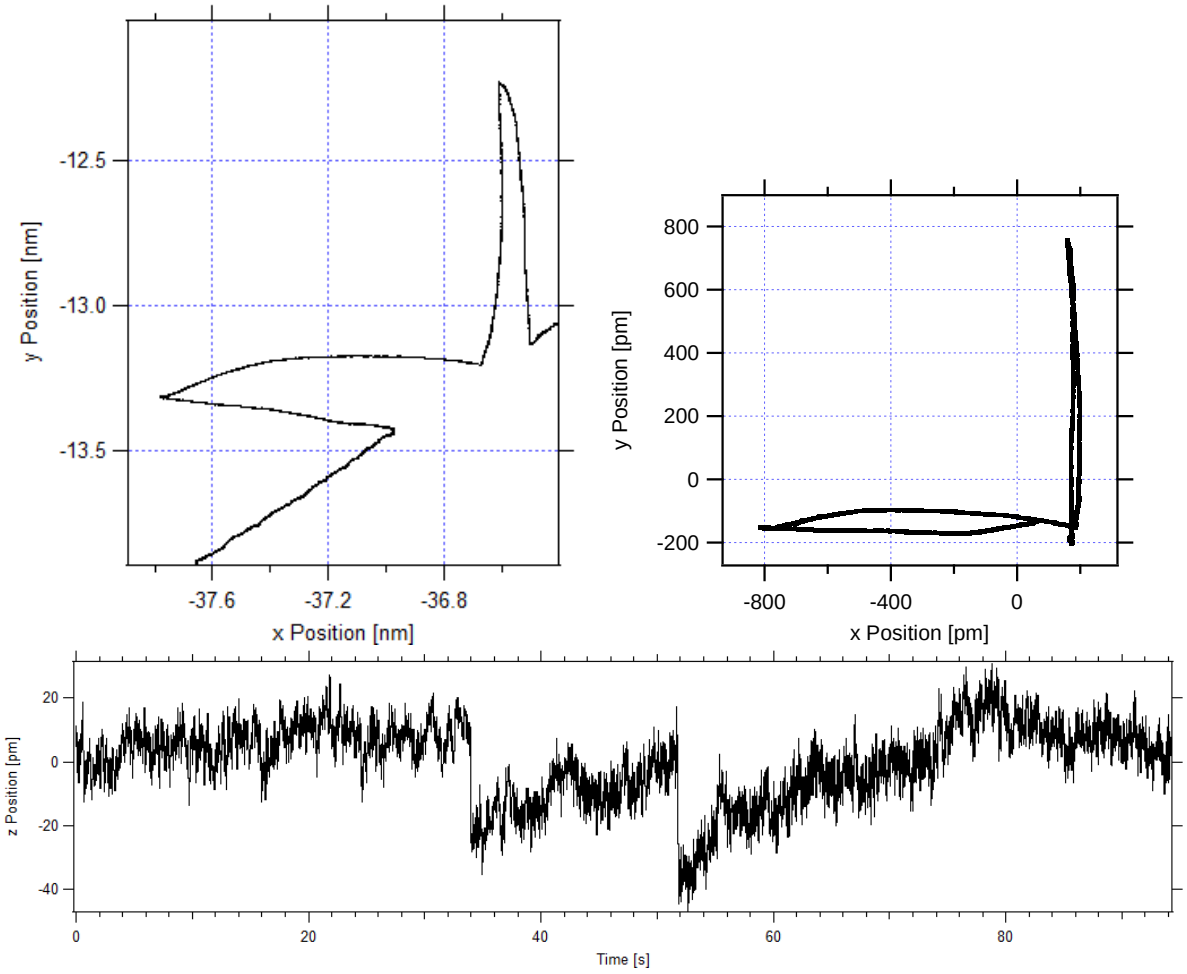

Figure 21. Tracking graphs of 1 nm jump experiments before (upper left) and after (upper right) drift correction. The new calibration factors for the X- and Y-offset channels result in the display of 1 nm jumps in the tracking graphs. Lower part: Evolution of the z-channel. The two jumps are well documented, as the forced jumps of the tip are rather harsh.

The same was checked in the Y-direction until the correct calibration factor was determined by fine-tuning. It was found to be 20.5 nm/V. This value is specific for our system and specific for the kind of addition board (with different voltage multiplication and division steps), which is used to add the voltages of the tracking to the set voltages of the STM. Regarding the aforementioned conversion factor of 32 nm/V for the piezos in the STM and a division factor of 1.5, the overall conversion factor should be 21.333 nm/V. The discrepancy of the theoretical and the measured conversion factor is probably due to a smaller dynamic range of the piezos. Thus it will be necessary to calibrate the offset output of the tracking each time the addition board is changed or exchanged.

For the calibration of the Z-channel signal (transferred by the Z_{mon} output), two different tip positions (in tunneling contact and fully retracted) were compared. The applied voltages were determined using an oscilloscope and the topographic values in nm were displayed by the STM control system. A calibration factor of 447 nm/V was found. This corresponds to a z-piezo with a dynamic range of ±1000 nm at a voltage application of ±140 V and subsequent division of the z-output by total factor of 62.5. The conversion factor for the tunneling current was set in the same way considering that 10 V correspond to 3.3 nA.

Quality of the tracking

Fig. 21 shows the track of the tip before and after the drift correction. From the first graph it becomes obvious that there is a drift driving the tip from the upper right to the lower left side of the cutout, whereas the second graph is drift-corrected. Furthermore the noise level on the drift track is in the range of a fraction of an Ångstrom, which shows the extraordinary precision with which the position of the tip can be monitored with the AT technique.

Nevertheless, the track of the tip jump in Fig. 20 shows a considerable difference in the track of the forward jump and the backward jump, as well in x- as in y-direction. This difference is much smaller in Fig. 21, even though the jump is slightly shorter here. As the tracking parameter are exactly the same for both measurements the difference in quality can be referred exclusively to a different tip quality. The deviation from a straight line in Fig. 20 can be explained by an asymmetric tip apex, precisely because the deviation is even bigger in y-direction than in x-direction. Hence it is of utmost importance to have a precise mapping of the tip quality before beginning with a tracking measurement, which can be reached by using the error topography tool. So the correct setting of the lock-in phase is crucial.

Results and discussion

In this section the first results by using the implemented AT technique are shown. As described in the previous sections, this technique is able to track protrusions (and depressions) on surfaces, whether they are mobile or used for drift calculation. Together with the implementation of the AT technique, the right conditions have been determined that are necessary to track size-selected metal clusters of the size of some ten atoms on periodically wettable surfaces. In the first part it was shown that clusters on such surfaces tend to agglomerate and are altered by Ostwald ripening, but only little is known about how they move on the surface and how this mobility looks like in real time. Hence AT is the optimal tool to investigate this system. By tracking the cluster under the STM tip, each of its movements can be recorded with unprecedented resolution in time and in space.

For the first application graphene Moiré was chosen because of its periodical wettability on a large scale and its local scale characteristics: Mobility from one Moiré cell to another should be observable as well as intra-cell mobility. The choice of the size of the clusters to be investigated was more difficult to make. On the one side Pd_{19} showed to be an ideal candidate for ripening measurements because of its geometry that allows for rapid discrimination of ripening (2-layer vs 3-layer clusters) and to complete the static investigation from chapter 1; on the other hand the mobility of Pd_{19} at RT is rather limited so that AT measurements should cover a large period of time to be able to record a diffusion event. Although the STM is variable in temperature and AT measurements could be taken at elevated temperatures, the substrate seemed to show not only cluster mobility but also that of smaller particles (gases, atomic species) that diffused over the surface and distracted the tip from the feature under investigation, so that it lost control.

Furthermore, measuring at elevated temperature demands more time, due to the thermic drift that occurs each time the heating parameters are changed.

Thus a smaller particle that showed more mobility already at RT was chosen, namely Pd_{12}. Pd_{12} has already been investigated on graphene on Ru(0001) before and the calculated structures show that it has two isomers, one 1-layer high with twelve atoms in contact with the surface and one 2-layer high isomer with only seven atoms in the lower layer and five in the upper layer.[24b] It was shown experimentally that the higher isomers show a larger mobility than the lower isomer, which could be traced back to the smaller footprint of the former (see Fig. 41). A larger footprint leads to a stronger binding and hence to a reduced mobility. In terms of comparability of these two supports, a similar behavior is expected on Rh(111).

In the following experiments we have studied these 2-layer Pd_{12} clusters on graphene Moirés grown on Rh(111) in order to understand the conditions and parameters that are necessary to track them in a reliable and undisturbed manner. As outlined in chapter 1, on Rh(111) the clusters encounter less interaction at the wetting sites than on Ru(0001). Therefore Rh(111) turns out to provide ideal conditions to check the tracking of clusters at RT.

This chapter will be organized as follows: In a first step, experiments investigating the influence of gas adsorption mediated diffusion are described. Additionally the influence of the bias and the electric fields that build up in the tunneling gap is checked. In the following, several cluster track experiments are presented.

Influence of gas adsorption induced diffusion

One factor that could have an influence on the clusters dynamics is the activation due to gas adsorption, which was e.g. investigated experimentally by Gerber et al.[36] Even if we could not observe an effect of CO on the stability in the static investigation of chapter 1, it could be interesting which effect a larger amount of CO in the backpressure of the STM could have on the clusters and to study the effects on a smaller scale.

In the present study, CO was dosed on the Pd_{12} clusters to see if it could enhance their mobility, even without a lifting of the Moiré superstructure as observed by Gerber et al. During the tracking, a CO backpressure was stepwise raised over half an hour. In Fig. 22 the tracking graph of a first try can be seen.

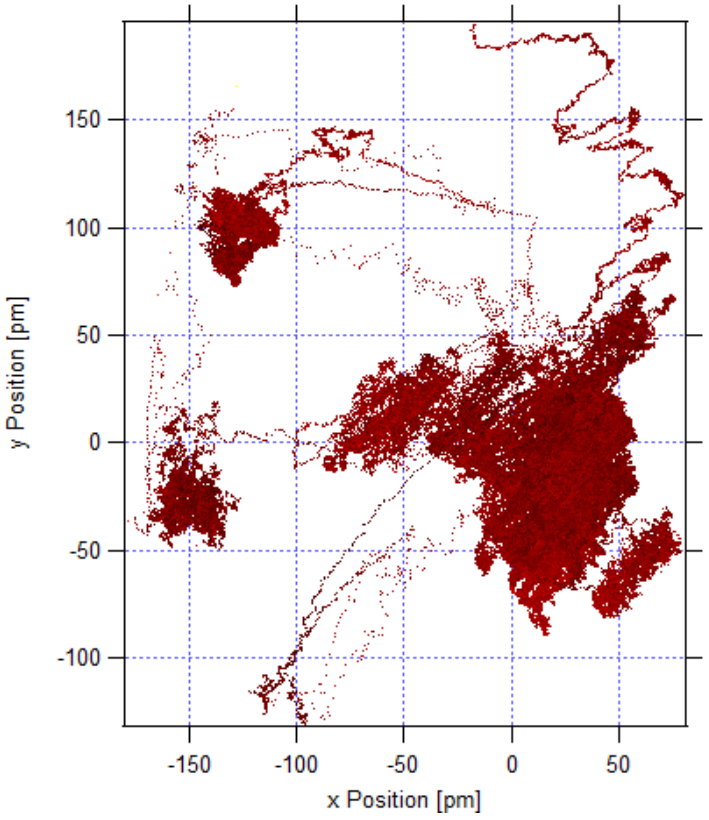

Figure 22. Tracking graph of a Pd_{12} cluster on graphene/Rh(111) that was dosed with CO color-coded with the Z-position (first experiment). Tracking conditions: K_p=0.05, T_i=10 ms, T_s=1 ms, lock-in phase: 335°.

No long range diffusion of the cluster observable upon this CO dosing. The tracking stays calm over a longer period, but some jumps between 100-150 pm can be seen at the end. As for one jump around 2000 s also a movement in the Z channel is observed, it could be that an adsorption of a CO molecule takes place and that this adsorption provokes a movement of the cluster maximum.

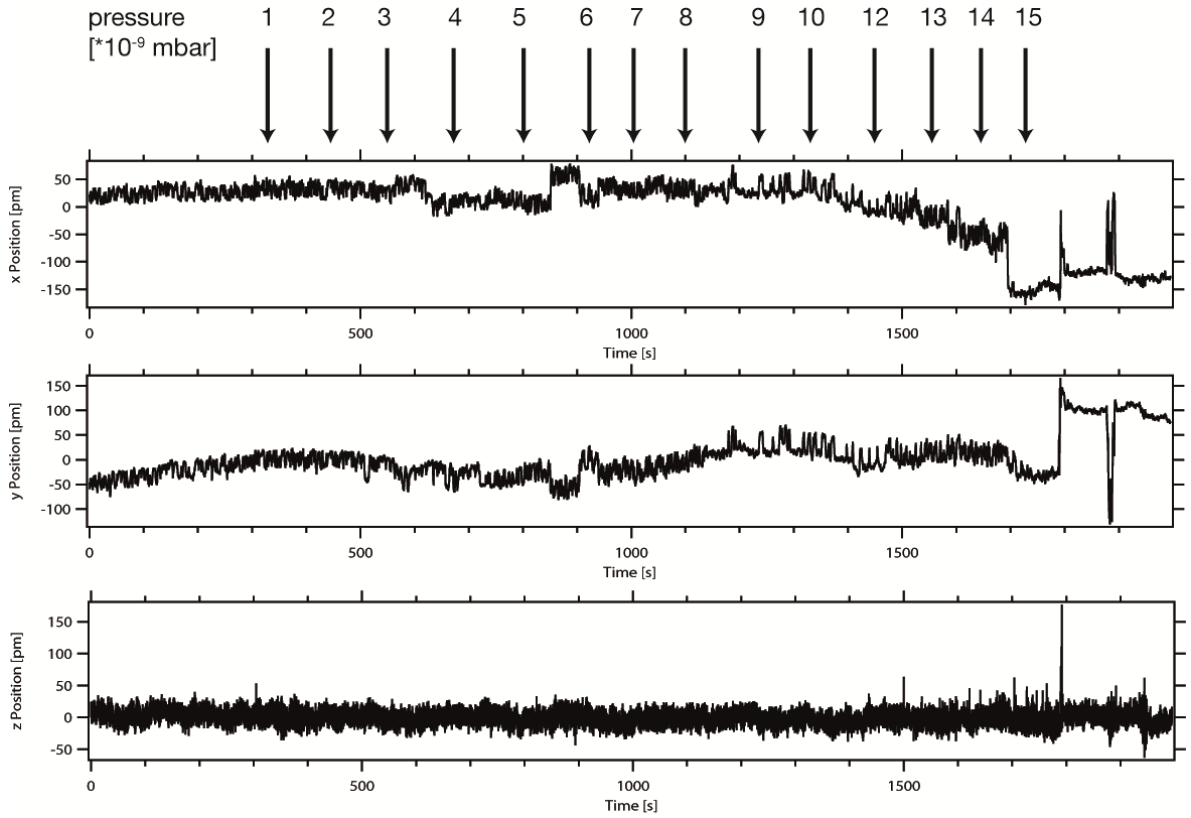

Figure 23. X-, Y- and Z-channels during the tracking with CO background (from top to bottom). The pressure indication reflects the value of the pressure gauge in the STM chamber. At the beginning the background pressure was $6 \cdot 10^{-10}$ mbar.

Regarding the range of the lateral movements, it is hardly possible that the whole cluster moves following a concerted gliding mechanism. It is more probable that CO enhances the mobility of single Pd atoms on top of the cluster and that therefore the maximum of the cluster shifts laterally. Sequential diffusion or edge diffusion of single Pd atoms could be the mechanisms behind this observation.[44c] It could be just as well that a CO molecule provokes a tip change and that this changes the cluster's apparent position.

In another experiment (see Fig. 24 and 25), which lasted twice as long as the former one and was operated until higher CO pressures, one sees still no long-range Diffusion of the cluster, but a jumping of the tip or a shift of the cluster's maximum already at lower pressures. The lateral jumps are in the range of several hundred picometers. Additionally there are zones with more or less noise. The nervousness changes after a jump, which could be mediated by the adsorption or loss of a CO molecule on the tip. The long-time dosing of the CO gas did not allow checking for stable conditions of the cluster after the gas has been switched off, since a tip change upon the gas dosing happened during the tracking.

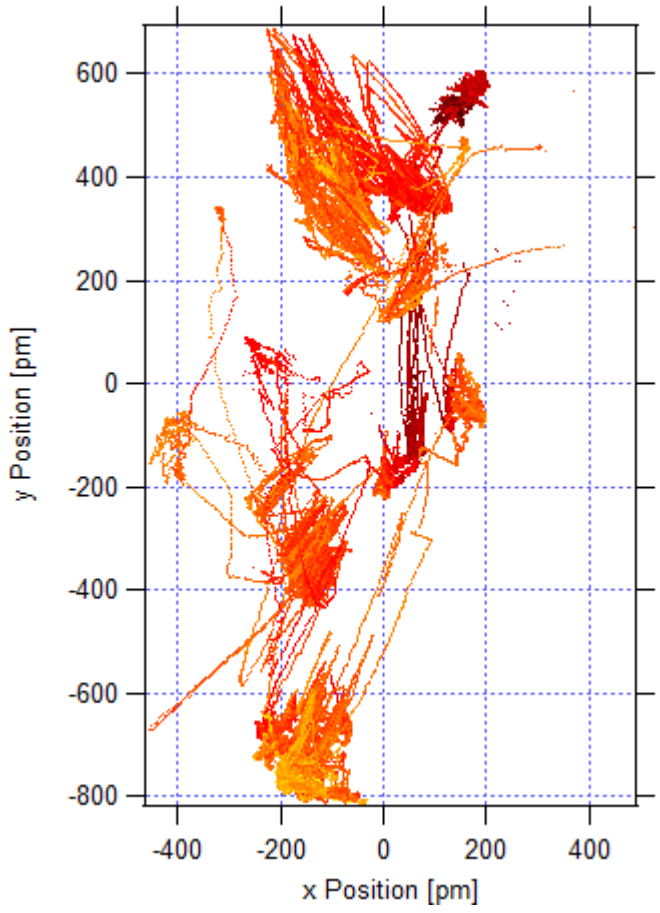

Figure 24. Tracking graph of a Pd_{12} cluster on graphene/Rh(111) that was dosed with CO color-coded with the Z-position (second experiment). Tracking conditions: K_p=0.05, T_i=10 ms, T_s=1 ms, lock-in phase: 325°.

The Z channel does not show any abrupt vertical movements; it is noisy and thus it is hard to subtract the background by the drift correction. The reason for this noise could be the adsorption of CO under the tip or on the cluster. More clear information about the topographic channel could have helped in explaining the fact that after the tracking the cluster has undergone an isomerism and changed from a 1-layer to 2-layer geometry. Nevertheless it is thinkable that CO does not only provoke jumping of single atoms in the horizontal but also in the vertical direction. The isomerization could happen, not by a concerted mechanism but by a multitude of single atom species on the cluster that become mobile through the adsorption of CO.

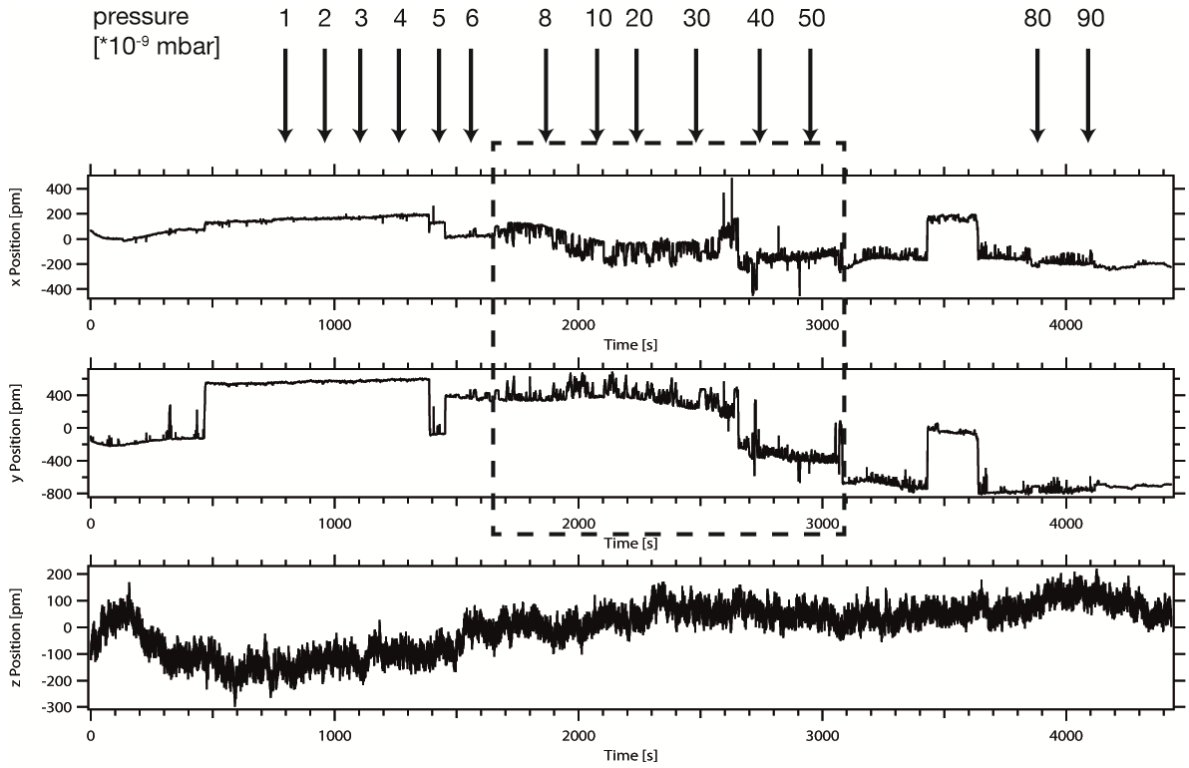

Figure 25. From top to bottom: X-, Y- and Z-channels during the tracking with CO background (second experiment). The pressure indication reflects the value of the pressure gauge in the STM chamber. At the beginning the background pressure was $4.8 \cdot 10^{-10}$ mbar. A particular noisy section is marked by a dashed frame.

This forming of CO adsorption species and their mobility has already been investigated by Parkinson et al.[63] They had a look at Pd adatoms that were dosed on a Fe_3O_4(001)

surface. The adsorption of the CO molecule showed to be responsible for the induction of mobility of the adatom and its coalescence to larger clusters. The coordination of a CO molecule to the Pd adatom competes with the bridge binding of the adatom to the oxygen atom of the ironoxide. As a consequence the binding of the adatom to the ironoxid is weakened and diffusion is facilitated. Such a coalescence effect could not be seen here, because no long range diffusion to another cluster occurred. Nevertheless CO adsorption on Pd atoms could be responsible for the rearrangement of the atoms in the cluster, i.e. the isomerization.

In contrast to the experiments of Gerber et al., our experiments investigated an isolated cluster, whereas on graphene/Ir(111) the mobility of the clusters were documented by STM scans which showed an ensemble of several tens of clusters. The strong effects observed by Gerber et al. are related to the particularity of the Ir(111) support that the Moiré structure is induced by the cluster adsorption itself. Once the clusters unpin, on graphene/Ir(111) the Moiré structure collapses.

Influence of the voltage bias

When investigating dynamics and mobility of particles on surfaces with STM and STM related techniques such as AT, the question arises whether this measuring process is noninvasive and the results are free from effects due to the measuring conditions. Indeed, when keeping the STM tip close to the surface an electric field builds up due to the bias that is applied between tip and surface, there can be effects from inelastic electrons and chemical bonds can be formed. In this electric field, diffusion processes could be inhibited or even accelerated. Hence, it is of utmost importance to find measuring conditions that are least invasive.

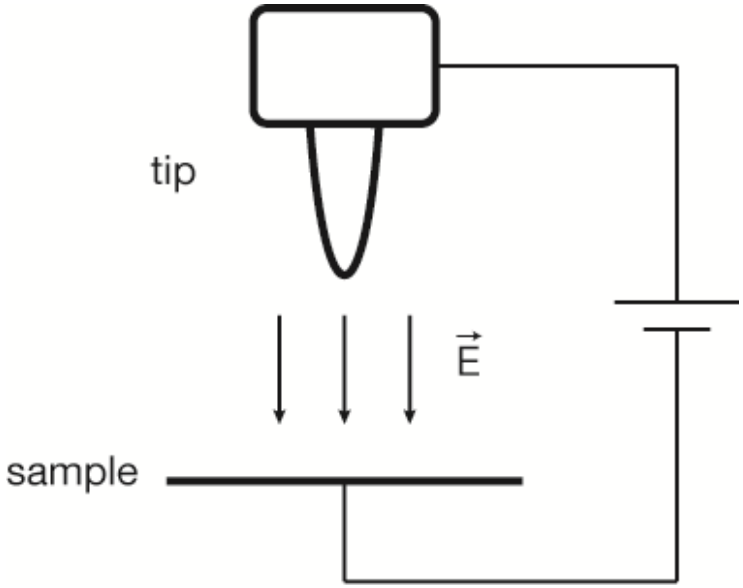

Figure 26. Scheme of the tip-sample set-up in the STM. The non-linear electrostatic field has been drawn linear for a clearer representation.

In their 1998 paper, Swartzentruber and Carpinelli raised the same question and proposed a method to verify the noninvasive measurement.[59] They put the STM tip in the dithering mode over a surface feature, in their case a Si dimer on Si(001), and performed a Z-V scan, while keeping the vertical feedback on. With the bias changing, the tip regulates Z in order to keep a constant tunneling current. Thus, the electric field felt by the Si dimer is directly proportional to the bias divided by the tip-sample distance.

They found what seems to be clear by intuition, that the smaller the bias, the smaller the tip sample distance gets. In total, the electric field is enlarging because the distance decreases more rapidly than the bias. Their conclusion therefore is not to measure at too small bias to avoid a too strong electric field. Strong electric fields, but also large currents can influence the kinetics of the adsorbate, such that they can overcome their intrinsic activation barrier for diffusion.[8b, 64] However in the course of their study they find that the electric field only has a minor influence on the diffusion kinetics: The activation barrier for diffusion only changes by 3%. As all the here described measurements are performed at the lowest possible tunneling current setpoint for our system (1 pA) and as this value

showed not to influence the clusters during conventional STM measurement, an influence on the adsorbate's kinetics by the tunneling current can only be studied once the diffusion is taking place.

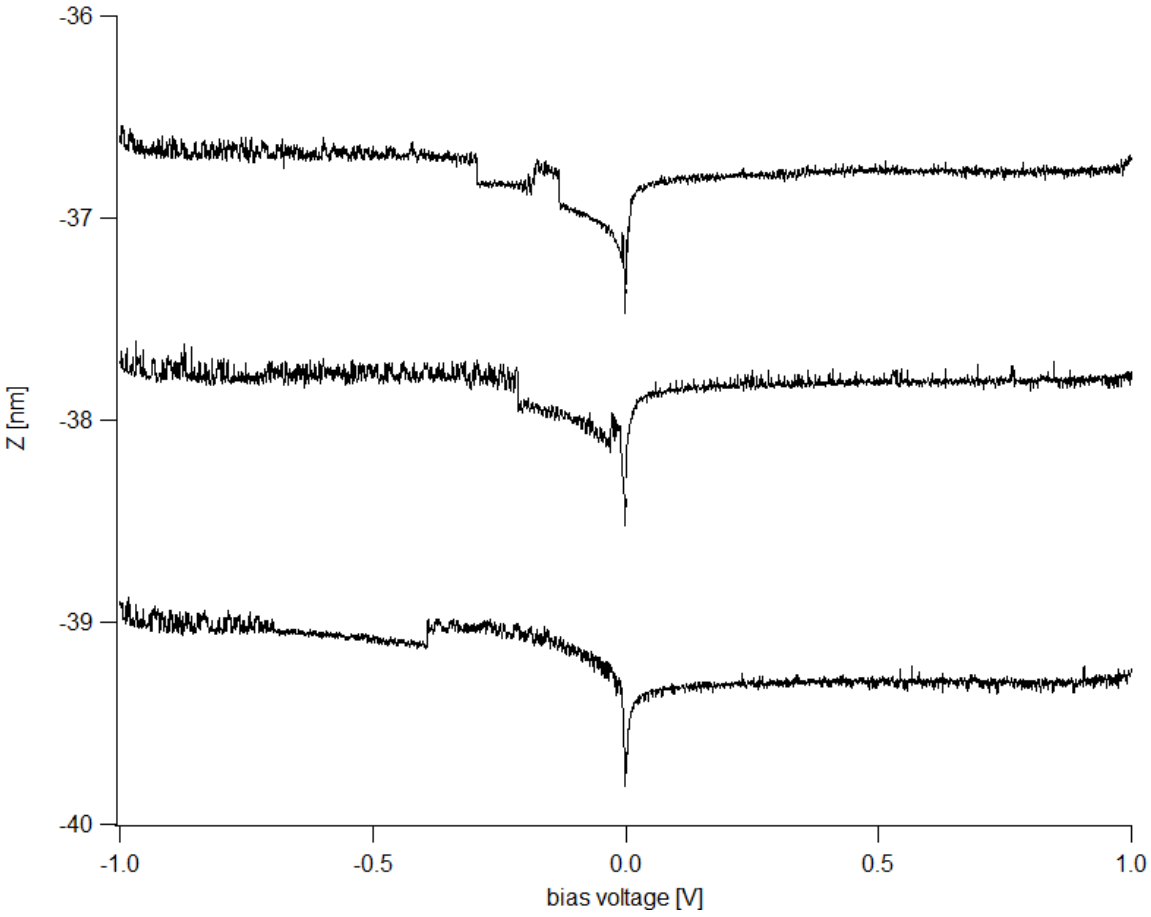

Figure 27. Z(V) spectroscopic measurements with a setup corresponding to a tracking measurement. The voltage has been scanned from -1 V, resp. from +1 V to -1 mV, resp. +1 mV to avoid the zero-crossing. An offset in Z has been added for clearer representation.

In order to check the tip-sample distance in our system with varying bias voltage, similar measurements as in Carpinelli et al. were done for Pd_{12} clusters on a graphene/Rh(111) support. Some of the results of this study are depicted in Fig. 27. Since below a certain

bias the tip-sample distance starts to oscillate and decreases dramatically and since on the negative bias side the erratic behavior of the tip shows pronounced abrupt jumps of more than one Angstrom with a high noise level, the bias for these measurements was kept at a value of +1 V. At this bias the tip-sample distance is around 8 Å (see Fig. 27, compared to the tip-sample touch at 0V) and safe enough to exclude any influence of the tip on the clusters' diffusion kinetics.

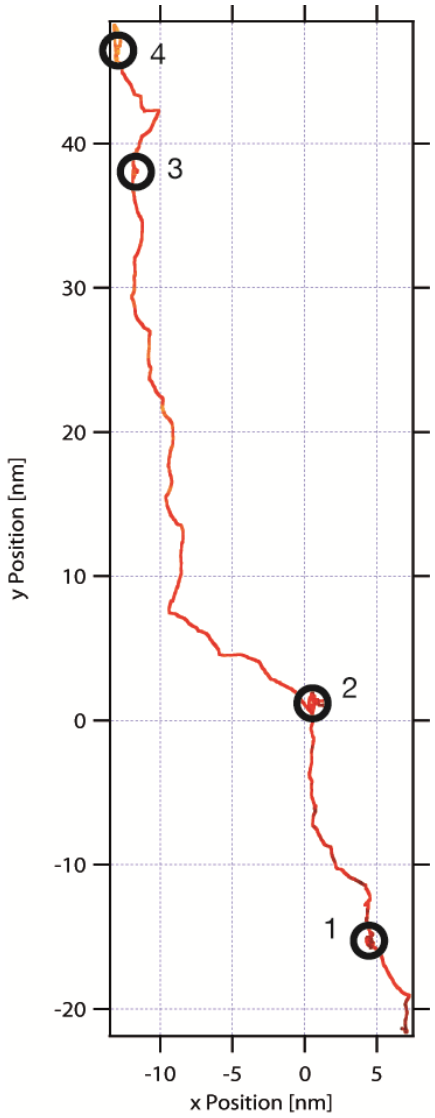

Figure 28. Tracking graph of a Pd_{12} cluster on graphene/Rh(111). The diffusion of the cluster starts only after a decrease of the bias from -1 V to -0.5 V. The black circles mark the resting positions. Tracking conditions: K_p=0.05, T_i=10 ms, T_s=1 ms, lock-in phase: 168°.

Concerning tracking at these conditions, Fig. 28 shows the tracking graph of an experiment where the bias was continuously raised from -1 V in 50 mV steps during the tracking. At around -0.6 mV, the tip shows horizontal instabilities, i.e. in the same range than the Z-channel for the spectroscopy experiments above. At -0.5 V the cluster starts to get mobile and diffuses over the surface. Due to bad tip conditions before and after the tracking, the tracking path could not be correlated to the graphene registry.

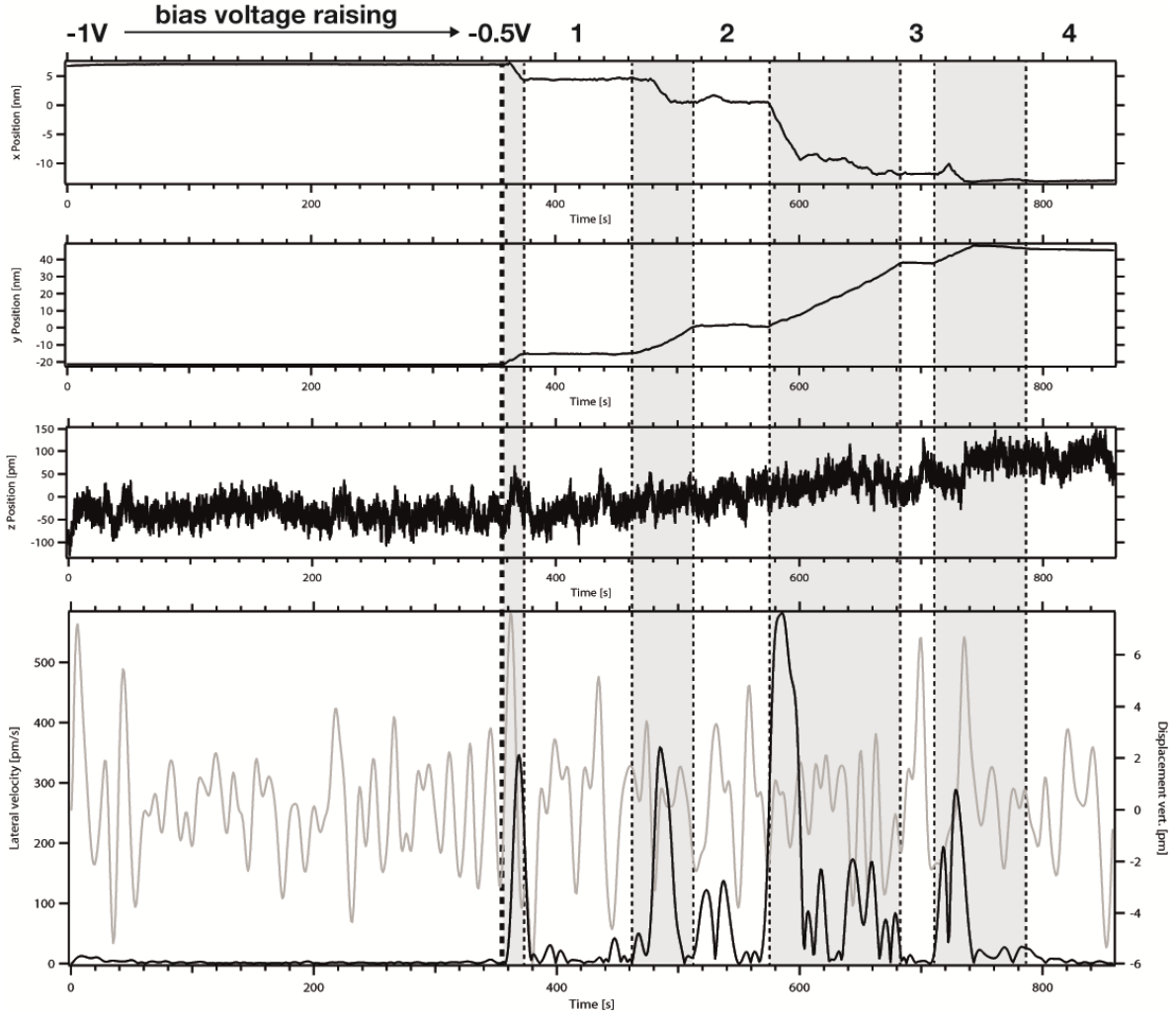

Figure 29. From top to bottom: Evolution of the X-, Y-, Z-channel and the derived lateral velocity and the vertical displacement. The movement phases are underlayed in gray. The numbers mark the resting positions from Fig. 28. The bold dashed line at 360 s marks the beginning of the movement. The Z-channel does not show any interesting feature. Lower part: Lateral velocity (left axis, black) and vertical displacement (right axis, gray) of the tip's position during the tracking.

This experiment shows clearly that a small bias tends to increase the interaction of the tip with the cluster and thereby also the mobility of the cluster. This behavior could only be observed for a bias below -0.5 V. As it can be seen in the following examples, the bias was always held at +1 V to suppress field effects as much as possible.

Track of a cluster in a potential well

Another example for mobility of a Pd_{12} cluster is shown in Fig. 30.

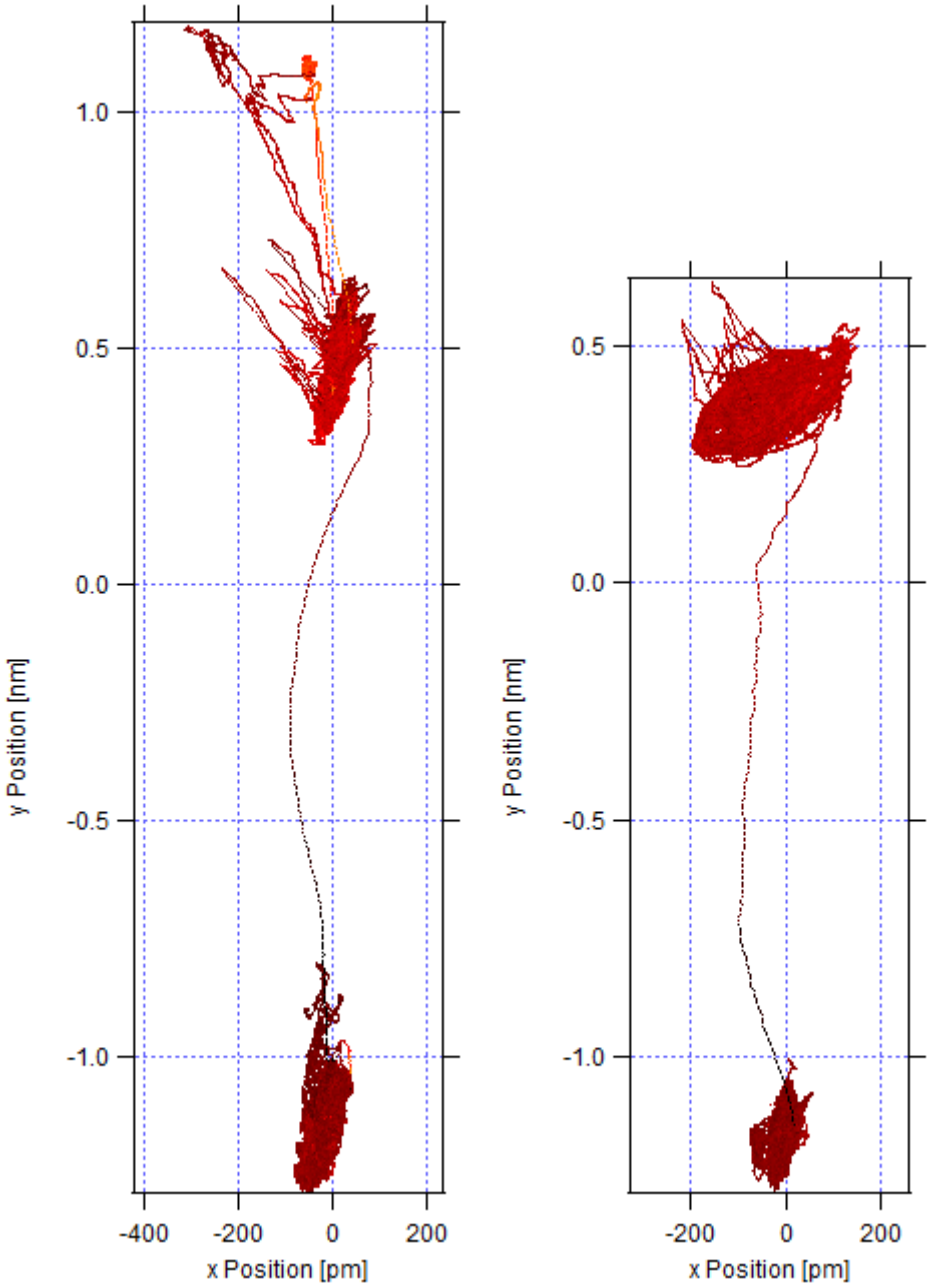

Figure 30. Tracking graphs of the same Pd_{12} cluster performing each time a jump upwards of around 1.6 nm. Tracking conditions: K_p=0.05, T_i=10 ms, T_s=1 ms, lock-in phase: 348°.

In this case the cluster switches between two positions in two neighboring Moiré cells, as can be seen in the tracking graph with the distance of the jumps corresponding to the distance between a ring-fcc site and a ring-hcp site in the Moiré cell (Fig. 31).

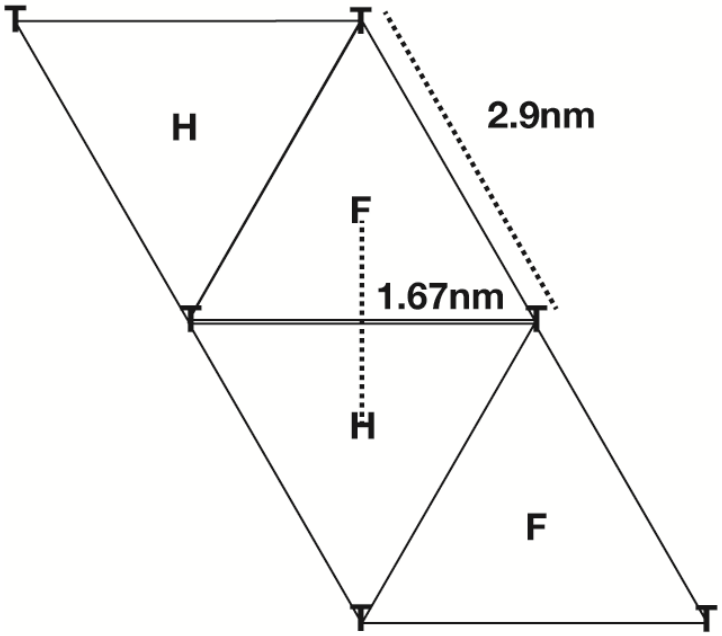

Figure 31. Scheme of two neighbored graphene Moiré cells. The attribution of the high symmetry sites and the Moiré cell length can be found in literature[3b]. The distance between hcp- and fcc-site is calculated by $\frac{\sqrt{3}}{3}a$, with a being the Moiré cell length.

Further proof for this finding can be found in the recording of the Z-channel (Fig. 32).

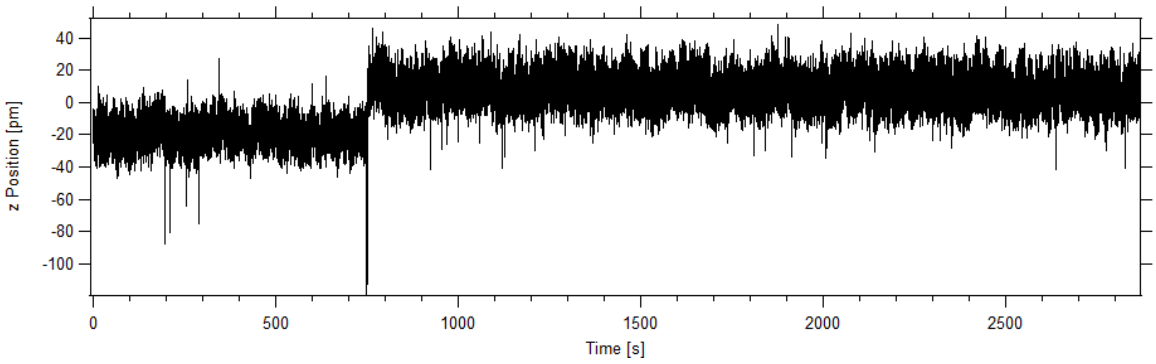

Figure 32. Evolution of the Z-topography channel with time. After 740 s the jump can be recognized by a rising in height of 40 pm. The Z-topography of the second jumps is analogous.

The two adsorption places differ in height by 40 pm, which corresponds to the difference between a ring-fcc and a ring-hcp site on graphene/Rh(111).[65]

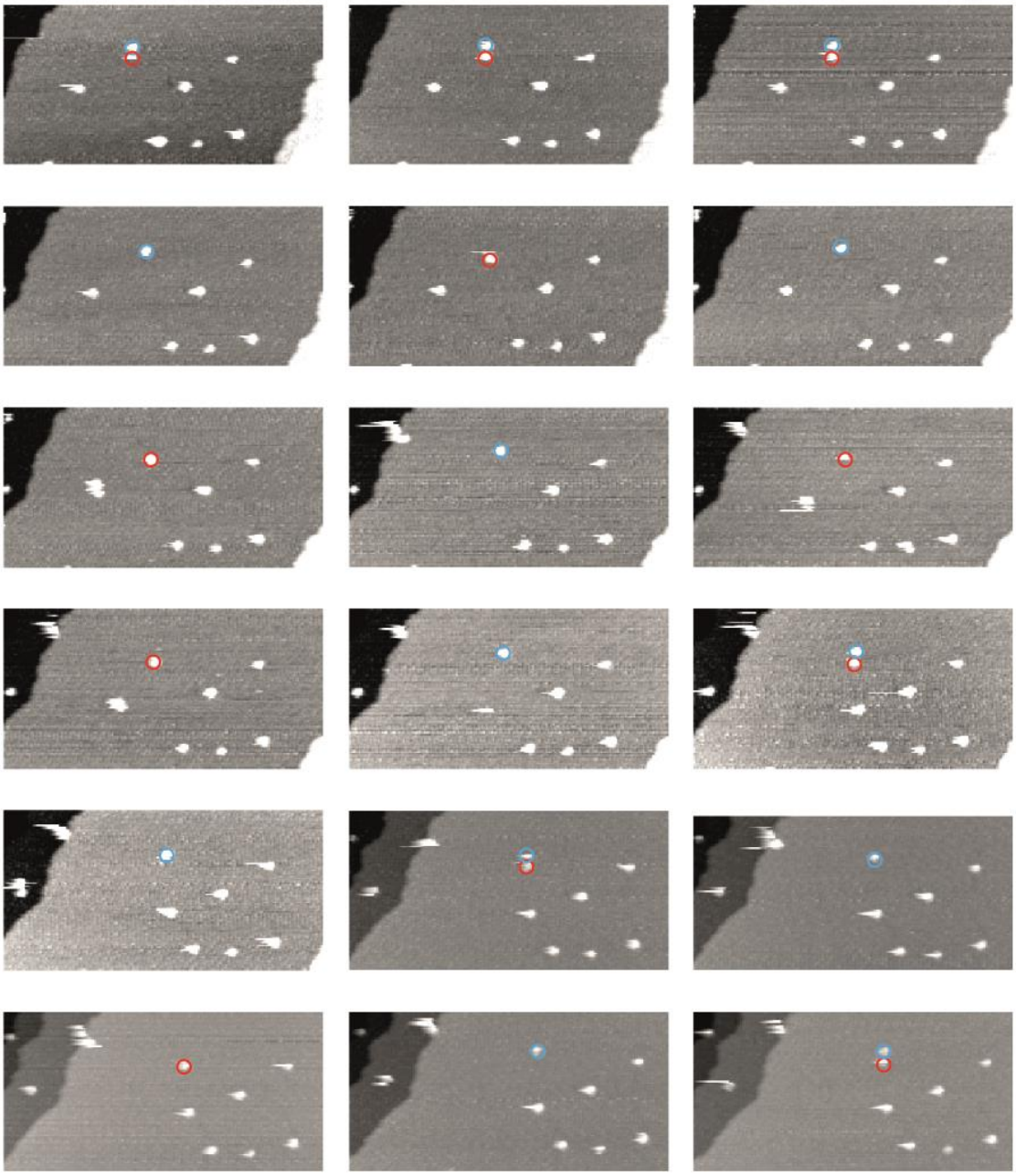

Figure 33. Series of STM topographs of one cluster jumping back and forth between two adsorption sites, with blue colored being in the upper adsorption place and red colored in the lower one. The series lasts for more than 3 hours. Note that a double apparition on the image is due to a jump right at the same time as the tip scans the cluster. Scanning conditions: +1 V, 1 pA.

This switching process can also be observed in an STM image series, where it becomes obvious that the cluster jumps from the lower in the upper cell and vice versa. The graphene superstructure in this series is poorly resolved due to the circular movement that was still on during scanning and because of poor tip conditions. Though, the STM images show that the movement is not tip-directed, as the jump also takes place against the scan direction (from bottom to top). The tip may however influence the hopping rate. In the tracking channels only one jump takes place within 50 minutes, whereas in the STM image series the switching takes place at least five times more often. The STM image series also shows that this switching was stable over a long time and over hours the cluster did not move to a different location.

The question arises why the cluster only diffuses between these two Moiré cells and does not go further away. Due to the poor scanning conditions the underlying graphene substrate cannot be resolved and unfortunately the Moiré structure cannot be derived either. Thus it is not clear whether the surrounding graphene is interspersed with defects and form a 2-minima potential comb, where the cluster is captured, or another phenomenon is involved.

Track of a colliding cluster

In another case a diffusing particle showed an interesting behavior in Z during tracking. Fig. 34 shows the tracking graph of this diffusion event overlaid to a conventional STM topograph taken before the AT.

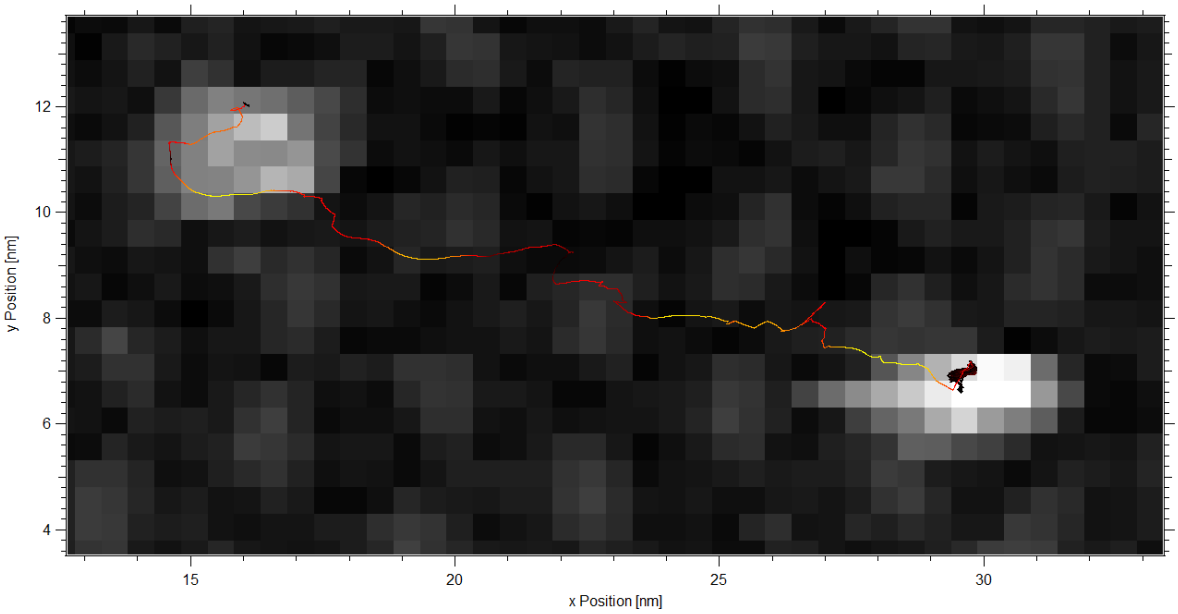

Figure 34. Tracking graph of a Pd_{12} cluster on graphene/Rh(111) color coded with the lateral velocity and overlaid to an STM topographic image taken before the tracking. Tracking conditions: K_p=0.05, T_i=10 ms, T_s=1 ms, lock-in phase: 168°. Scanning conditions: -1 V, 1 pA.

The Pd_{12} cluster diffuses from the lower right to the upper left corner of the considered section of the graphene substrate and stops 15 nm away from the starting point. Considering that in the previous case the diffusion stopped because of a step edge, here, no step edge was in the vicinity. A closer look to the Z-mapping of the diffusion pathway shows that the Z-channel recorded several jumps that are in the range of an interlayer distance in Pd. It seems that the cluster isomerizes several times during the diffusion. At the end of the tracking the cluster is higher than in the beginning.

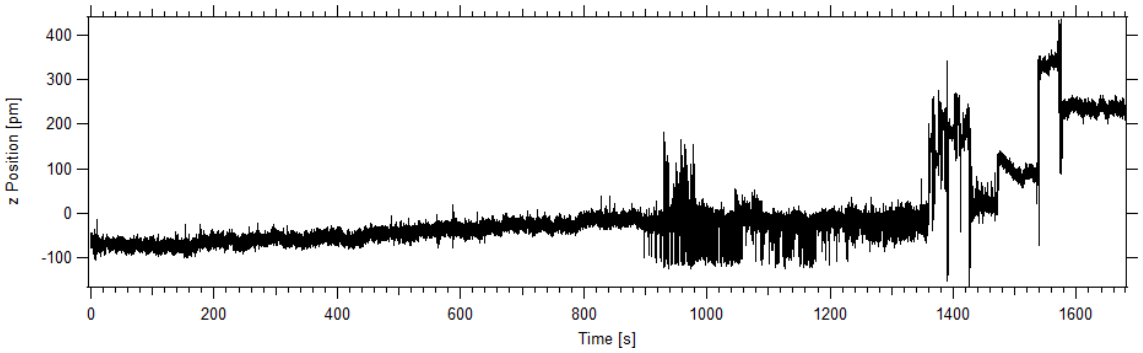

Figure 35. Evolution of the Z-topography channel with time. During the tracking after around 1500 s the Z-channel shows several jumps that are in the range of atomic layers.

The STM scan preceding the tracking reveals why the cluster stopped its diffusion. At the position where the cluster stops, there was another cluster before tracking. Assuming that this cluster has not moved during the tracking, the two clusters might have coalesced.

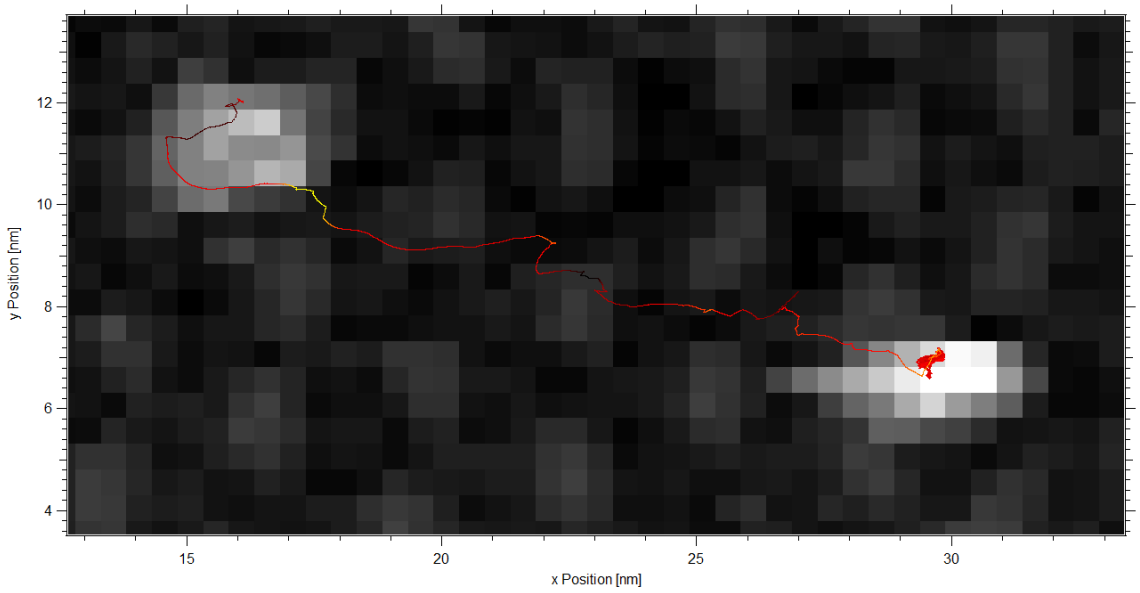

Figure 36. Tracking graph of a Pd_{12} cluster on graphene/Rh(111) color coded with the vertical displacement and overlaid to an STM topographic image taken before the tracking. The color coding reveals the raising of the vertical displacement just before the diffusing cluster hits its neighbor.

The feature observable in the Z-channel corresponds therefore to a coalescence process. Such a process has already been observed in our laboratory by imaging of Pd_{19} clusters

on Rh(111) at a higher coverage at 50°C.[31] The corresponding time lapse movie of the consecutive STM scans shows a fuzziness in the cluster's shape (streaks in x-direction). Some frames out of this movie are shown in Fig. 37. This fuzziness might indicate peripheral diffusion of adsorbate molecules that induce the diffusion process.

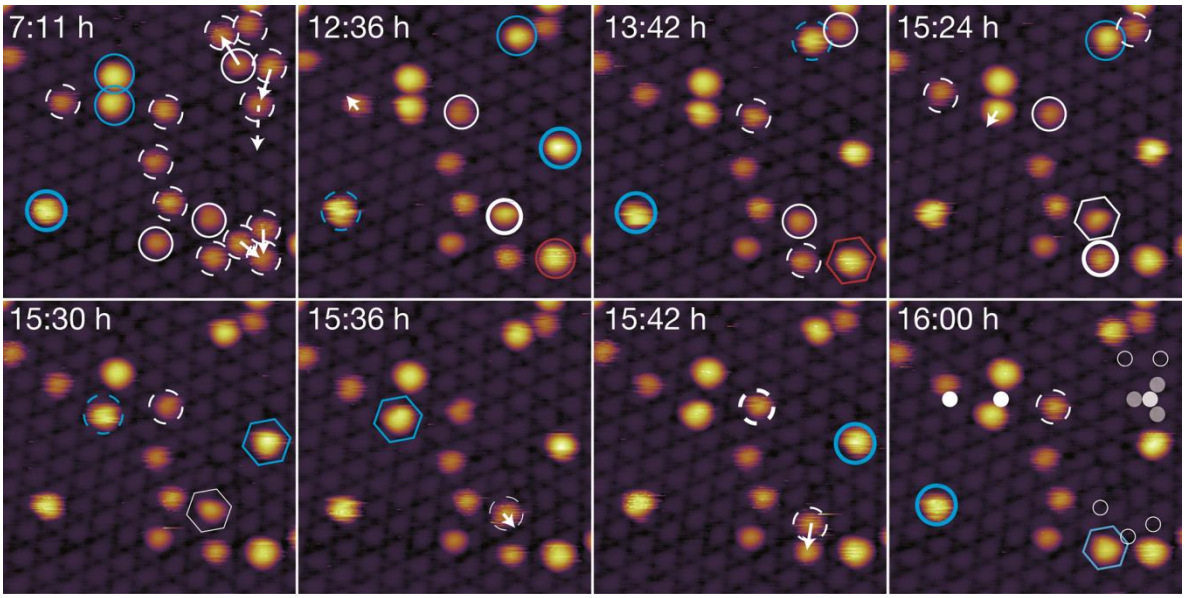

Figure 37. Evaluation of ripening processes of Pd_{19} clusters on graphene/Rh(111) at 323 K. White circles represent Pd_{19}, blue circles Pd_{38} and red circles Pd_{57}. Image sizes: 34 x 34 nm^2. Imaging conditions: -1 V, 1 pA. This figure is part of the thesis of Michael König and has been reproduced with the permission of the author.[31]

The vertical displacement in this case confirms the collision, as it shows a positive contribution right in the vicinity of the colliding cluster (Fig. 36). Upon merging the two clusters form a new 2-layer high Pd_{24} cluster which is more stable towards diffusion than the single Pd_{12} cluster, due to its larger footprint. The new cluster just slightly moves within the Moiré cell in order to find the optimal adsorption place and stops there. A zoom-out of this area after the tracking (Fig. 38) shows another cluster neighbored to the merged cluster. The measured distance between these two upper neighboring clusters is decreased after the tracking, which is in agreement with the shape of the tracking path. Also the height increase of the merged cluster can be seen in this figure.

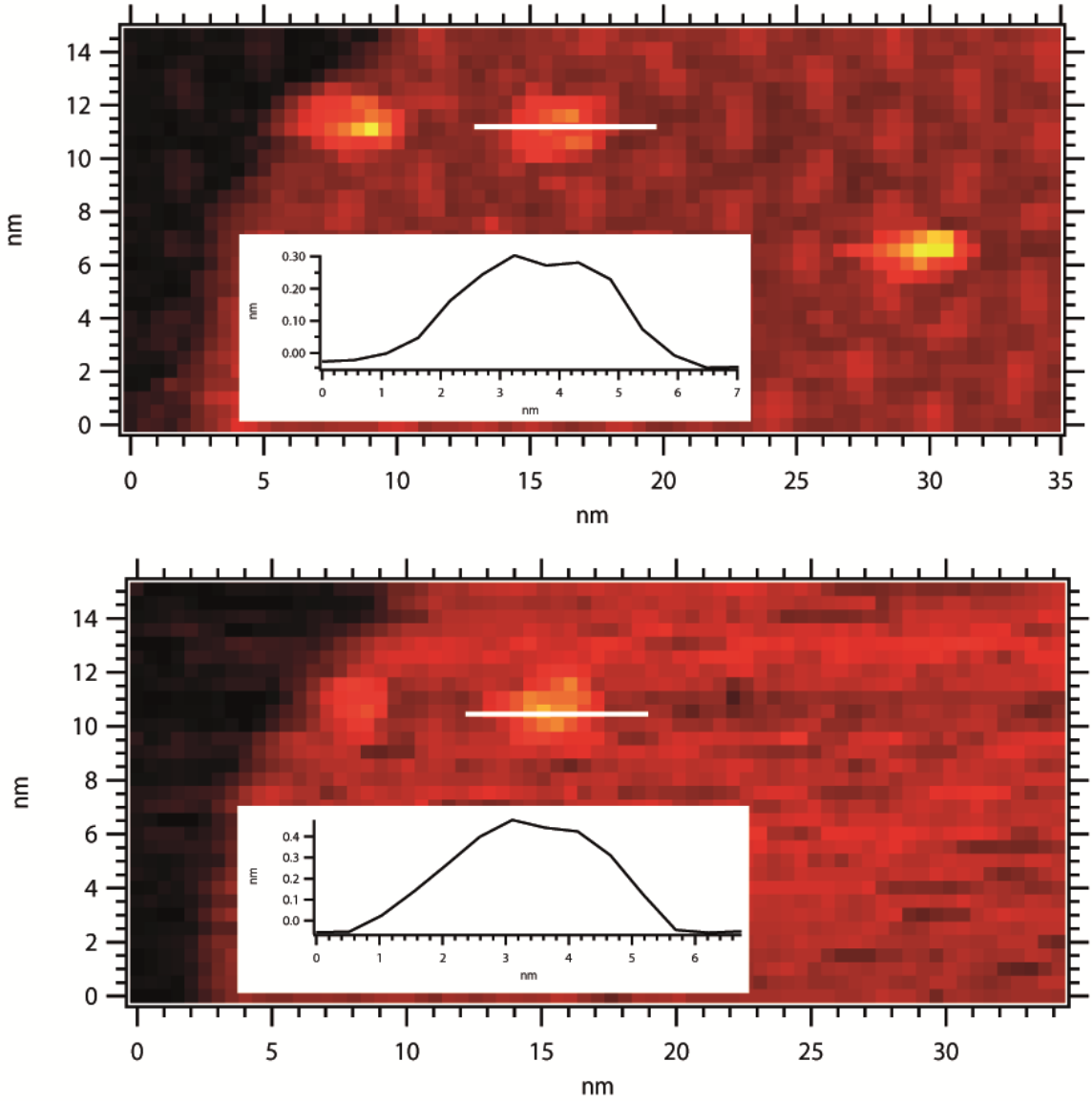

Figure 38. Upper part: STM topograph taken before the scan an overlaid to the tracking graph in the preceeding figures. Lower part: STM topograph taken after the tracking. The quality of the tip in the second scan is worsened, but nevertheless the line profiles, represented by white lines, reveal an increase in height of the cluster in the middle from a 1-layer to a 2-layer cluster.

The lateral velocity shows an increase when moving away from an adsorption place and a decrease when moving towards (Fig. 34). In two places the cluster decelerates more, up to nearly stopping, which are two different adsorption sites, notably ring-fcc and ring-hcp sites. This shows again that on graphene/Rh(111) both sites are equally frequented.

Track of a cluster diffusing over a step edge

In all of the experiments the Pd_{12} clusters were soft-landed on a graphene on Rh(111) surface at a low coverage in order to avoid coalescence of the clusters already before the measurement and collisions of the cluster under investigation during the measurement.

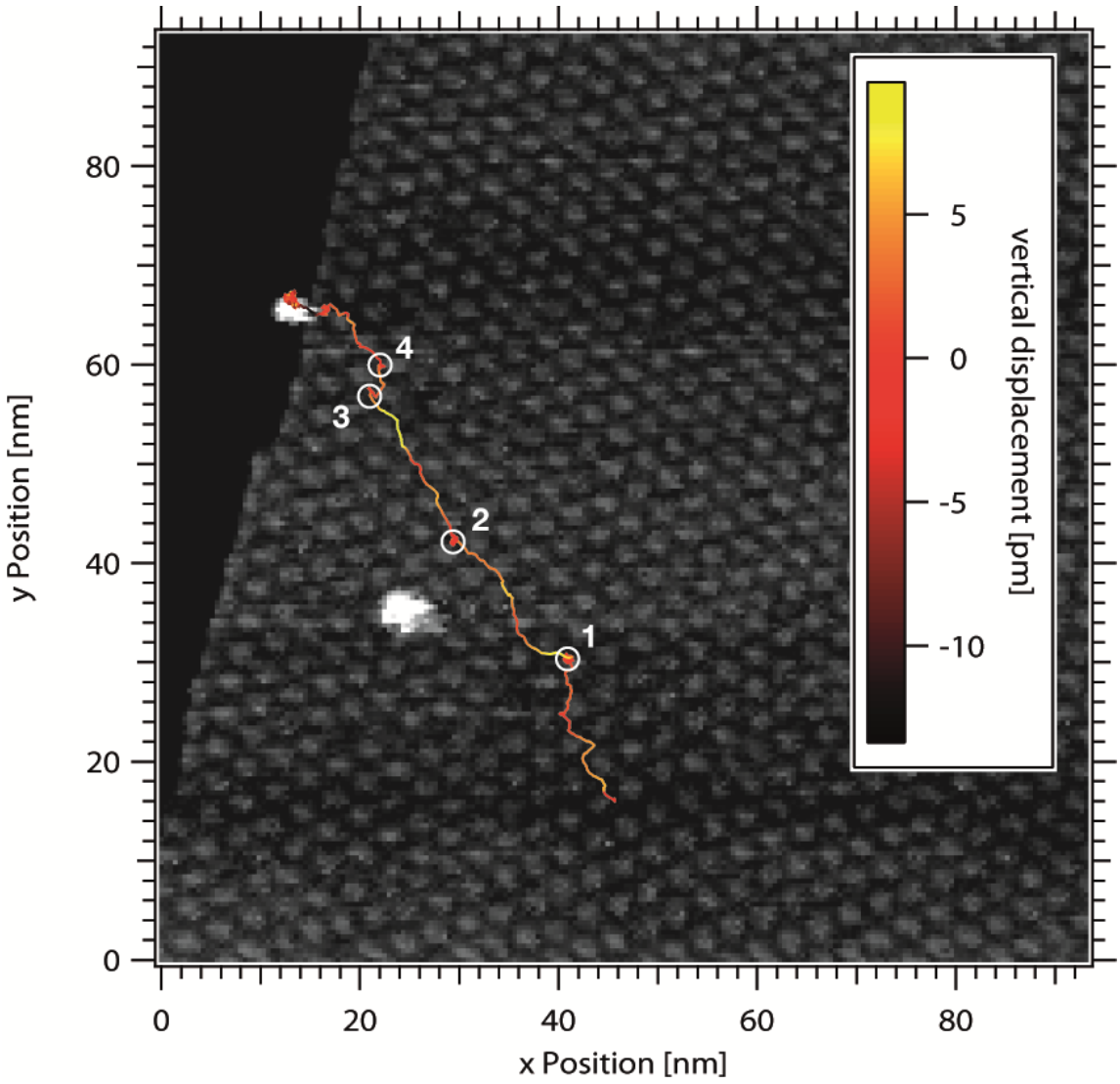

Figure 39. Tracking graph of a Pd_{12} cluster on graphene/Rh(111) color coded with the vertical displacement and overlaid to an STM topographic image taken after the tracking. The starting point has been determined using STM overview images of less quality taken before the experiment (see Fig. 40). The numerated white circles mark the four main resting points. Tracking conditions: K_p=0.05, T_i=10 ms, T_s=1 ms, lock-in phase: 348°. Scanning conditions: +1 V, 1 pA.

On periodic surfaces, references (clusters or step edges) are needed; hence the coverage should not be too low. Some, in the best case, immobile clusters should be present on the same section of the surface, which will be helpful in reconstructing the start and the end point of the tracking. Characteristic step edges act in the same way with the advantage that they are not mobile in any case. The starting as well as the end point are sometimes difficult to define correctly, because the STM images taken before and after the tracking often show large differences in imaging quality. Switching the AT on or off is associated to an abrupt change in the tip's direction and velocity (circular movement) and can thus provoke changes of the tip apex and though the quality of the imaging. These changes can be reduced by placing the tip as near as possible to the cluster before activating the AT and by programming waiting times in the start and end procedures.

In Fig. 39 the track of a Pd_{12} cluster is overlaid to a STM image taken some time after the end of the tracking. This overlay is not arbitrary. The start point can be defined using an image taken before the tracking (see Fig. 40) and showing the same large cluster as on Fig. 39 on the lower left side.

To find the correct end point is trickier though, because the cluster slightly moved after tracking and before taking the STM image in Fig. 39. Nevertheless, thanks to STM images of poorer quality that have been taken in the meantime, the position of the cluster at the end of the tracking could be reconstructed. In addition to this, the four main resting positions of the cluster during its drive over the terrace help to align the trace to the image. These resting positions - marked by white circles in Fig. 39 - are supposed to coincide with ring-fcc or ring-hcp binding sites.

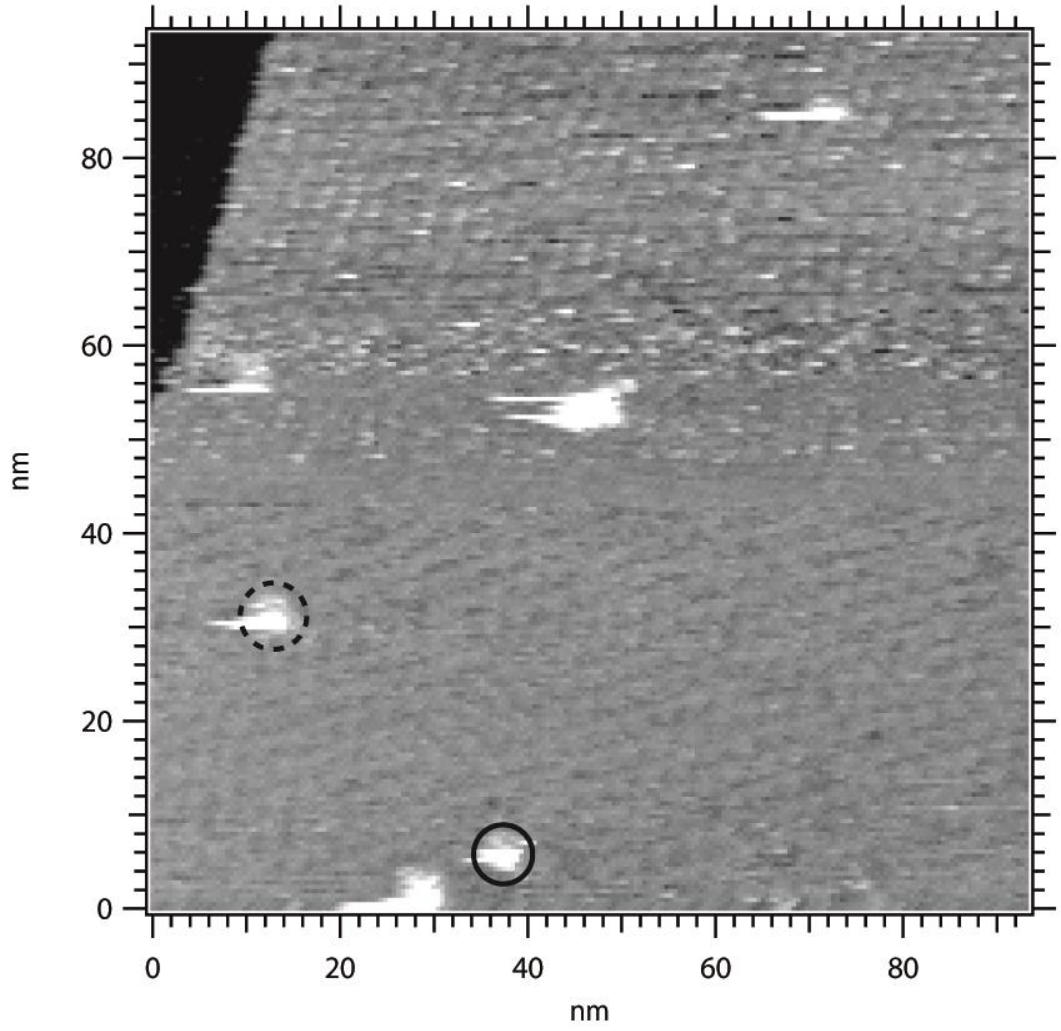

Figure 40. STM scan taken before the tracking and showing the position of the cluster (full circle) at the beginning relative to the stable cluster (dashed circle), which remains at its position even after the tracking. Using the faintly appearing Moiré structure of this image the original position of the cluster could be determined in Fig. 39.

In Fig. 39, the track shows that the cluster diffuses towards the step edge of the surface by avoiding the top sites of the Moiré superstructure. This draws an analogy to the theoretical calculations that have been done for clusters on graphene/Ru(0001).[24b] Eventually the cluster hops to the lower terrace. At the marked positons the cluster stops for a moment and continues its movement again. These spots lie in between three top sites and correspond to the fcc/hcp binding sites also shown in reference [24b]. In the

case of graphene on Rh(111), the energy difference for cluster adsorption in the fcc and in the hcp site is smaller than on Ru(0001), which explains that on graphene on Rh(111) clusters bind in both sites in equal shares, whereas on graphene on Ru(0001) the clusters nearly exclusively bind in the fcc site. Furthermore, one can differentiate the diffusivity of a one-layer from that of a two-layer isomer of Pd_{12}, the two-layer isomer being more mobile because of the reduced footprint. Fig 41 shows a modified figure of this reference, which summarizes a STM scan series documenting the diffusion of the Pd_{12} clusters. Note that in this study we presented single diffusion steps of the Pd_{12} clusters (represented by white dashed lines in Fig.41), but we have also observed clusters that cover a distance of more than 20 nm in 20 min.

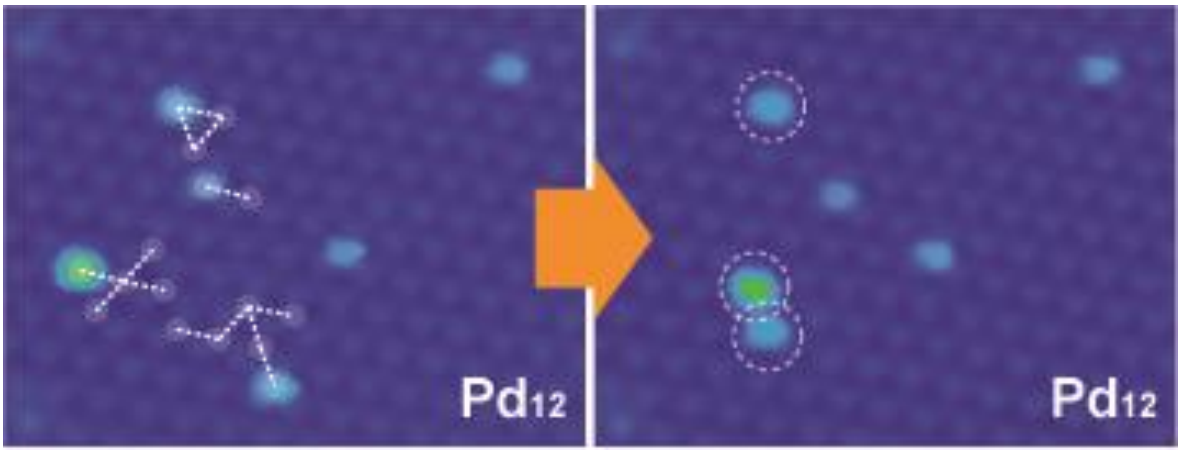

Figure 41. Isomer-dependent diffusion of Pd_{12} clusters on graphene on Ru(0001) under scanning conditions at RT in a time series over 20 min (Δt = 1 min). All observed trajectories are indicated on the left side. They have no preferential direction and are thus not dictated by the scanning direction. The 2-layer isomers, that is, those with smaller footprint, show higher mobility. Image sizes 41 x 31 nm^2; imaging conditions, +1 V, 100 pA. Reprinted (adapted) with permission from [24b]. Copyright 2015 American Chemical Society.

The mobility of the Pd_{12} clusters on the two different supports cannot be compared in absolute values due to the lower cluster binding energies on Rh(111). On graphene/Ru(0001), the clusters hop from one cell to a neighbored one, whereas on

graphene/Rh(111) the movement steps range over several Moiré cells. Nevertheless, we can estimate the mean displacement over a time range that is for both experiments of around 20 min. On one side, the AT measurement shows only one diffusion event, whereas the STM series documents a dozen of events in the same time. On the other hand the cluster density is around one magnitude lower in the AT measurement than in the STM series. As a conclusion the mobility of Pd_{12} clusters is in the same range for both the scanning and the tracking.

When considering the diffusion of the cluster on a more global scale, it is possible to calculate the diffusion constant and the related exponent of the diffusion time step by analyzing the data of the cluster's movement using the formula presented in the theoretical overview. By plotting the mean square displacements against the time needed for this displacement and fitting the graph using a power function results in a general diffusion constant D of $4.75 \cdot 10^{-21}$ m^2/s and an anomalous parameter α of 1.9 (see Fig. 42). This means that the diffusion process observed is superdiffusive, but the anomalous parameter is close to 2, which corresponds to a ballistic movement, or to pure drift and which can be influenced by the tip. The diffusion constant in our case is much smaller than the value of the diffusion constant of atomic Rh adsorbates on Rh(111) ($D_0=2 \cdot 10^{-8}$ m^2/s) found in the literature.[44c]

As can be seen in Fig. 39, once the 2-layer cluster in movement, it only stops at defined capture positions and makes longer runs over several Moiré cells without stopping at one of the intermediate potential adsorption positions. The fact that the cluster does not stop in the neighboring cell underlines that the cluster has to dissipate energy in order to hit the next wettable site. This brings to mind the concept of Lévy-flights, which was presented in the introduction to this chapter. In this case longer resting periods are

followed by longer jumps. Only if the cluster approaches strong binding sites it can be captured. Nevertheless, this process will require efficient energy dissipation. Otherwise the cluster would continue its movement and would rush past the binding site.

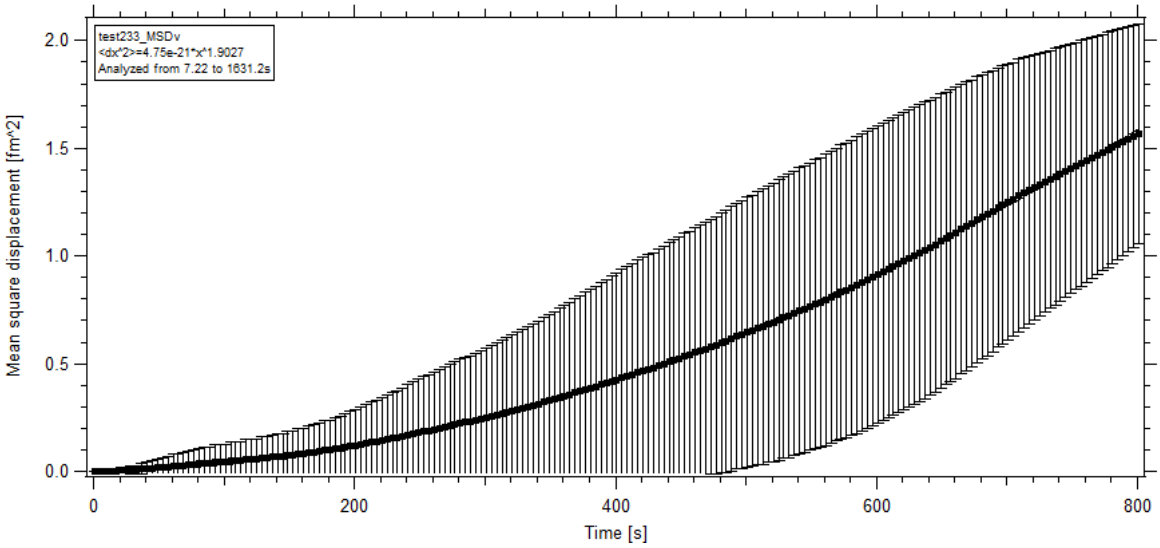

Figure 42. Mean square displacement of time intervals from 0 to 800 s. The considered data exclude the time before the first and after the last movement. Note the large error bars for large displacements (large times) due to restricted statistics.

This fact allows postulating that the cluster's diffusion on graphene follows a Lévy flight type behavior with long flight intervals in between the resting points, as it was already described in the theoretical approach. Hence, during its movement, the cluster leaves out several potential adsorption places in between the resting positions. The reason why the cluster does not bind to these intermediate places might simply be the fact that once the cluster having enough energy to overcome one barrier, it can overcome some more and continues its motion. Other examples of such diffusion processes can be found in literature [50, 66]. In some of these cases the reduced affinity of binding to a neighbored binding site is attributed to the low friction of the particle on the support and thus relates

this type of movement to a rollercoaster. Thus graphene/Rh(111) seems to be a support for clusters that is very slippery when they are far from the wetting sites.

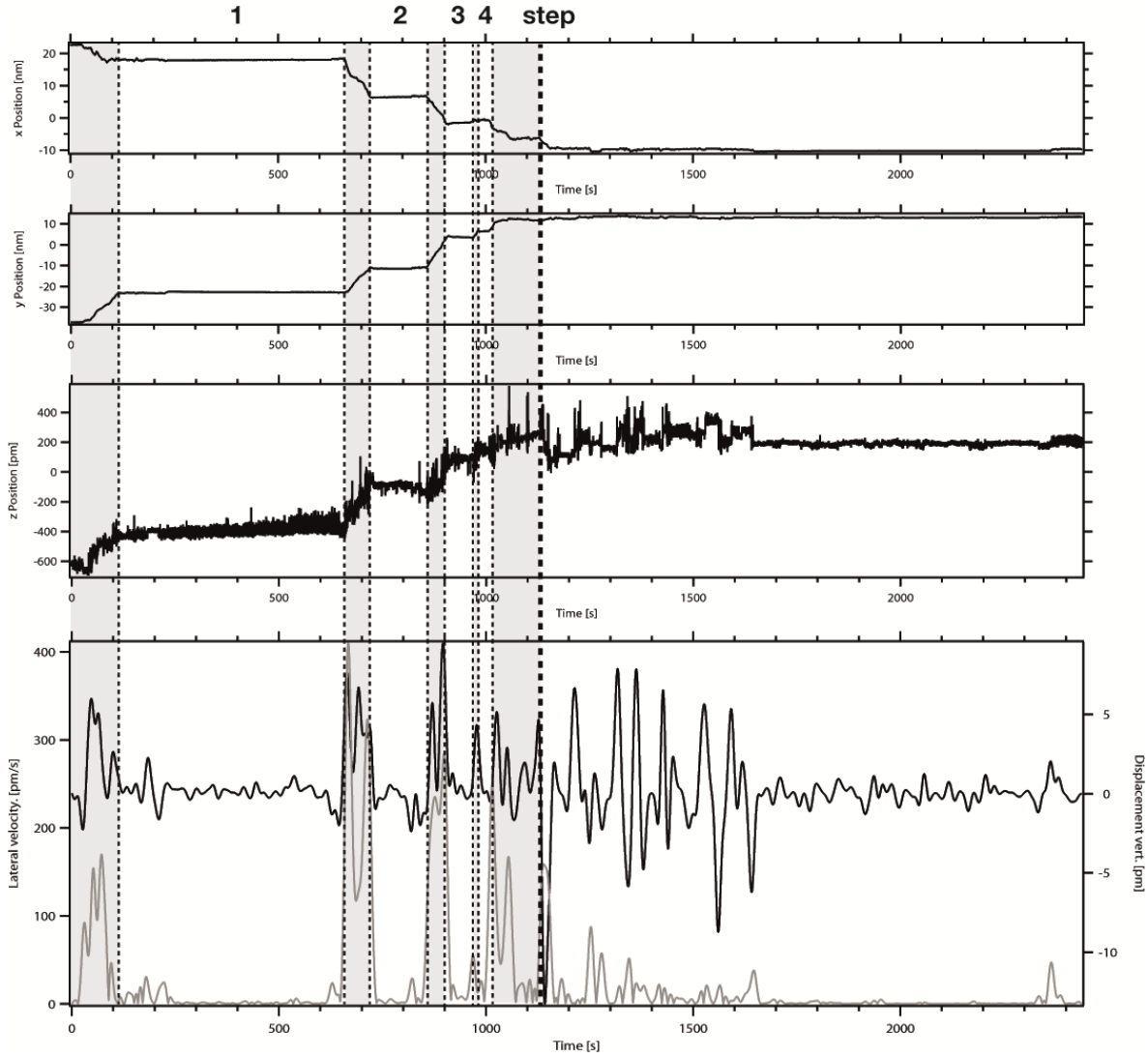

Figure 43. From top to bottom: Evolution of the X-, Y-, Z-channel and the derived lateral velocity and the vertical displacement. The movement phases are underlayed in gray. The numbers mark the resting positions from Fig. 39. The bold dashed line at 1130 s marks the step to the lower terrace. After the step the cluster stays fix at its position, whereas the Z-channel still displays vertical movements. Lower part: Lateral velocity (left axis, gray) and vertical displacement (right axis, black) of the tip's position during the tracking.

When having a look at the Z-channel, no clear feature of the step edge or of other vertical interaction is visible. The Z-channel is very noisy in between the marked resting zones. The information from the Z-channel can be transformed into a vertical displacement by calculating the displacement from one measuring point to another and smoothing the

resulting curve. Dividing by the time increment thus gives the velocity of the cluster at that specific increment. In fact, this transformation corresponds to the first derivative of the Z-channel. Thus more information can be extracted.

In between the four main resting points the vertical displacement is higher. During its trip over the Moiré cells, the cluster has to face bridge sites and comes close to top sites, so the barrier it has to overcome is not only energetically but also geometrically higher. After 1130 s the vertical displacement in the lower graph of Fig. 43 (black line) breaks down exactly when encountering the step edge and in correspondence to the diffusion of the cluster to the lower terrace. This movement down the step is related to the overcoming of a barrier. A zoom-in of this step edge region is displayed in Fig. 44.

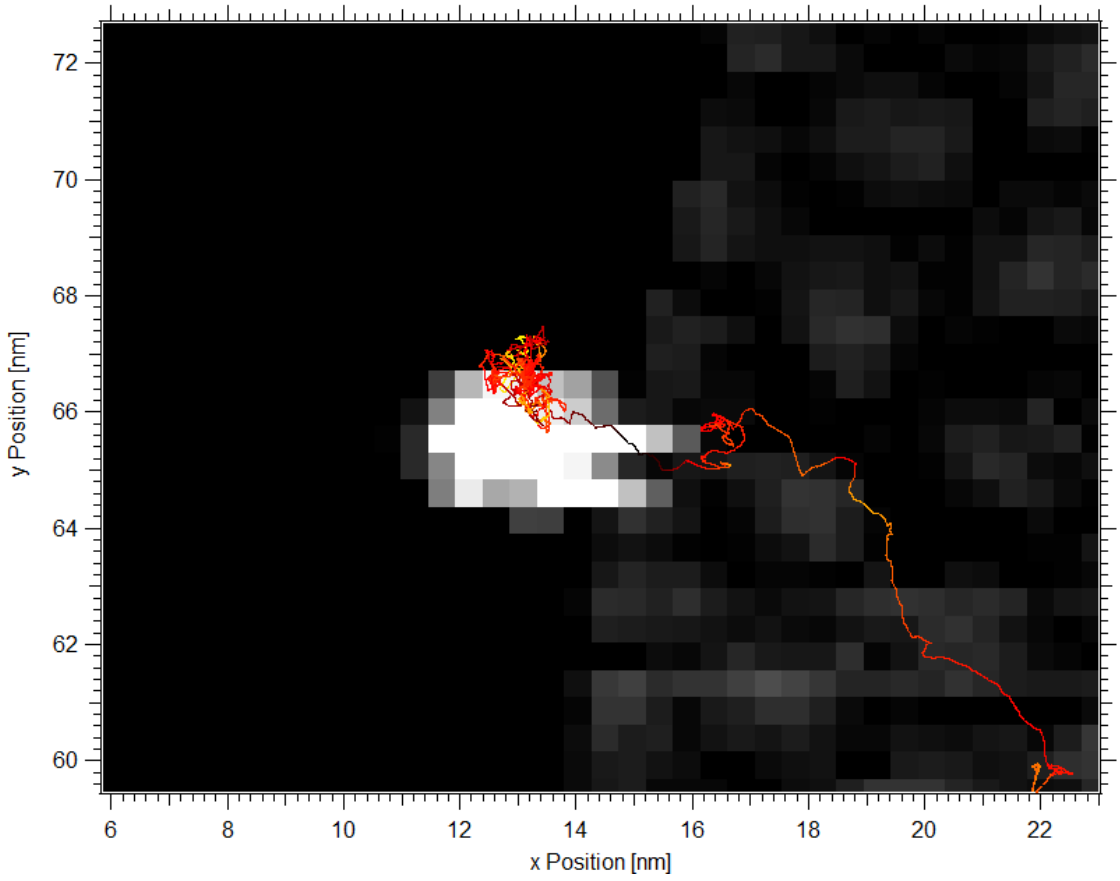

Figure 44. Detail of the tracking graph of the Pd_{12} cluster on graphene/Rh(111). The color coding shows the abrupt collapse of the vertical displacement at the exact position of the step edge.

The following jumps in the Z-channel as well as in the displacement channel can be attributed to an isomerization process of the cluster coordinated to the step, the cluster having a new 3-layer geometry. This isomerization is associated to a fuzzy phase in the Z-channel and followed by a quiet phase, upon which the cluster continues moving along the step after the tracking. The quality of the Z-channel shows that it is reliable on a short term, but that drift is still acting in this direction, which is problematic on the long term.

The same analysis can be done with the lateral channels and the resulting lateral displacement (or velocity) can be overlaid to the tracking path (Fig. 45). There are extended periods of high velocity and in between, at the resting sites, the displacement is smaller.

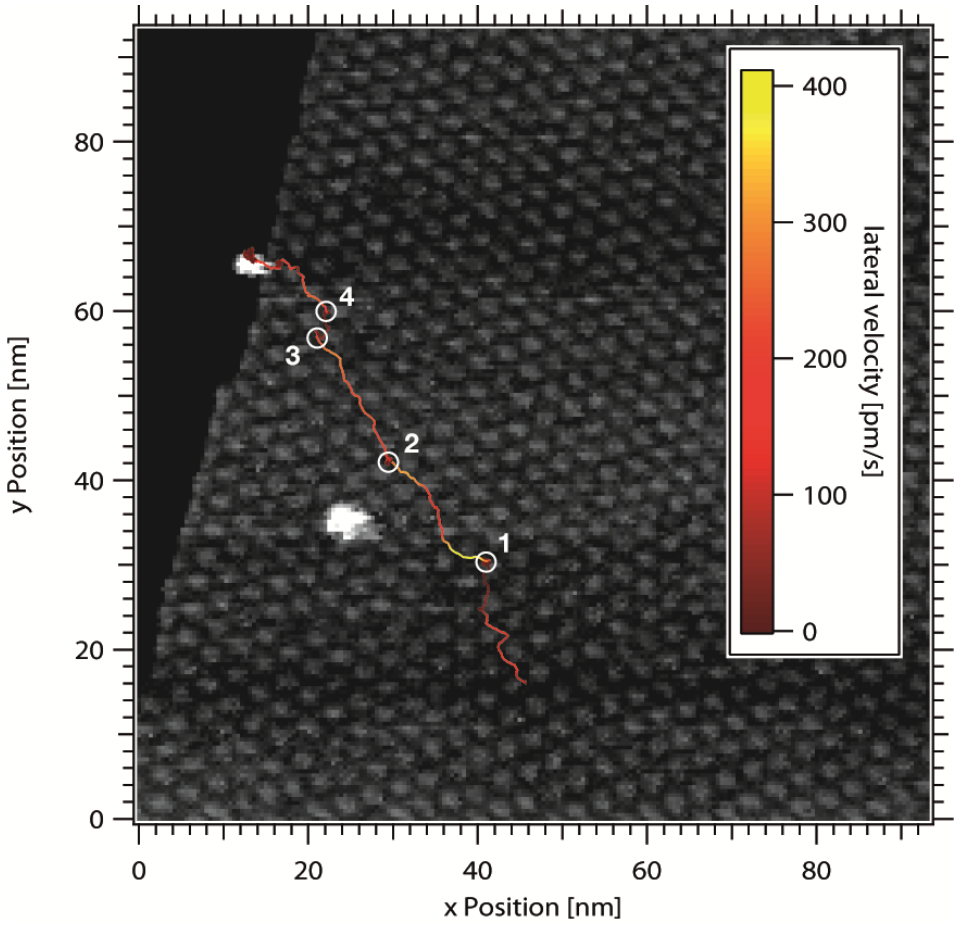

Figure 45. Tracking graph of the Pd_{12} cluster on graphene/Rh(111) color coded with the lateral velocity of the tip. The tracking and scanning conditions are identical to Fig. 39.

It also becomes visible that the cluster decelerates, when coming close to a resting position and accelerates, when diffusing away. In the case of diffusion towards the ring-fcc and ring-hcp sites respectively, the binding energy barrier increases. This can decelerate the cluster, if energy is dissipated.

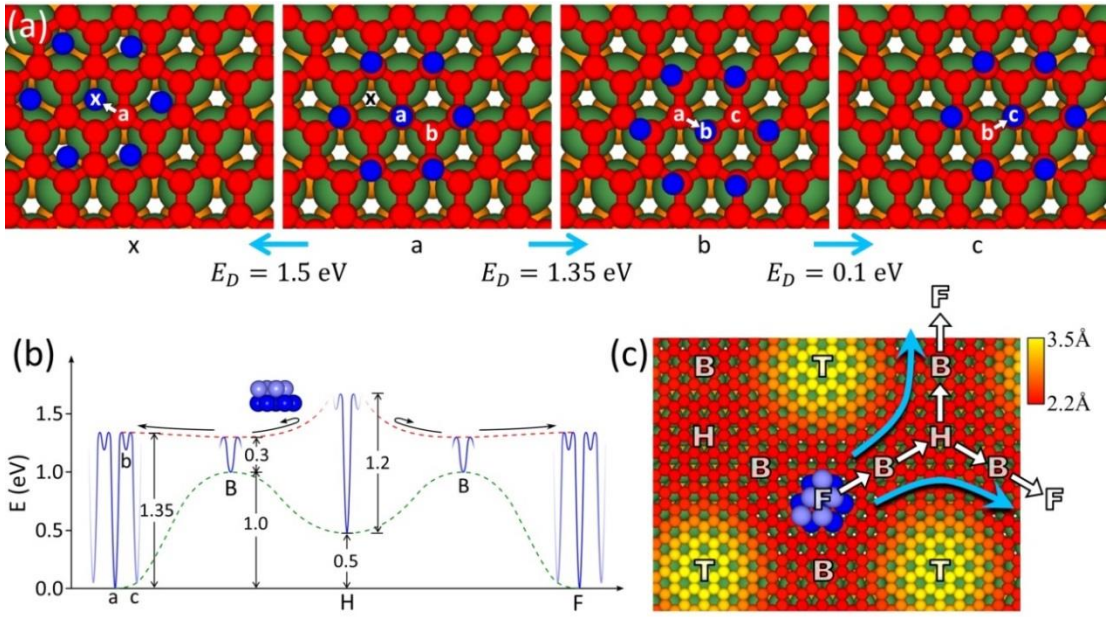

Figure 46. Theory results on the diffusion path of a mobile, low footprint (2-layer) Pd_{12} isomer on graphene/Ru(0001). Displacement of the cluster with the center of mass (com) moving along the C-C bond (see a → b) requires a smaller activation energy barrier than motion of the com in the direction of the center of the honeycomb ring (a → x). In the calculated diffusion path (a → b → c) with the lowest activation barrier, the first step out of the F adsorption site (a → b) requires a much larger activation energy than the subsequent step (b → c). The following diffusion steps (in the direction of the B-site region) require successively smaller activation energies. (b) Schematic energy-surface diagram that summarizes the results of the calculations, displaying the relative values of the binding energies of the cluster to the surface (relative to the F site taken as the zero of the energy scale), the respective calculated outward diffusion barriers from the F, B and H sites (with a,b, and c marked in the F region, on the left, corresponding to the path a-b-c in panel (a)), and the range of upper and lower bounds for the variation along the diffusion path of the interaction energy of the cluster with the surface. Note the relatively high energy barrier (~0.4 eV) inhibiting diffusion of the cluster into the H region, while the highest local barrier for diffusion out of an adsorption site is found for the F site. These activation barriers lead to almost exclusive population of F sites under the investigated conditions. (c) Part of the Moiré formed by the graphene layer on the Ru(0001) with the 2-layer Pd_{12} cluster adsorbed at the F site; the color scale in the upper right gives the distance of the carbon atom from the topmost layer of the underlying metal surface. Superimposed we show the most probable diffusion paths (blue arrows) of the cluster between adjacent F sites (see panel (a,b)), constructed from the results of the first-principles calculations. The first-principles calculations and the set of the figure have been performed by the coauthors of the cited publication, B. Yoon and U. Landman. Reprinted (adapted) with permission from [24b]. Copyright 2015 American Chemical Society.

The kinetic energy has to be dissipated efficiently in this case. When driving away from the strong binding sites the cluster no longer gets caught by sites where it can dissipate and accelerates, in analogy with a former study that was performed on gr/Ru(0001).[24b]

Fig. 46, taken from this study, shows the relation between the diffusion path and the activation barrier for each displacement step. The figure has been drawn using first-principles calculations. The results from this study cannot be adopted one to one to our measurement as they are related to two analogous but though different supports. The main difference is the total energy differences of the clusters being adsorbed in the ring-fcc site versus the ring-hcp site. On graphene on Rh(111) this difference seems to be rather small as the clusters bind in the two positions in the Moiré cell in equal shares. It is important to note that the cluster can also bind strongly in the neighbored position on the C_6 ring; therefore also small displacements in the order of a carbon-carbon distance are possible (see Fig. 48).

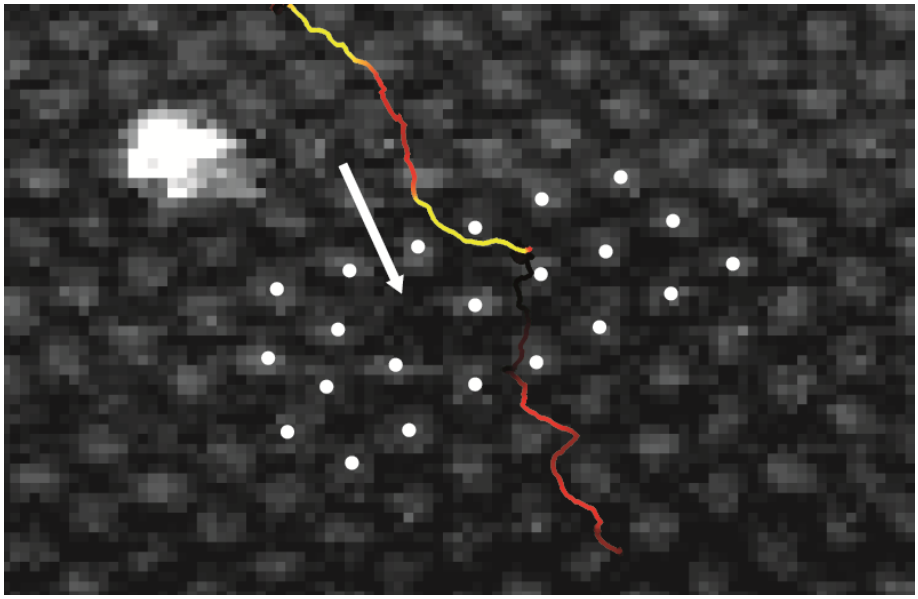

Figure 47. Zoom-in of Fig. 44, displaying the velocity colored track of the cluster over the graphene surface. The neighbored ring-top sites are marked by white dots, whereas the visible defect zone is marked by an arrow.

The high lateral displacement of the cluster after the first stop is probably due to the neighboring defect in the graphene layer, which can be seen by the irregular constitution of the Moiré cells, displayed in a zoom-in in Fig. 47.

In order to get a more detailed view of the adsorption process in the resting positions, a zoom-in of the cluster's track around the resting position 1 is displayed in Fig. 48. The cluster approaches the adsorption site, which is supposed to be a ring-hollow site on the substrate, from the lower left corner whereupon its movement comes nearly to a rest.

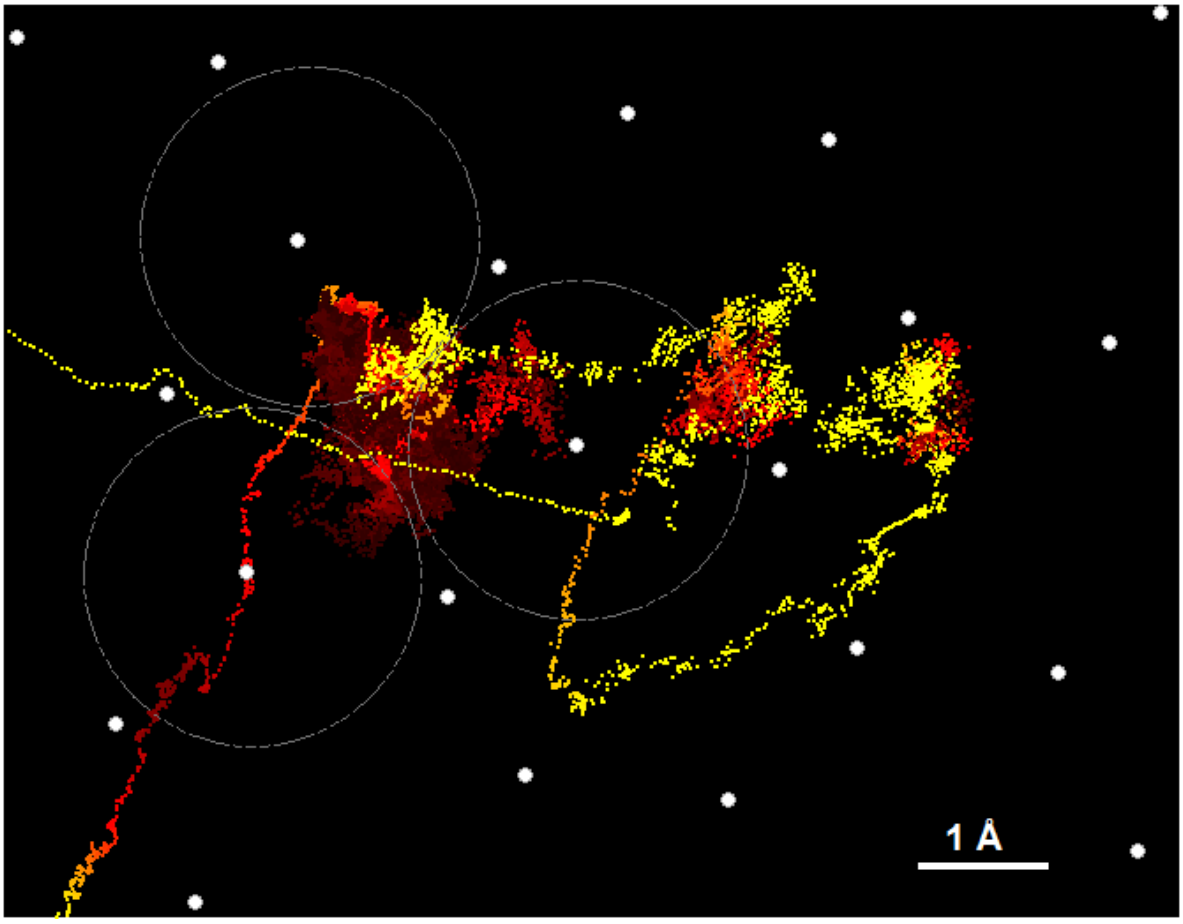

Figure 48. Zoom-in of the cluster track in the resting zone 1. The track is color-coded with the lateral velocity. The cluster, coming from the lower left corner, approaches the ring-hollow site marked by three schematic Rh atoms. To guide the eye the white dots represent the carbon atoms of the graphene layer. After a long waiting time in the ring-hollow site, the clusters starts a slow movement in the proximity before enhancing abruptly its velocity and rushing away to the left of the zoom-in.

After some time the cluster starts a slow movement in the proximity of the ring-hollow site, which is marked by three schematic Rhodium atoms. The carbon ring, represented by white dots, is centered over these three atoms. In these carbon hexagons the cluster resides for a longer time. Suddenly the cluster takes up velocity in a position off-center and the track shows a fast movement of the cluster to the left, which starts the diffusion step that will end up in the resting position 2. It seems that the cluster explores the surrounding binding sites in the same way as anticipated by the simulation and once the cluster has accelerated, it has no chance to get caught by the ring-hollow site again, not even if flying right over it, because there is no time to dissipate the obtained kinetic energy.

Discussion

In this section a technique for time resolved STM was presented: The Atom Tracking technique was first described theoretically and its evolution through the last 20 years was depicted. A major part of the workload lay on the implementation of the technique into our STM system. This implementation turned out to be time expensive due to the setup from scratch that was required in order to find a solution that could be fully controlled by us. Hardware just like the software were developed in-house and required a set of control parameters that had to be determined for the specific cluster diffusion problem.

Finally, the first experiments using the Atom Tracking technique showed the power and the accuracy of this method. Clusters or other protrusions on the surface can be tracked with a time resolution of 10 ms. The coordinates of mobile clusters could be recorded with an accuracy below one angstrom and together with the information in the vertical direction a complete picture of the clusters' movement could be drawn. The experiment could be driven for long times and could cover large distances (up to 100 nm).

Nevertheless the statistics are still rather limited. Up to now, only a few clusters could be tracked and the reasons for that are mainly attributed to the low diffusion probability of the observed clusters. A long range ordered support, namely graphene on Rh(111), was used, which had to be free of defects and have domain boundaries of over hundreds of nanometers. The low cluster coverage, essential for the observation of collision-free diffusion events, made it difficult to catch diffusing clusters. Experiments at elevated temperatures were not yet successful, since thermal drift has to be controlled in a more efficient way and since diffusing contaminations blocked the cluster tracking control. AT measurements at elevated temperatures could nevertheless be fruitful with tracking parameters that hold the tip on the cluster and not be distracted by smaller diffusing

particles. To enlarge the amplitude of the circular movement could be the key parameter in this case.

The movements that were observed for the clusters differ from classical atomic diffusion or the movement of silicon dimers on Si(111) as observed by Swartzentruber.[58] He observed defined hops or jumps between adjacent adsorption sites. These jumps happen 2-dimensionnally and randomly but more often than our cluster movements. This is why for the case of silicon dimers distinct hop statistics can be made and the activation energy for a jump can be calculated through an Arrhenius plot. In the case of clusters on graphene, the situation is more complicated. The cluster can move in each of the directions on the surface and the interaction of the cluster and the support is not limited to adjacent adsorption sites but is subject to a complex interplay due to the periodically wettability of the graphene. The cluster not simply jump from one ring-hcp or ring-fcc binding site to a neighbored one, but perform a complex movement with periods of acceleration and deceleration, and long diffusion events over some ten Moiré cells before coming to a rest. We observe that metal clusters on graphene can display a Lévy flight-type displacement over large distances, while still being caught by distinct adsorption sites on the graphene support. The interplay of the cluster's movement with the periodically wettable graphene support, as well in the horizontal as in the vertical direction, can be shown by the Atom Tracking measurements. Small movements around wettable resting positions seem to follow the results anticipated by DFT calculations.

In order to improve the statistics of mobile clusters, the quality of the graphene layer is of uttermost importance. Mobile clusters on poor quality graphene are caught by defects that exhibit additional, stronger adsorption places to the clusters. A fact that was

illustrated by a tracked cluster that hopped between two adsorption places within a potential well in the graphene sheet.

In the view of future experiments, other cluster sizes should be checked on the same support as well as on supports that differ by the clusters' adsorption properties. The difference in the adsorption environment should also have effects on the diffusion pattern of the moving clusters. Especially the beginning and end of each movement step is of high interest, as more insight into this step could provide detailed information of the local diffusion of the cluster and the cluster's binding properties to the support underneath. In order to get this kind of information, the definition of the cluster's position has to be even more accurate and the tracking properties should be optimized in view of such an investigation.

Conclusion and Outlook

In the first chapter I reported on size-selected and soft-landed Pd clusters that were investigated by conventional STM of the monodisperse cluster distributions. The evolution of the PSD upon subsequent annealing steps allowed insight into the competing cluster ripening mechanisms. The study was performed on three different substrates: a bare metallic Rh(111) surface, graphene Moiré films on Rh(111) and Ru(0001) surfaces, as well as a hexagonal boron nitride Moiré on Rh(111). These substrates differ in their long-range order as well as in their atom and cluster adsorption strength. On the bare metal surface as well as on h-BN/Rh(111), the Pd clusters grow exclusively by Ostwald ripening due to the stronger binding of the cluster to the substrate. On epitaxial graphene, in contrast, the clusters ripen by Smoluchowski ripening up to 600 K, and only then a crossover to Ostwald ripening sets in.

Important insights into the structural and energetic factors that govern the operative atomic-scale processes of mass-transport and ripening mechanisms could be understood on the basis of first-principles DFT calculations. These calculations explored the nature and strength of the cluster bonding to the surfaces, dependencies on the supporting surface and the structure of the adsorbed cluster, as well as the energies of atom and dimer detachment from adsorbed clusters. The combined experimental and theoretical investigations allowed to relate the differences in the ripening behavior to distinct properties of the different substrates: The periodical wettability and the different binding strenght at the cluster adsorption sites suggest a strategy aimed at optimizing the stability of surface-supported clusters against ripening. Accordingly, one can conclude that in attempting to control particle coarsening on surfaces, one must optimize both, the binding of the entire adsorbed clusters to the substrate - playing a key role in the cluster

migration/coalescence processes, termed here the Smoluchowski ripening mechanism - , as well as the interactions of single atoms or very small clusters serving as mass-transport species in the Ostwald ripening mechanism. Such circumstances may be realized by suitable choice of surfaces with laterally modulated wettability. On such surfaces, stronger binding of the adsorbed metal clusters to particular sites (wettable areas) anchors them locally, while the relatively weak interaction of single metal atoms with non-wettable regions of the substrate blocks interparticle exchange of matter and limits the preferential residence to the wettable areas that act as attractive catchment basins. This study shows that surfaces with modulated wettability, that is graphene- and hexagonal boron nitride-Moiré films grown on late transition metal surfaces, such as Rh(111) and Ru(0001), can be employed as useful model systems for control of adsorbed particle coarsening. The information gained in this investigation provides the impetus for further development of stable effective nanocatalytic systems and investigations of their stability and catalytic properties through the use of surface-supported size-selected clusters.[67]

The second chapter of this thesis deals with the implementation of an Atom Tracking technique and its application to small clusters that diffuse already at RT on a periodically wettable substrate, namely size-selected Pd_{12} clusters soft-landed on graphene/Rh(111). It could be demonstrated that the path taken by the diffusing clusters is related to the geometric and electronic properties of the graphene superstructure, e.g. by avoiding the ring-top sites. The technique could be implemented in such a way as to facilitate the use for a general community. The hierarchical implementation steps are explained in detail and test experiments, which investigate the influence of the voltage bias and CO gas dosing on the measurement, are described.

Two cases demonstrate that the diffusion of clusters can be traced by AT; the termination is not given by technical limits, but is due to characteristic defects and coalescence events that can each time be elucidated by post-tracking STM images. By relating the mean square displacement to the time interval of the movement, a diffusion coefficient as well as the parameter for anomalous diffusion could be calculated. The movement points to be anomalous and is related to Lévy flights, where large displacement step lengths and long waiting times in the adsorption position are possible, in contrast to a classical random walk.

This thesis established a method in our laboratory and elucidates possible investigations with AT in the future. Once the conditions are optimized for driving AT at higher temperatures, temperature dependent measurements of a cluster's diffusion could give insights into the kinetics of the cluster-substrate system and their related thermodynamic parameter. Comparable to the work of Swartzentruber, an Arrhenius plot combining measurement for different temperatures could provide the activation energy for such a diffusion step.[58] Furthermore the conventional transition state theory allows for determining the prefactor of the diffusion rate expression, which is related to the floppiness of the adsorbed cluster, and the entropy of activation, which gives insights into the configurations of the transition state.[68]

Beside of looking at the cluster's diffusion from cell to cell, also the diffusion within the Moiré cell seems to be promising. If a cluster can be found that can reach by thermal activation over a sufficient measurement interval all the positions in the Moiré cell (ergodic behavior), a potential energy surface of the graphene Moiré could be drawn, based on the population histograms. Furthermore, by linking the lateral and vertical information that can be obtained by AT with high precision, the diffusion of clusters with different sizes

can be compared. Here it will be interesting to know if clusters with open and closed shells diffuse differently, e.g. due to different peripheral diffusion of cluster atoms that mediates fluctuations of the clusters' center of mass. Thus AT is highly promising for shedding light on the interaction of noble metal clusters and their respective supports.

References

[1] Y. Fukamori, M. Konig, B. Yoon, B. Wang, F. Esch, U. Heiz, U. Landman, *ChemCatChem* **2013**, *5*, 3330-3341.

[2] U. Heiz, F. Vanolli, L. Trento, W. D. Schneider, *Rev. Sci. Instrum.* **1997**, *68*, 1986-1994.

[3] a) M. Sicot, S. Bouvron, O. Zander, U. Rudiger, Y. S. Dedkov, M. Fonin, *Appl. Phys. Lett.* **2010**, *96,* 093115;
b) B. Wang, M. Caffio, C. Bromley, H. Fruchtl, R. Schaub, *ACS Nano* **2010**, *4*, 5773-5782.

[4] a) S. Berner, M. Corso, R. Widmer, O. Groening, R. Laskowski, P. Blaha, K. Schwarz, A. Goriachko, H. Over, S. Gsell, M. Schreck, H. Sachdev, T. Greber, J. Osterwalder, *Angew. Chem. Int. Edit.* **2007**, *46*, 5115-5119;
b) R. Laskowski, P. Blaha, T. Gallauner, K. Schwarz, *Phys. Rev. Lett.* **2007**, *98,* 106802.

[5] a) G. Binnig, H. Rohrer, C. Gerber, E. Weibel, *Appl. Phys. Lett.* **1982**, *40*, 178-180;
b) G. Binnig, H. Rohrer, C. Gerber, E. Weibel, *Phys. Rev. Lett.* **1983**, *50*, 120-123.

[6] C. J. Chen, *Introduction to scanning tunneling microscopy*, Oxford University Press, New York, **1993**.

[7] a) R. Wiesendanger, Cambridge University Press, Cambridge, **1994**;
b) H. J. W. Zandvliet, A. van Houselt, *Annu. Rev. Anal. Chem.* **2009**, *2*, 37-55.

[8] a) L. Grill, F. Moresco, P. Jiang, C. Joachim, A. Gourdon, K. H. Rieder, *Phys. Rev. B* **2004**, *69,* 035416;
b) L. Grill, F. Moresco, *J. Phys. Condens. Mat.* **2006**, *18*, S1887-S1908.

[9] C. H. Bartholomew, *Appl. Catal. A* **2001**, *212*, 17-60.

[10] J. R. Rostrup-Nielsen, *Catalysis Today* **1993**, *18*, 125-145.

[11] a) H. L. Xin, J. A. Mundy, Z. Y. Liu, R. Cabezas, R. Hovden, L. F. Kourkoutis, J. L. Zhang, N. P. Subramanian, R. Makharia, F. T. Wagner, D. A. Muller, *Nano Lett.* **2012**, *12*, 490-497;
b) M. A. Newton, C. Belver-Coldeira, A. Martinez-Arias, M. Fernandez-Garcia, *Nat. Mater.* **2007**, *6*, 528-532.

[12] D. W. Goodman, *Surf. Rev. Lett.* **1995**, *2*, 9-24.

[13] W. Ostwald, *Zeitschrift für Physikalische Chemie* **1900**, *34*, 495-503.

[14] M. v. Smoluchowski, *Physikalische Zeitschrift* **1916**, *17*, 557-571, 585-599.

[15] a) M. J. J. Jak, C. Konstapel, A. van Kreuningen, J. Verhoeven, J. W. M. Frenken, *Surf. Sci.* **2000**, *457*, 295-310;
b) T. W. Hansen, PhD Thesis, Technical University of Denmark **2006**.

[16] a) I. M. Lifshitz, V. V. Slyozov, *J. Phys. Chem. Solids* **1961**, *19*, 35-50;
b) C. Wagner, *Zeitschrift für Elektrochemie* **1961**, *65*, 581-591;
c) M. Kahlweit, *Adv. Colloid. Interfac.* **1975**, *5*, 1-35.

[17] B. K. Chakraverty, *J. Phys. Chem. Solids* **1967**, *28*, 2401-2412.

[18] R. Finsy, *Langmuir* **2004**, *20*, 2975-2976.

[19] a) C. G. Granqvist, R. A. Buhrman, *Appl. Phys. Lett.* **1975**, *27*, 693-694;
b) C. G. Granqvist, R. A. Buhrman, *J. Catal.* **1976**, *42*, 477-479.

[20] P. G. Wynblatt, N.A., *Progress in solid state chemistry* **1975**, *9*, 21-58.

[21] A. K. Datye, Q. Xu, K. C. Kharas, J. M. McCarty, *Catalysis Today* **2006**, *111*, 59-67.

[22] S. B. Simonsen, I. Chorkendorff, S. Dahl, M. Skoglundh, J. Sehested, S. Helveg, *J. Am. Chem. Soc.* **2010**, *132*, 7968-7975.

[23] K. Morgenstern, G. Rosenfeld, G. Comsa, *Surf. Sci.* **1999**, *441*, 289-300.

[24] a) B. Wang, M. L. Bocquet, *J. Phys. Chem. Lett.* **2011**, *2*, 2341-2345;
b) B. Wang, B. Yoon, M. Konig, Y. Fukamori, F. Esch, U. Heiz, U. Landman, *Nano Lett.* **2012**, *12*, 5907-5912.

[25] G. Kresse, D. Joubert, *Phys. Rev. B* **1999**, *59*, 1758-1775.

[26] a) J. P. Perdew, in *Electronic Structure of Solids'91* (Eds.: P. Ziesche, H. Eschring), Akademie, Berlin, **1991**;
b) J. P. Perdew, J. A. Chevary, S. H. Vosko, K. A. Jackson, M. R. Pederson, D. J. Singh, C. Fiolhais, *Phys. Rev. B* **1992**, *46*, 6671-6687;
c) J. P. Perdew, J. A. Chevary, S. H. Vosko, K. A. Jackson, M. R. Pederson, D. J. Singh, C. Fiolhais, *Phys. Rev. B* **1993**, *48*, 4978-4978.

[27] G. Rosenfeld, K. Morgenstern, M. Esser, G. Comsa, *Appl. Phys. A-Mater.* **1999**, *69*, 489-496.

[28] a) G. Rosenfeld, A. F. Becker, B. Poelsema, L. K. Verheij, G. Comsa, *Phys. Rev. Lett.* **1992**, *69*, 917-920;
b) C. Massobrio, P. Blandin, *Phys. Rev. B* **1993**, *47*, 13687-13695.

[29] T. Michely, M. Hohage, M. Bott, G. Comsa, *Phys. Rev. Lett.* **1993**, *70*, 3943-3946.

[30] J. Knudsen, P. J. Feibelman, T. Gerber, E. Granas, K. Schulte, P. Stratmann, J. N. Andersen, T. Michely, *Phys. Rev. B* **2012**, *85,* 035407.

[31] M. König, PhD Thesis, Technische Universität München **2015**.

[32] J. Weitkamp, R. Gläser, (Eds.: R. Dittmeyer, W. Keim, G. Kreysa, A. Oberholz), Wiley-VCH, Weinheim, **2004**.

[33] O. Bunk, M. Corso, D. Martoccia, R. Herger, P. R. Willmott, B. D. Patterson, J. Osterwalder, I. van der Veen, T. Greber, *Surf. Sci.* **2007**, *601*, L7-L10.

[34] a) H. Dil, J. Lobo-Checa, R. Laskowski, P. Blaha, S. Berner, J. Osterwalder, T. Greber, *Science* **2008**, *319*, 1824-1826;
b) A. Goriachko, Y. B. He, H. Over, *J. Phys. Chem. C* **2008**, *112*, 8147-8152.

[35] D. E. Sanders, A. E. Depristo, *Surf. Sci.* **1992**, *264*, L169-L176.

[36] T. Gerber, J. Knudsen, P. J. Feibelman, E. Granas, P. Stratmann, K. Schulte, J. N. Andersen, T. Michely, *ACS Nano* **2013,** *7*, 2020-2031.

[37] a) S. Kunz, F. F. Schweinberger, V. Habibpour, M. Rottgen, C. Harding, M. Arenz, U. Heiz, *J. Phys. Chem. C* **2010**, *114*, 1651-1654;
b) T. Engel, G. Ertl, *J. Chem. Phys.* **1978**, *69*, 1267-1281.

[38] M. Di Vece, D. Grandjean, M. J. Van Bael, C. P. Romero, X. Wang, S. Decoster, A. Vantomme, P. Lievens, *Phys. Rev. Lett.* **2008**, *100,* 236105.

[39] N. V. S. Piskunov, Y.T.; Kulgavchuk, V.M.; Protopopov, N.A., *J. Eng. Phys. Thermophys.* **2001**, *74*, 1217-1220.

[40] A. Fick, *Annalen der Physik* **1855**, *170*, 59-86.

[41] a) A. Einstein, *Annalen der Physik* **1905**, *17*, 549-560;
b) A. Einstein, *Annalen der Physik* **1906**, *19*, 371-381;
c) A. Einstein, *Annalen der Physik* **1906**, *19*, 289-306.

[42] M. v. Smoluchowski, *Annalen der Physik* **1906**, *21*, 756-780.

[43] a) J. Ingen-Housz, in *Nouvelles expériences et observations sur divers objets de physique, Vol. 2*, Theophile Barrois, Paris, **1789**, pp. 1-5;
b) R. Brown, *Edinburgh new Philosophical Journal* **1828**, *5*, 358-371.

[44] a) H. Brune, *Surf. Sci. Rep.* **1998**, *31*, 121-229;
b) J. V. Barth, *Surf. Sci. Rep.* **2000**, *40*, 75-149;
c) K. L. Oura, V.G.; Saranin, A.; Zotov, A.V.; Katayama, M., *Surface Science*, Springer, Berlin, **2003**.

[45] a) M. F. Shlesinger, G. M. Zaslavsky, J. Klafter, *Nature* **1993**, *363*, 31-37;
b)M. F. Shlesinger, J. Klafter, G. Zumofen, *Am. J. Phys.* **1999**, *67*, 1253-1259.

[46] H. Scher, E. W. Montroll, *Phys. Rev. B* **1975**, *12*, 2455-2477.

[47] a) M. Weiss, M. Elsner, F. Kartberg, T. Nilsson, *Biophys. J.* **2004**, *87*, 3518-3524;
b) J. Klafter, I. M. Sokolov, *Phys. World* **2005**, *18*, 29-32.

[48] D. Brockmann, L. Hufnagel, T. Geisel, *Nature* **2006**, *439*, 462-465.

[49] a) N. E. Humphries, N. Queiroz, J. R. M. Dyer, N. G. Pade, M. K. Musyl, K. M. Schaefer, D. W. Fuller, J. M. Brunnschweiler, T. K. Doyle, J. D. R. Houghton, G. C. Hays, C. S. Jones, L. R. Noble, V. J. Wearmouth, E. J. Southall, D. W. Sims, *Nature* **2010**, *465*, 1066-1069;

b) A. M. Edwards, R. A. Phillips, N. W. Watkins, M. P. Freeman, E. J. Murphy, V. Afanasyev, S. V. Buldyrev, M. G. E. da Luz, E. P. Raposo, H. E. Stanley, G. M. Viswanathan, *Nature* **2007**, *449*, 1044-U1045.

[50] W. D. Luedtke, U. Landman, *Phys. Rev. Lett.* **1999**, *82*, 3835-3838.

[51] B. C. Stipe, M. A. Rezaei, W. Ho, *Phys. Rev. Lett.* **1998**, *81*, 1263-1266.

[52] A. E. Baber, H. L. Tierney, E. C. H. Sykes, *ACS Nano* **2008**, *2*, 2385-2391.

[53] W. Auwarter, K. Seufert, F. Bischoff, D. Ecija, S. Vijayaraghavan, S. Joshi, F. Klappenberger, N. Samudrala, J. V. Barth, *Nat. Nanotechnoly* **2012**, *7*, 41-46.

[54] a) F. Besenbacher, E. Laegsgaard, I. Stensgaard, *Mater Today* **2005**, *8*, 26-30;
b) T. R. Linderoth, S. Horch, E. Laegsgaard, I. Stensgaard, F. Besenbacher, *Phys. Rev. Lett.* **1997**, *78*, 4978-4981;
c) E. Laegsgaard, L. Osterlund, P. Thostrup, P. B. Rasmussen, I. Stensgaard, F. Besenbacher, *Rev. Sci. Instrum.* **2001**, *72*, 3537-3542;
d) M. J. Rost, L. Crama, P. Schakel, E. van Tol, G. B. E. M. van Velzen-Williams, C. F. Overgauw, H. ter Horst, H. Dekker, B. Okhuijsen, M. Seynen, A. Vijftigschild, P. Han, A. J. Katan, K. Schoots, R. Schumm, W. van Loo, T. H. Oosterkamp, J. W. M. Frenken, *Rev. Sci. Instrum.* **2005**, *76,* 053710.

[55] F. Esch, C. Dri, A. Spessot, C. Africh, G. Cautero, D. Giuressi, R. Sergo, R. Tommasini, G. Comelli, *Rev. Sci. Instrum.* **2011**, *82,* 053702.

[56] J. Wintterlin, J. Trost, S. Renisch, R. Schuster, T. Zambelli, G. Ertl, *Surf. Sci.* **1997**, *394*, 159-169.

[57] D. W. Pohl, R. Moller, *Rev. Sci. Instrum.* **1988**, *59*, 840-842.

[58] B. S. Swartzentruber, *Phys. Rev. Lett.* **1996**, *76*, 459-462.

[59] J. M. Carpinelli, B. S. Swartzentruber, *Phys. Rev. B* **1998**, *58*, 13423-13425.

[60] M. Abe, Y. Sugimoto, O. Custance, S. Morita, *Nanotechnology* **2005**, *16*, 3029-3034.

[61] P. Rahe, J. Schutte, W. Schniederberend, M. Reichling, M. Abe, Y. Sugimoto, A. Kuhnle, *Rev. Sci. Instrum.* **2011**, *82,* 073703.

[62] J. A. Lissajous, in *Annales de Chimie et de Physique* (Ed.: Mallet-Bachelier), Paris, **1857**.

[63] G. S. Parkinson, Z. Novotny, G. Argentero, M. Schmid, J. Pavelec, R. Kosak, P. Blaha, U. Diebold, *Nat. Mater.* **2013**, *12*, 724-728.

[64] a) J. A. Stroscio, D. M. Eigler, *Science* **1991**, *254*, 1319-1326;
b) Y. W. Mo, *Science* **1993**, *261*, 886-888;
c) T. C. Shen, C. Wang, G. C. Abeln, J. R. Tucker, J. W. Lyding, P. Avouris, R. E. Walkup, *Science* **1995**, *268*, 1590-1592.

[65] E. N. Voloshina, Y. S. Dedkov, S. Torbrugge, A. Thissen, M. Fonin, *Appl. Phys. Lett.* **2012**, *100,* 241606.

[66] B. A. J. Lechner, A. S. de Wijn, H. Hedgeland, A. P. Jardine, B. J. Hinch, W. Allison, J. Ellis, *J. Chem. Phys.* **2013**, *138,* 194710.

[67] a) A. Sanchez, S. Abbet, U. Heiz, W. D. Schneider, H. Hakkinen, R. N. Barnett, U. Landman, *J. Phys. Chem. A* **1999**, *103*, 9573-9578;
b) U. Landman, B. Yoon, C. Zhang, U. Heiz, M. Arenz, *Top. Catal.* **2007**, *44*, 145-158.

[68] K. W. Kolasinski, *Surface Science: Foundations of Catalysis and Nanoscience*, Wiley, **2012**.

Reprint permissions

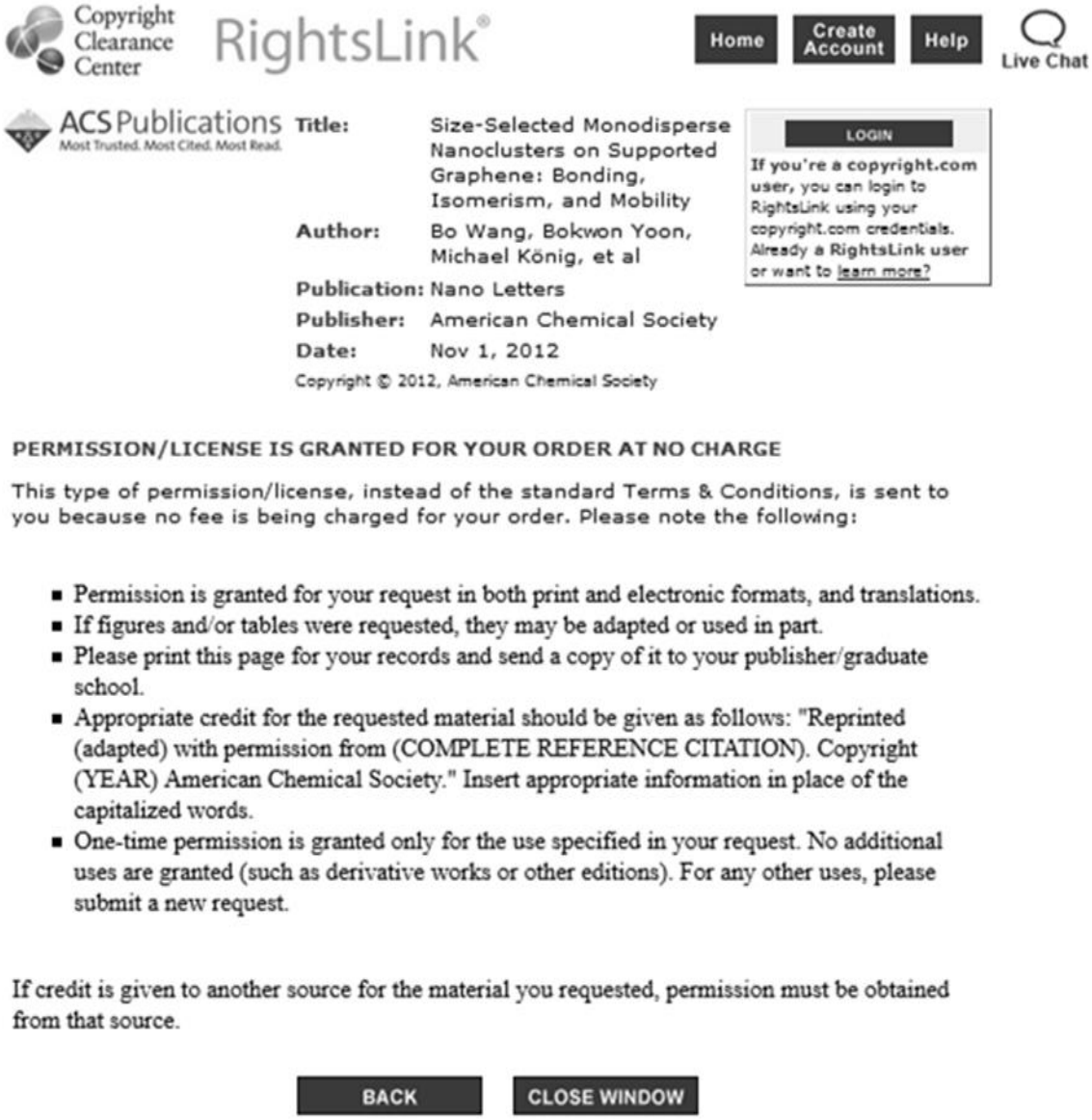

Copyright Clearance Center RightsLink®

Home | Create Account | Help | Live Chat

ACS Publications
Most Trusted. Most Cited. Most Read.

Title: Size-Selected Monodisperse Nanoclusters on Supported Graphene: Bonding, Isomerism, and Mobility

Author: Bo Wang, Bokwon Yoon, Michael König, et al

Publication: Nano Letters

Publisher: American Chemical Society

Date: Nov 1, 2012

Copyright © 2012, American Chemical Society

LOGIN

If you're a copyright.com user, you can login to RightsLink using your copyright.com credentials. Already a RightsLink user or want to learn more?

PERMISSION/LICENSE IS GRANTED FOR YOUR ORDER AT NO CHARGE

This type of permission/license, instead of the standard Terms & Conditions, is sent to you because no fee is being charged for your order. Please note the following:

- Permission is granted for your request in both print and electronic formats, and translations.
- If figures and/or tables were requested, they may be adapted or used in part.
- Please print this page for your records and send a copy of it to your publisher/graduate school.
- Appropriate credit for the requested material should be given as follows: "Reprinted (adapted) with permission from (COMPLETE REFERENCE CITATION). Copyright (YEAR) American Chemical Society." Insert appropriate information in place of the capitalized words.
- One-time permission is granted only for the use specified in your request. No additional uses are granted (such as derivative works or other editions). For any other uses, please submit a new request.

If credit is given to another source for the material you requested, permission must be obtained from that source.

BACK | CLOSE WINDOW

Copyright © 2015 Copyright Clearance Center, Inc. All Rights Reserved. Privacy statement. Terms and Conditions.
Comments? We would like to hear from you. E-mail us at customercare@copyright.com

JOHN WILEY AND SONS LICENSE TERMS AND CONDITIONS

Nov 22, 2015

This Agreement between Yves Fukamori ("You") and John Wiley and Sons ("John Wiley and Sons") consists of your license details and the terms and conditions provided by John Wiley and Sons and Copyright Clearance Center.

License Number	3754200486648
License date	Nov 22, 2015
Licensed Content Publisher	John Wiley and Sons
Licensed Content Publication	ChemCatChem
Licensed Content Title	Fundamental Insight into the Substrate-Dependent Ripening of Monodisperse Clusters
Licensed Content Author	Yves Fukamori,Michael König,Bokwon Yoon,Bo Wang,Friedrich Esch,Ueli Heiz,Uzi Landman
Licensed Content Date	Aug 13, 2013
Pages	12
Type of use	Dissertation/Thesis
Requestor type	Author of this Wiley article
Format	Print and electronic
Portion	Full article
Will you be translating?	No
Title of your thesis / dissertation	Static and dynamic characterization of size-selected cluster diffusion and ripening on periodically wettable surfaces
Expected completion date	Nov 2015
Expected size (number of pages)	120
Requestor Location	Yves Fukamori Lichtenbergstraße 4 Garching, Germany 85748 Attn: Yves Fukamori
Billing Type	Invoice
Billing Address	Yves Fukamori Lichtenbergstraße 4 Garching, Germany 85748 Attn: Yves Fukamori
Total	0.00 EUR
Terms and Conditions	

TERMS AND CONDITIONS

This copyrighted material is owned by or exclusively licensed to John Wiley & Sons, Inc. or one of its group companies (each a"Wiley Company") or handled on behalf of a society with which a Wiley Company has exclusive publishing rights in relation to a particular work (collectively "WILEY"). By clicking "accept" in connection with completing this licensing

transaction, you agree that the following terms and conditions apply to this transaction (along with the billing and payment terms and conditions established by the Copyright Clearance Center Inc., ("CCC's Billing and Payment terms and conditions"), at the time that you opened your RightsLink account (these are available at any time at http://myaccount.copyright.com).

Terms and Conditions

- The materials you have requested permission to reproduce or reuse (the "Wiley Materials") are protected by copyright.

- You are hereby granted a personal, non-exclusive, non-sub licensable (on a stand-alone basis), non-transferable, worldwide, limited license to reproduce the Wiley Materials for the purpose specified in the licensing process. This license, **and any CONTENT (PDF or image file) purchased as part of your order,** is for a one-time use only and limited to any maximum distribution number specified in the license. The first instance of republication or reuse granted by this license must be completed within two years of the date of the grant of this license (although copies prepared before the end date may be distributed thereafter). The Wiley Materials shall not be used in any other manner or for any other purpose, beyond what is granted in the license. Permission is granted subject to an appropriate acknowledgement given to the author, title of the material/book/journal and the publisher. You shall also duplicate the copyright notice that appears in the Wiley publication in your use of the Wiley Material. Permission is also granted on the understanding that nowhere in the text is a previously published source acknowledged for all or part of this Wiley Material. Any third party content is expressly excluded from this permission.

- With respect to the Wiley Materials, all rights are reserved. Except as expressly granted by the terms of the license, no part of the Wiley Materials may be copied, modified, adapted (except for minor reformatting required by the new Publication), translated, reproduced, transferred or distributed, in any form or by any means, and no derivative works may be made based on the Wiley Materials without the prior permission of the respective copyright owner.**For STM Signatory Publishers clearing permission under the terms of the STM Permissions Guidelines only, the terms of the license are extended to include subsequent editions and for editions in other languages, provided such editions are for the work as a whole in situ and does not involve the separate exploitation of the permitted figures or extracts,** You may not alter, remove or suppress in any manner any copyright, trademark or other notices displayed by the Wiley Materials. You may not license, rent, sell, loan, lease, pledge, offer as security, transfer or assign the Wiley Materials on a stand-alone basis, or any of the rights granted to you hereunder to any other person.

- The Wiley Materials and all of the intellectual property rights therein shall at all times remain the exclusive property of John Wiley & Sons Inc, the Wiley Companies, or their respective licensors, and your interest therein is only that of having possession of and the right to reproduce the Wiley Materials pursuant to Section 2 herein during the continuance of this Agreement. You agree that you own no right, title or interest in or to the Wiley Materials or any of the intellectual property rights therein. You shall have no rights hereunder other than the license as provided for above in Section 2. No right, license or interest to any trademark, trade name, service mark or other branding ("Marks") of WILEY or its licensors is granted hereunder, and you agree that you

shall not assert any such right, license or interest with respect thereto

- NEITHER WILEY NOR ITS LICENSORS MAKES ANY WARRANTY OR REPRESENTATION OF ANY KIND TO YOU OR ANY THIRD PARTY, EXPRESS, IMPLIED OR STATUTORY, WITH RESPECT TO THE MATERIALS OR THE ACCURACY OF ANY INFORMATION CONTAINED IN THE MATERIALS, INCLUDING, WITHOUT LIMITATION, ANY IMPLIED WARRANTY OF MERCHANTABILITY, ACCURACY, SATISFACTORY QUALITY, FITNESS FOR A PARTICULAR PURPOSE, USABILITY, INTEGRATION OR NON-INFRINGEMENT AND ALL SUCH WARRANTIES ARE HEREBY EXCLUDED BY WILEY AND ITS LICENSORS AND WAIVED BY YOU.

- WILEY shall have the right to terminate this Agreement immediately upon breach of this Agreement by you.

- You shall indemnify, defend and hold harmless WILEY, its Licensors and their respective directors, officers, agents and employees, from and against any actual or threatened claims, demands, causes of action or proceedings arising from any breach of this Agreement by you.

- IN NO EVENT SHALL WILEY OR ITS LICENSORS BE LIABLE TO YOU OR ANY OTHER PARTY OR ANY OTHER PERSON OR ENTITY FOR ANY SPECIAL, CONSEQUENTIAL, INCIDENTAL, INDIRECT, EXEMPLARY OR PUNITIVE DAMAGES, HOWEVER CAUSED, ARISING OUT OF OR IN CONNECTION WITH THE DOWNLOADING, PROVISIONING, VIEWING OR USE OF THE MATERIALS REGARDLESS OF THE FORM OF ACTION, WHETHER FOR BREACH OF CONTRACT, BREACH OF WARRANTY, TORT, NEGLIGENCE, INFRINGEMENT OR OTHERWISE (INCLUDING, WITHOUT LIMITATION, DAMAGES BASED ON LOSS OF PROFITS, DATA, FILES, USE, BUSINESS OPPORTUNITY OR CLAIMS OF THIRD PARTIES), AND WHETHER OR NOT THE PARTY HAS BEEN ADVISED OF THE POSSIBILITY OF SUCH DAMAGES. THIS LIMITATION SHALL APPLY NOTWITHSTANDING ANY FAILURE OF ESSENTIAL PURPOSE OF ANY LIMITED REMEDY PROVIDED HEREIN.

- Should any provision of this Agreement be held by a court of competent jurisdiction to be illegal, invalid, or unenforceable, that provision shall be deemed amended to achieve as nearly as possible the same economic effect as the original provision, and the legality, validity and enforceability of the remaining provisions of this Agreement shall not be affected or impaired thereby.

- The failure of either party to enforce any term or condition of this Agreement shall not constitute a waiver of either party's right to enforce each and every term and condition of this Agreement. No breach under this agreement shall be deemed waived or excused by either party unless such waiver or consent is in writing signed by the party granting such waiver or consent. The waiver by or consent of a party to a breach of any provision of this Agreement shall not operate or be construed as a waiver of or consent to any other or subsequent breach by such other party.

- This Agreement may not be assigned (including by operation of law or otherwise) by you without WILEY's prior written consent.
- Any fee required for this permission shall be non-refundable after thirty (30) days from receipt by the CCC.
- These terms and conditions together with CCC's Billing and Payment terms and conditions (which are incorporated herein) form the entire agreement between you and WILEY concerning this licensing transaction and (in the absence of fraud) supersedes all prior agreements and representations of the parties, oral or written. This Agreement may not be amended except in writing signed by both parties. This Agreement shall be binding upon and inure to the benefit of the parties' successors, legal representatives, and authorized assigns.
- In the event of any conflict between your obligations established by these terms and conditions and those established by CCC's Billing and Payment terms and conditions, these terms and conditions shall prevail.
- WILEY expressly reserves all rights not specifically granted in the combination of (i) the license details provided by you and accepted in the course of this licensing transaction, (ii) these terms and conditions and (iii) CCC's Billing and Payment terms and conditions.
- This Agreement will be void if the Type of Use, Format, Circulation, or Requestor Type was misrepresented during the licensing process.
- This Agreement shall be governed by and construed in accordance with the laws of the State of New York, USA, without regards to such state's conflict of law rules. Any legal action, suit or proceeding arising out of or relating to these Terms and Conditions or the breach thereof shall be instituted in a court of competent jurisdiction in New York County in the State of New York in the United States of America and each party hereby consents and submits to the personal jurisdiction of such court, waives any objection to venue in such court and consents to service of process by registered or certified mail, return receipt requested, at the last known address of such party.

WILEY OPEN ACCESS TERMS AND CONDITIONS

Wiley Publishes Open Access Articles in fully Open Access Journals and in Subscription journals offering Online Open. Although most of the fully Open Access journals publish open access articles under the terms of the Creative Commons Attribution (CC BY) License only, the subscription journals and a few of the Open Access Journals offer a choice of Creative Commons Licenses. The license type is clearly identified on the article.

The Creative Commons Attribution License

The Creative Commons Attribution License (CC-BY) allows users to copy, distribute and transmit an article, adapt the article and make commercial use of the article. The CC-BY license permits commercial and non-

Creative Commons Attribution Non-Commercial License

The Creative Commons Attribution Non-Commercial (CC-BY-NC)License permits use, distribution and reproduction in any medium, provided the original work is properly cited and is not used for commercial purposes.(see below)